MASTER THESIS

THE EFFECTS OF IMPLANT ANGLES ON THE STABILITY OF SACROILIAC JOINT FUSION: A FINITE ELEMENT STUDY

RENSKE L.G.T. PIJNENBURG

SEPTEMBER 2024

Supervisor:	N.F.B. Kampkuiper MSc
Committee chair:	Prof.dr.ir. N.J.J. Verdonschot
External member:	Dr. ir. E.S. Perdahcioglu
Additional member:	Prof.dr.ir. G.J.M. Tuijthof
Additional member:	Dr. ir. T. Bitter
Additional member:	F. Janssen MSc

Faculty of Engineering Technology, Mechanical Enineering
Research Chair of Biomedical Device Design and Production
University of Twente

UNIVERSITY OF TWENTE.

ABSTRACT

This study investigates the impact of varying implant angles on the stability of the sacroiliac (SI) joint in lateral transiliac SI joint fusion using a Finite Element (FE) model of the pelvis. As a first step, FE simulations were executed that mimicked experimental SI-stability measurements under various conditions (i.e. varying implant configurations) as reported in literature. These analyses formed the basis to create a more anatomically realistic FE model of a patient. In this patient model, five clinically relevant implant configurations were selected with three implants: one parallel configuration, two in which only the middle implant is rotated and two in which all implants are rotated. Each configuration was arranged in a triangular pattern with consistent spacing between the implants at the SI joint gap. The configurations were chosen based on patient anatomy and surgical accessibility, and the motions at the SI joint were calculated under shear loading conditions. The results showed minimal differences in both displacement direction and magnitude across the different configurations. To gain a more comprehensive understanding, it is recommended to explore additional load cases and a broader range of implant angles.

TABLE OF CONTENTS

1. INTRODUCTION

This master thesis is part of a project by the Biomedical Device Design and Production (BDDP) chair at the university of Twente in collaboration with Medisch Spectrum Twente (MST). The research concerns the implant positioning for sacroiliac joint fusion. This chapter provides a brief introduction to the subject of sacroiliac joint fusion, states the goal of this research, and gives an overview of the content of this report.

Figure 1-1: Positioning of implants in the SI joint [1]

The sacroiliac (SI) joints are the joints between the sacrum and the ilium. These joints only have limited motion due to the strong ligaments connecting the sacrum and ilium. When patients experience pain originated from the SI joint, which may be caused by a high degree of movement or weakening of the pelvic ligaments, it is called sacroiliac joint dysfunction (SIJD). When non-invasive treatments are insufficient, the most common operative procedure is minimally invasive sacroiliac joint fusion (SIJF). Within this procedure, implants are used to fasten the sacrum and ilium with respect to each other and thereby reduce pain, see Figure 1-1. A complication after primary SIJF can be implant loosening, causing reoccurrence of the pain complaints. A possible cause for this implant loosening are relatively large micromovements between the implant and the bone during loading [2], caused by everyday activities. It is assumed that these micromovement will be minimal when there is less movement between the sacrum and ilium during loading. Therefore, it is needed to investigate the influence of different implant configurations on this relative movement. Several factors within an implant configuration may influence this. Examples of these factors are the number of implants [3] [4] [5] [6], implant spacing [3] [5] [6], implant depth [6], implant pattern (triangular or linear) [6] [5] [7], and implant angle [8] [5]. As there is lack of research about the influence of different implant angles [9] [10], this master thesis will focus on anatomically feasible implant angles. The research question of this study is therefore: 'To what extend do implant angles influence the stability* of the SI joint for lateral transiliac SI joint fusion while taking into account patient anatomy and operative accessibility?' Insight in mechanical behavior of a structure, in this case the influence on different implant configurations on the movements within the SI joint, can be obtained by experimentation or theoretical considerations. Although full-scale experiments are highly accurate, they are also very costly making modeling techniques often the preferred choice. The finite element method (FEM) is a widely used numerical method for analyzing structures and continua. The goal of this research is therefore: 'To develop, validate with literature, and use a Finite Element Model of the pelvis to determine the optimal configuration of the implants for SIJF, while taking into account patient anatomy and operative accessibility.'

This report begins with a medical background, covering the anatomy of the pelvis and the SI joints, followed by more information about SIJD and SIJF. Additionally, it provides a literature overview on the influence of different implants and implant configurations. The next chapter outlines the precise problem definition, goal, and research question that followed from the medical background. As the research question will be answered with the use of the finite element method, a mathematical background of this method is given in Chapter 4, which will later be used to explain different modelling

* 'Stability' in the context of 'implant stability' or 'implant configuration stability' is in this paper defined as the amount of motion between the sacrum and ilium because of the connection made by the implant. A good stability means little motion between the sacrum and ilium.

choises that were made. Furthermore, a small overview is given of what can be found in literature about FE modelling of the SI joint. To be able to work forward from a simple, validated model before diving into the complex geometry of the pelvis, it is decised to begin by modelling the experiments conducted on a physical foam block model found in literature. Further details on this model are provided in Chapter 5. In order to lean in what extend implant angles influence the movement within the SI joint in a simple geometry, it is decided to test the influence of the selected implant configurations on this foam block model. This is discribed in Chapter 6. In Chapter 7, the buildup of the more complex pelvis model is explained, and it is analysed how the implant configurations affect the stability in the SI joint. Lastly, an overall discussion and conclusion is given.

2. MEDICAL BACKGROUND

In this chapter, a medical background for this research project is provided. First, the anatomy of the pelvis and sacroiliac joint is explained after which the causes and symptoms of sacroiliac joint dysfunction are discussed. The different treatment methods are introduced and an elaboration is given on the minimally invasive treatment, together with what is already known in literature about different implant configurations.

2.1 ANATOMY OF THE PELVIS AND SACROILIAC JOINT

In colloquial usage, the pelvis is the complex structure that connects the spine and the legs. From anatomical perspectives, the pelvis is the part of the body surrounded by the pelvic girdle, where the pelvic girdle represents the appendicular skeleton on the lower limb [11]. The main function of the pelvic girdle is to support and balance the torso as well as containing and supporting the intestines, the urinary bladder and the internal sex organs. The pelvic girdle consists of three bones (two hip bones and the sacrum) and three joints (two sacroiliac joints and the pubic symphysis). The anatomy of the pelvic girdle is shown in Figure 2-1.

The pelvic girdle of males and females differs in several aspects, primarily due to the heavier build and larger muscles of most men and, as well as the adaptations in the female pelvis for childbearing [11]. The female sacrum is wider, less curved, more uneven, and tilted further backward than the male sacrum. Additionally, women tend to have greater pelvic mobility, experience more stresses, and have increased ligament strain in the sacroiliac joints compared to men [12].

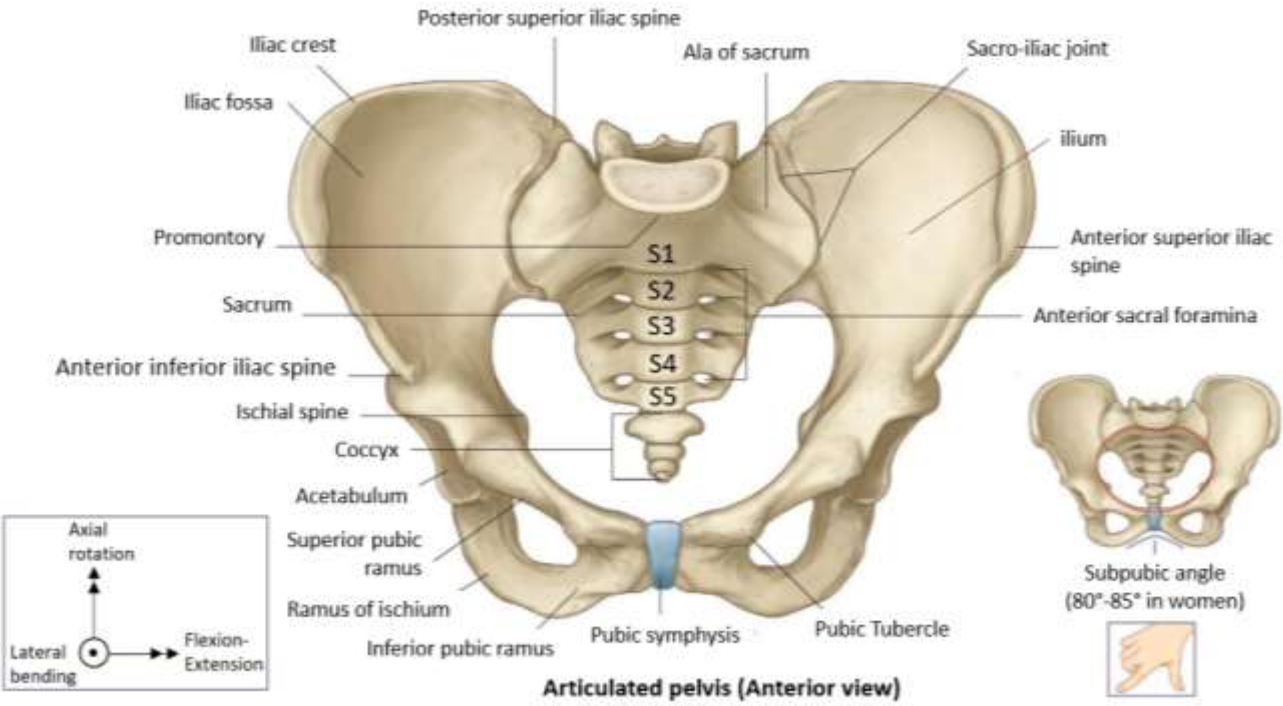

Figure 2-1: Anatomy of the pelvic girdle [13].

The sacroiliac (SI) joints are the joints between the sacrum and the ilium, and consist of synovial and fibrous joint parts. The synovial joint is the free-moving joint located between the ear-shaped articular surfaces of the sacrum and ilium, and is covered with cartilage. The fibrous joint, located between the tuberosities of these bones, includes the ligamentous structures between the sacrum and ilium and only has limited motion. See Figure 2-2. The articular surfaces of the synovial joint have irregular but congruent elevations and depressions that interlock. The movement at the SI joint is limited by interlocking of the articulating bones and the SI ligaments, resulting in relatively small gliding and rotary movements [11]. The SI joint range of motion in flexion-extension is about 3 degrees, in axial rotation about 1.5 degrees, and in lateral bending about 0.8 degrees [12]. The shape of the sacrum is extremely variable among patients [14] [15] [16].

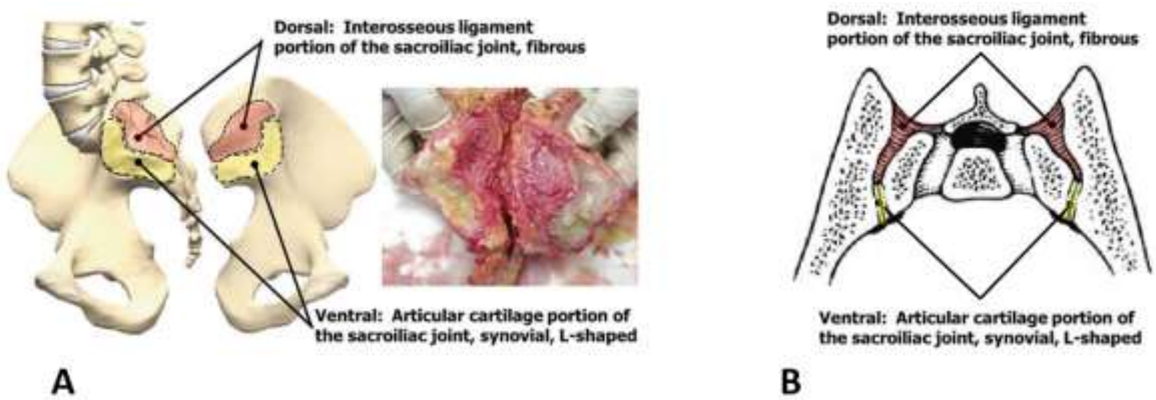

Figure 2-2: Lateral schematic visualization (A), real (A) and cut in transverse schematic visualization (B) of the synovial (yellow) and fibrous (red) joint parts of the SI joint [12].

2.2 SI JOINT DYSFUNCTION

When patients experience pain originated from the SI joint, which may be caused by a high degree of movement or weakening of the pelvic ligaments, it is called sacroiliac joint dysfunction (SIJD). SIJD is often experienced by women during or after delivery. The hormone "Relaxin" ensures that the ligaments of the pelvic joints become more flexible in preparation for childbirth. Relaxation of SI ligaments causes the interlocking mechanism of the SI joint to become less effective, permitting greater movement within the joint [11]. In some cases, the ligaments become too flexible, causing them to become overextended and sometimes damaged. This can result in chronic pain. SIJD can also occur in non-pregnant women and men. Pelvic complaints can for example develop because of hypermobility syndromes, after lumbar stabilization surgery, when the transverse and oblique abdominal muscles become weak, or can develop as a result of a sports injury or accident that has led to strained or torn pelvic ligaments. Pelvic asymmetry, misalignment of the pelvic joints or an unexpected, rapid change in normal movement can also cause SIJD. Pelvis instability can cause lower back pain, pain around the pelvis, hip and buttocks.

2.3 SACROILIAC JOINT FUSION

When non-invasive treatments prove insufficient, the most common operative procedure is minimally invasive sacroiliac joint fusion (SIJF). Open sacroiliac joint fusion has been performed in the past, but is no longer the preferred approach due to extensive healing processes and higher complication rates [17]. Both procedures result in a reduction in joint motion using implants/ bone grafts to fasten the ilium and sacrum with respect to each other, and thereby reduce pain. SIJF has minimal effect on either the spine or hip [18].

A typical minimally invasive SIJF procedure (called the Lateral Transiliac approach) is performed through a small incision of approximately 5cm in the buttock. A guide pin is inserted and the gluteal muscles are dissected to access the ilium. The positioning of the guide pin is visualized by fluoroscopic imaging and a safe trajectory needs to be confirmed in the inlet and outlet views during the procedure. See Figure 2-3 for the lateral, inlet and outlet views. The guide pin is hammered through the ilium, to provide passage for the implant to reach the sacrum, and inserted to an appropriate depth. Comparison of the fluoroscopic images during the surgery with predetermined landmarks on pre-surgical CT-scans, can be used to help the surgeon efficiently position the guide pins and later on the implants [19]. After the first guide pin is in position, spacers can be used to accurately position the second and third. Subsequently, a drill is used over the first guide pin to enlarge the cavity, and the triangular configuration is broached into it. The titanium implant is now inserted over the guide pin and hammered into the triangular cavity, after which the guide pin is removed. The last steps are repeated for the second and third implant. In most cased three implants are used, but depending on the configuration of the SI joint, the number may vary. The incision site is closed in layers using standard procedure. Most published series on fusion outcomes use this Lateral Transiliac Approach [20]. Also in Medisch Spectrum Twente (MST) this approach is used for SIJF surgery.

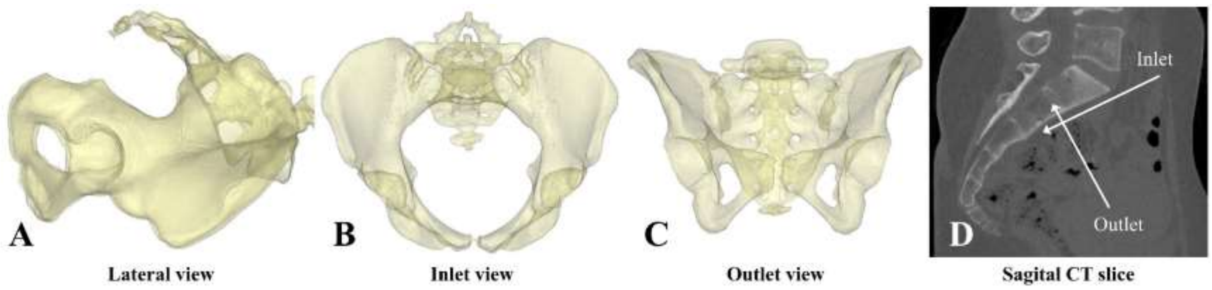

Figure 2-3: During the procedure, the patient is placed in a prone position, and fluoroscopy images are made in the lateral (A), inlet (B), and outlet (C) views. A central sagittal plane (D) is shown in which the directions of the inlet and outlet view are displayed. Figure taken from Kampkuiper et al. (2023) [19].

In literature, also other approaches are described. A variation on the Lateral Transiliac technique is the Posterolateral Transiliac procedure. The Posterolateral Transiliac approach has a more posterior starting point than the Lateral Transiliac approach and has its trajectory across the ligamentous part of the SI joint. The Posterolateral Transiliac technique was developed to lower the risk of injury or irritation of the S1 and S2 nerves within the foramina and to the branched of the superior gluteal artery [21]. Another procedure for SIJF is the Posterior Interpositional Approach (also called Dorsal Approach). It is performed through an incision along the dorsal midline, or a paramedian incision, allowing access to the ligamentary space between the sacrum and ilium. The soft tissue around the joint is cleared, after which the implants are placed without fixing the joint [20]. The implants are eighter structural bone allografts or metallic devices, and the procedure relies on ligamentotaxis for short-term SI joint stabilization and distraction arthrodesis for long-term SI joint fusion [21]. In Figure 2-4 an overview is given of the discussed different trajectories for minimally invasive SI joint fusion.

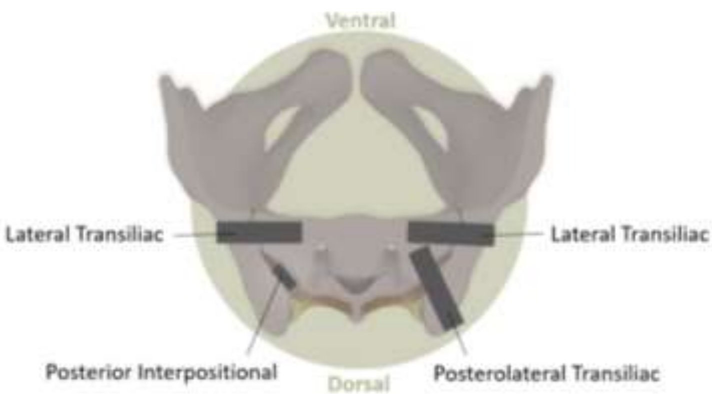

Figure 2-4: Overview of the trajectories for minimally invasive sacroiliac joint fusion. Figure adapted from Wang et al. [21]

Finally, there are some other, recently marketed devices that span or bridge the SI joint and engage in both the ilium and the sacrum. However, there is a lack of published clinical literature describing the safety and/or effectiveness of this type of device and this procedure. [21]

Whang et al. conclude in their literature review that studies reporting outcomes with the Lateral Transiliac procedure show larger improvements in pain and disability compared with those on Posterior Interpositional and Posterolateral Transiliac procedures [21]. Furthermore, a biomechanical study from Bruna-Rosso et al (see also Section 2.4) concluded that the trajectories preserving the interosseous ligament seemed to be beneficial to SIJ fixation. MST previously performed SIJF with only two implants. One implant in the ligamentous and one in the articular part of the joint. Since 2018, SIJF is performed with three implants, all located in the articular part of the joint. The latter is assumed to be more stable, with less chance of loosening (although this is not investigated). Therefore, the focus will lay on the lateral transiliac method in the rest of this literature study. The to-be-studied number of implants will be discussed in Section 2.4.

2.4 IMPLANTS AND CONFIGURATIONS

Several implants can be used in lateral transiliac SI Fusion. The iFuse implants [1] (SI-BONE, Santa Clara, CA, USA), see Figure 2-5, are by far the most commonly used in reportings [20] [21] [18], and are also used in MST. These are porous triangular titanium implants, of which the shape, coating, and interference fit should allow for initial stabilization and mechanical fixation. Biological fixation should lead to effective stabilization of the joint over time. Other implants that can be used in the Lateral Transiliac approach are screw types of implants. There are several manufacturers with screw type implant systems present [21].

Figure 2-5: Porous iFuse implant from SI-BONE. Image from [1].

Although a lot of data can be found on clinical outcomes of SIJF surgery, the data on the biomechanics of the SIJF is limited [18]. However, biomedical studies are of high importance as they complement clinical studies by providing fundamental insight into the mechanics of the SI joint, leading to more targeted and effective treatment approaches. In the existing biomedical literature, it can be found that several factors may influence the stability of SIJF. Examples of these factors are the number of implants, implant spacing, implant depth, implant pattern (triangular or linear) and implant angle. The following sections will review the existing literature on these factors.

2.4.1 Number of implants

Some studies could be found that access the influence of implant number on the stability of the SI joint. A Finite Element Model (FEM) study from Zhang et al. tested four different lateral transiliac configurations using eighter one or two threaded implants (see Figure 2-7) for two types of pelvic injuries. The study concluded that in both injury models, the placement of two implants provided a more stable connection between the ilium and sacrum than the placement of only one implant [3]. Inferior displacement, flexion and lateral bend (in bilateral stance) were recorded and analyzed in this study. Another Finite element study that compares the effect of one threaded implant in comparison to two threaded implants is the study from Bruna-Rosso et al. [8]. Six different posterolateral configurations were tested of which four configurations for one implant and two configurations for two implants, see Figure 2-8. In contradiction to the findings of Zhang et al., the addition of the second implant was not beneficial. However, this contradiction might be explained by the location of the second implant and the modification to the simulated ligament damage to enable implant insertion, considering the significant role of this ligament on the SIJ biomechanics [8]. Additionally, as only a single load case (compression) was tested, the results may present an incomplete picture. The model of Bruna-Rosso et al is also adapted by Dubé-Cyr et al. to determine the characteristics affecting SIJ fixation performance [22]. These models were instrumented with one to three threaded implants through a posterolateral trajectory (see Figure 2-9). They found that the addition of a second implant did increase the joint stability for both compression and flexion-extension loading, but the addition of a third did not. Cadaver experiments conducted by the same research group had similar outcome [23]. However, it is unsure whether the findings for lateral transiliac and posterolateral configurations can be compared properly. A cadaver study from Shih et al. also compared the effect of one or two threaded implants [4]. Four different lateral transiliac configurations were tested, of which two with one implant and two with two implants, see Figure 2-10. Again, the fixation using two implants provided better stability than the fixation that used only one implant for pure moment testing in flexion-extension, lateral bending, and axial rotation. Furthermore, a study from Freeman et al. using a synthetic model based on foam blocks, analyzed the difference of two in comparison to three triangular implants (see Figure 2-11) [5]. Here, shear and torsion were tested and it was concluded that the use of three implants provided the best stability. Lastly, Lindsey et al. did a Finite Element (FE) study on the influence of 1, 2 or 3 triangular implants [6]. Twenty-two lateral transiliac configurations were tested for flexion-extension, lateral bending (left and right), and axial rotation (left and right), see Figure 2-12. They also concluded that three implants gave the best stability. Conclusively, it is therefore assumed that the use of three implants is the most stable configuration.

2.4.2 Implant spacing

Besides the number of implants, Zhang et al. concludes with their FE model that, regarding the spacing of the implants, implants positioned closely to each other provide less stability than implants positioned further away from each other [3]. This is in line with the findings of the already mentioned synthetic model of Freeman et al. and the FE analysis from Lindsey et al. who also state that increasing the inter-implant distance increases stability [5] [6]. The results of Freeman et al even indicate that spacing between the implants is the most essential component for stability (in comparison to implant configuration and implant angle). Therefore, it is assumed that stability can be improved by increasing the implant spacing.

2.4.3 Implant depth

The effect of implant depth is only investigated by Lindsey et al., but only for the cranial implant [6]. They concluded that a longer cranial implant, and thus an increased cranial implant depth, resulted in more stability.

2.4.4 Implant pattern

For the positioning of three implants, two of the earlier mentioned studies also investigated whether a triangular implant pattern was better than a linear one (see Figure 2-6): Lindsey et al. concluded that a triangular configuration was more stable [6], but Freeman et al. could not find a significant difference between linear and triangular configuration (although they state that if implants must be placed closely, then nonlinear configurations may improve construct stability) [5]. A cadaver study from Soriano-Baron et al., also could not find a significant difference in linear or triangular implant

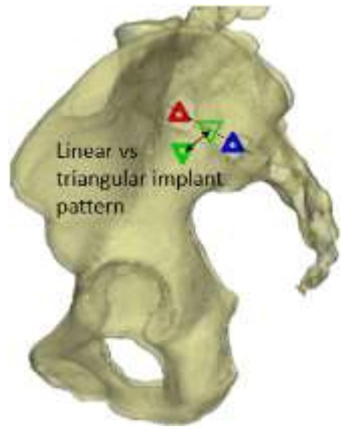

Figure 2-6: Linear versus triangular implant configuration.

configurations, although there was a trend towards triangular positioning [7]. They tested the effect of lateral transiliac implant positioning of three implants in a triangular (Trans-Articular) or linear (Posterior) position (see Figure 2-12) for flexion-extension, lateral bending, and axial rotation. The reason that their result was not significant may be due to the low amount of experiments. Conclusively, triangular configuration is expected to be superior to linear placement, but further investigation is needed. For this research, the assumption is made that triangular placement of the implants is indeed superior.

2.4.5 Implant angle

Finally, regarding angular positioning of the implants within surgical approaches, not a lot of research has been done. The research from Bruna-Rosso et al. concludes that the trajectory only had influence in two of the six cases. The only accessed load case was a compressive load, which induced rotation of the sacrum with respect to the ilium. They found that the more parallel the implant was with respect to the axis around which the relative displacement occurred within the SI joint, the better the fixation [8]. However, this model was not focused on the Lateral Transiliac approach. Freeman et al. also studied the influence of implant angle in their synthetic model and concluded that (for cyclic torsion testing) the configuration with linear-20mm-spaced-10°-angled-implants had significantly less ROM compared to the linear- and triangular-13mm-spaced-0°-angled configurations at both 0 and 10 000 cycles [5]. The configuration with linear-20mm-spaced-20°-angled-implant only experienced a significant reduction in ROM in comparison with the linear-13mm-spaced-0°-angled configuration at 10.000 cycles. Concluding from this, it is likely to believe that the implant angle has an influence on the implant stability. However, the ROM was also significantly lower for the linear- and triangular 22-mm-0°-angled configurations than both the linear- and triangular-13-mm-0°-angled configurations at 0 and 10 000 cycles. Therefore, the significant reduction in ROM for the angled implant configurations could also be because of the increased spacing. Furthermore, only two implant angles are tested, and both tested angles were in the same direction. Ideally, a range of angles and different directions should be tested. Furthermore, it is questionable to what extent the synthetic model is representative. Therefore, more research on this topic is needed.

Kampkuiper et al. suggested in a letter to Freeman et al. that, taking into account all findings on superior implant length, triangular configuration, spacing and angle, the combination of the triangular configuration with a converging orientation could be the most superior implant orientation [9]. This orientation would automatically create more spacing between the implants at the height of the SI joint gap. Furthermore, in this configuration a larger implant depth could be obtained without damaging the nerves in the foramina of the sacrum. (And although the implant may be inserted in an area with lower bone density in the sacrum which may has an adverse effect for a converging configuration, spacing between implants and implant depth may be a more important component for a stable SI arthrodesis.) Freeman et al. agreed with the thoughts from Kampkuiper et al. in their letter back [10], but this configuration is not yet tested.

Considering all the research on implants and implant configurations discussed in the paragraphs above, there appears to be a gap in the literature regarding the influence of anatomically feasible implant angles on SI joint stability.

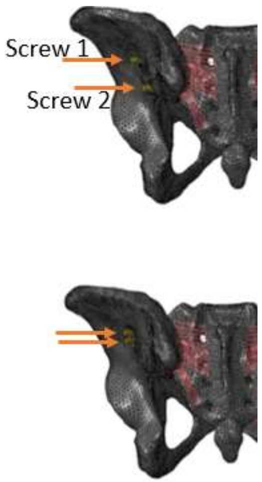

Figure 2-7: Two of the four Implant configurations tested by Zhang et al., for the other two configurations, screw 1 or screw 2 was removed from the top image. Image also adapted from Zhang et al. [3]

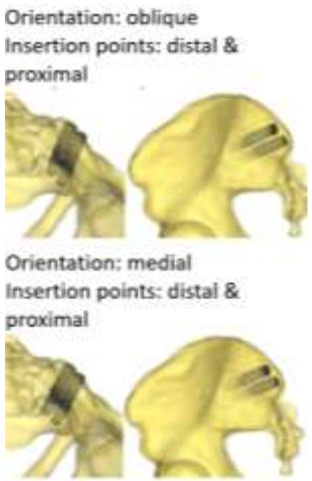

Figure 2-8: Two of the six Implant configurations tested by Bruna-Rosso et al., for the other four, one of the screws was removed from the top and bottom image. Image also adapted from Bruna-Rosso et al. [8]

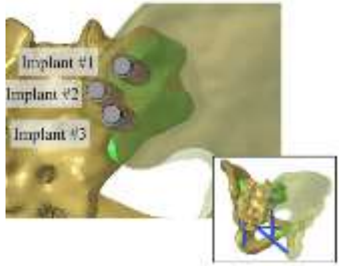

Figure 2-9: Positioning of the one to three implants through a posterolateral trajectory used in the Finite Element study and cadaver study of Dubé-Cyr et al. Image also adapted from Dubé-Cyr et al. [22] [23]

Figure 2-10: Two of the four implant configurations tested by Shih et al., for the other two configurations, screws 2 are pulled out from the top and bottom image. Image also adapted from Shih et al. [4]

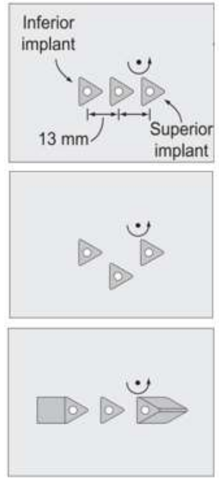

Figure 2-11: Three of the eight implant configurations tested by Freeman et al. (top view), two more were tested with more space in between the implants of the top and middle image, one more with a bigger angle for the third image. For the last two configurations, the 13- and 22-mm configurations were also testes using only two implants. Image also adapted from Freeman et al. [5]

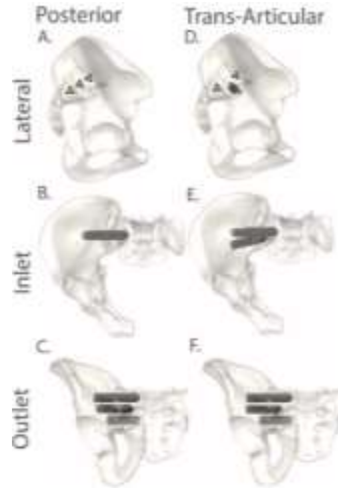

Figure 2-12: Implant configurations tested by Soriano-Baron et al. [7] These implant configurations are also tested by Lindsey et al [6]. (although it is unknown whether the middle implant was also angled from inlet point of view), with the addition of test with only one implant of each position, two implants of each position, and all mentioned configurations but with the superior implant ending mid sacrum, resulting in a total of twenty two implant configurations tested. Image also adapted from Soriano-Baron et al.

3. PROBLEM DEFINITION, GOAL AND RESEARCH QUESTION

Implant loosening is a possible complication after SIJF. An possible cause for this implant loosening are relatively large micromovements between the implant and the bone during loading [2], caused by everyday activities. It is assumed that these micromovements will be minimal when there is less movement between the sacrum and ilium during loading. Therefore, it is needed to investigate the influence of different implant configurations on this movement. As discussed in section 2.4, several factors may influence the stability of SIJF. Examples of these factors are the number of implants, implant spacing, implant depth, implant pattern (triangular or linear) and implant angle. As a diverging implant configuration is not anatomically feasible [9] and there is lack of research about the influence of other implant angles, this master thesis will focus on anatomically feasible implant angles. This way all separate components are investigated, before combining factors into more advanced configurations. The research question of this thesis is therefore:

To what extend do implant angles influence the stability of the SI joint for lateral transiliac SI joint fusion while taking into account patient anatomy and operative accessibility?

Insight into the mechanical behavior of a structure, in this case the influence of different implant configurations on the movements within the SI Joint, can be obtained by experimentation or theoretical considerations. Although full-scale experiments are highly accurate, they are also very costly making modeling techniques often the preferred choice. The finite element method (FEM) is a widely used numerical procedure for analyzing structures and continua [24]. The goal of this research is therefore:

To develop, validate with literature and use a Finite Element Model of the pelvis to determine the optimal configuration of the implants for SIJF, while taking into account patient anatomy and operative accessibility.

4. FINITE ELEMENT MODELLING OF PELVIS BACKGROUND

In this chapter, a detailed overview is given about three FE models that are used in studies concerning SIJF. The models are used as examples to learn from and therefore an overview is made to highlight their approaches. Since the FE modelling is fundamentally mathematical, this chapter starts with an explanation of the key underlying mathematical principles of the finite element method. This is needed to understand the influence of certain modelling decisions made in the FE models found in literature, and will later serve as a backbone for the decisions made in this research.

4.1 FINITE ELEMENT MODELLING IN GENERAL

Insight in mechanical behavior of a structure can be obtained by experimentation or theoretical considerations. Although full-scale experiments are highly accurate, they are also very costly making modeling techniques often the preferred choice. The finite element method (FEM) is a widely used numerical procedure for analyzing structures and continua [24].

Within this method, a structure is virtually broken into parts. Within each part simplifications are made, such that after combining all simplified parts together, a mathematical system is created which can approximate a structures behavior. The accuracy of this approximation largely depends on the simplifications made within each part [25]. For the last decades, the finite element method has become a highly flexible and powerful analysis tool, widely used in fields such mechanical, aerospace and civil engineering, but has also found its way to the medical world due to surpassing the limitations of for example cadaver studies by providing greater flexibility in simulating real-life conditions [26].

4.1.1 Mathematical principles of linear finite element method

The parts in which a structure is divided are called elements and the elements of the structure are connected at points called nodes. This arrangement of elements simulating a structure is called a mesh. Numerically, the mesh is represented by a system of algebraic equations to be solved for the unknowns at the nodes. In this section, the basics of these algebraic equations will be explained.

To understand the linear FE equations, the virtual work theorem is a good starting point. Although the derivation of these equations will be not discussed in detail, from $\delta w^{int} = \delta w^{ext}$ (the work done by the action of internal forces on a volume is equal to the work done by the action of external forces on this volume) it follows that the internal forces must be equal to the external forces.

$$F^{int} = F^{ext} \qquad \text{Equation 4-1}$$

In other words, when external forces act on a structure, internal forces must develop to achieve equilibrium: There must be a displacement field that generates strains, which in turn creates stresses, ultimately leading to internal forces. The goal of the finite element analysis is to determine the displacement field that will result in the correct internal force vector that is equal to the external forces. With (among others) this virtual work theorem, it can be derived that for small displacements the following holds:

$$F^{int} = \int_V B^T \sigma \, dV = \int_{V_0} B^T D B \, dV \; U = KU \qquad \text{Equation 4-2}$$

Therefore, the response of a structure to a load can thus be determined by solving the following system of equations:

$$[\mathrm{K}]\{\mathrm{U}\} = \{\mathrm{F}\} \qquad \text{Equation 4-3}$$

In which {U} is the response of the structure (for example displacement), [K] is the coefficient matrix relating loads and degrees of freedom (for example the stiffness matrix) and {F} is the external load vector (for example a force). The stiffness matrix for one element is now defined as:

$$[\mathrm{K_e}] = \int_{\mathrm{V_0}} [\mathrm{B}]^{\mathrm{T}}[\mathrm{D}][\mathrm{B}]\,\mathrm{dV} \qquad \text{with: } [\mathrm{B}] = \nabla[\mathrm{N}(\mathrm{x})] \qquad \text{Equation 4-4}$$

In which [D] is the elasticity matrix (containing o.a. the Young's modulus), [B] the strain displacement matrix (which relates the strain field in the body to the nodal displacements as can be seen in Equation 4-5) and [N(x)] are interpolation functions used to describe the displacement field within the elements. Furthermore, one should note that the stresses and strains are related to each other by the elasticity matrix [D] as also shown in Equation 4-5.

$$\{\varepsilon\} = \frac{\mathrm{du}}{\mathrm{dx}} = [\nabla\mathrm{N}]\{\mathrm{u}\} = [\mathrm{B}]\{\mathrm{U}\} \quad \text{and} \quad \{\sigma\} = [\mathrm{D}]\{\varepsilon\} \qquad \text{Equation 4-5}$$

The solution methods can be direct, based on inverting the [K] matrix such that {U}=$[\mathrm{k}]^{-1}${F}, or iterative.

Although these equations will not be discussed in detail, more information can be found in the reader 'An Introduction to the Finite Element Method' [25], the core principle is fairly straightforward and can be understood as the relation for a spring, involving a spring constant, force, and displacement (see equation Equation 4-3). Furthermore, material properties are incorporated into the elements via the [D] matrix, and the total displacements of the complex structure {U} are derived from the displacements within each small element using the [B] matrix. As stated above, the [B] matrix is composed with the use of interpolation functions, which describe the displacement field within the elements. Which interpolation functions are used is dependent on the element type chosen for a simulation.

Boundary conditions can be reinforced by assigning values for the displacements to specific nodes in the {U} matrix, loadings can be applied by assigning values for forces to specific nodes in the {F} matrix, and constraints can be implemented by adding extra equation rows representing these constraints to Equation 4-3. There are different options to choose in order to reinforce those constraints, all having their own tradeoff between computational time and accuracy.

The explanation above concerns the basic principles of FEM. One should note that those equations hold for static, linear FEM. For non-linear FEM, the same principle holds, but with other equations that are also valid for larger displacements. This will be discussed in the next paragraph. As dynamic FEM is not relevant to this research, dynamic aspects will not be discussed.

4.1.2 Mathematical principles of non-linear finite element method

In structural Mechanics, a problem is nonlinear if the stiffness matrix or the load vector is dependent upon displacement. In other words, for a static problem symbolized as Equation 4-3, both [K] and {F} are regarded independent of {U} in linear analysis, and regarded as functions of {U} in non-linear analysis. Within structures, non-linearity can for example be associated with changes in material properties (when Hooke's law does not cover the stress-strain relationship of the material anymore in Equation 4-5, due to for example large deformations or material yielding) or associated with changes in geometry (when there are large deformations or rigid rotation and the small strain tensor $\varepsilon_{\mathrm{ij}} =$

$\frac{1}{2}(u_{i,j} + u_{j,i})$ will lose its accuracy in Equation 4-5, or the initial volume of a structure is too different from the deformed volume in Equation 4-4). When structures interact with each other, also nonlinearity is expected at the contact interface: with deformation the contact area can change, which means that the contact forces are a function of the displacements [27]. There are more sources of nonlinearity, and for more information on these please read 'Concepts and Applications of Finite Element Analysis' [24]. Note that in fact all problems have a certain degree of non-linearity, but many problems are typically approximated by linear equations leading to sufficiently accurate results in less calculation time.

As well as for Linear FEM, the interest lies in finding the displacements that satisfy Equation 4-1. However, as we are not only interested in small deformations, the assumptions and therefore the derivation in Equation 4-2 described in the previous section cannot be used. Therefore, the internal force vector will alternatively be described by:

$$F^{int} = \int_{V_0} \hat{B}^T S \, dV \qquad \text{Equation 4-6}$$

In this equation, S (called the 2nd Piola-Kirchoff stress) is the stress as a function of the reference coordinates (instead of the current coordinates as is the case for the Cauchy stress σ from Equation 4-5). $\hat{B}$ is the new B-matrix, that relates the nodal displacements to the strains. As the strain tensor from Equation 4-5 is not suitable for large displacements, another strain tensor definition is needed. This new strain tensor E (called the Green-Lagrange strain tensor) is related to $\hat{B}$ and defined as follows:

$$E = \hat{B}U \quad \text{and} \quad E = \frac{1}{2}\left(F^T F - I\right) \qquad \text{Equation 4-7}$$

In this equation, F is a new introduced tensor (called the deformation gradient tensor) that relates the reference and current configuration. I is the identity matrix.

Note that solution methods cannot be direct, but an iterative solution method has to be used. An iterative solution method that can be used to solve systems of non-linear equations is the Newton Raphson method. This method works as follows. We want to obtain $F^{int} = F^{ext}$, and therefore the equation we want to solve is:

$$F^{int}(U^*) - F^{ext} = 0 \qquad \text{Equation 4-8}$$

Where U^* represents the solution. Note that at any point other than the solution, this equation is not equal to zero. The use of Taylor series expansion, gives the possibility to solve for the displacement ΔU, resulting in:

$$\Delta U = \left(\frac{\partial F^{int}}{\partial U}\right)^{-1} \left(F^{ext} - F^{int}(U)\right) \qquad \text{Equation 4-9}$$

Where $\frac{\partial F^{int}}{\partial U}$ is called the tangent stiffness matrix K^t, as it gives the relationship between the forces and displacements, but is dependent on U. As only the first Taylor series expansion is used, the solution will not be found in one step: several iterations are needed to go from an initial guess to better approximations. The current approximation is thus described by:

$$\Delta U_{j+1} = \left(K_j^t\right)^{-1}\left(F^{ext} - F_j^{int}(U)\right) \qquad \text{Equation 4-10}$$

This iterative process with continue until the difference between forces from Equation 4-8 are smaller than a certain pre-set tolerance. Note that several variations of the Newton-Raphson method can also be used to find a solution. Those deal with updating K^t differently.

The Newton Raphson method is used to solve for the displacements for a given load. In practice, this given load is split up in smaller load steps called increments, that are all solved for with the Newton-Raphson method. This approach ensured that the first guess in each increment is not too far off, increasing the likelihood of successful completion. Furthermore, this method allows for observation of not only the total deformation, but also the path of deformation.

As noted before, non-linearity is expected when contact happens between two structures. There are two problems associated with contact that need to be solved by the software. The first is to find out where contact will happen. During a simulation, this contact area can change and these changes need to be updated. The second is to solve for the contact forces. For this, constraint equations are used.

Note that above explanation only gives an overview of the non-linear finite element method. For more information, please read the lecture notes 'Nonlinear Finite Element Method' [27] and 'Geometrical nonlinearity and Contact' [28].

4.2 FINITE ELEMENT MODELS OF SIJ FOUND IN LITERATURE

Several studies can be found regarding FE-modelling of the pelvic bones. Since the focus of this report is to develop an FE model of the pelvis with an emphasis on implant configurations in the SIJ, this section will elaborate on three models that specifically investigate this aspect.

Ivanov et al. [29] developed in 2008 a FE-model of the Pelvis which was used in several follow-up studies: to investigate the effect of lumbar fusion on angular motion and stress across the SI joint in 2009 [30], the relationship between limb length discrepancy and load distribution across the SI joint in 2012 [31], the effect of SI joint fusion on adjacent lumbar segment motion in 2015 [32] and the stability of the SI joint of different implant configurations in 2018 [6]. In order to compare male and female pelvises (with and without SIJ fixation) also a FEM model of a female pelvis was made by the same research group in 2017 [33]. This female pelvis FEM model is also used to test the effects on hip stress following SIJF in 2019 [34] and is used for more detailed comparison of implant fixation in males and females in 2021 [35]. Another FE pelvic model developed to study implant configurations was created by Zhang et al. in 2014 [3]. This model was used to test four kinds of percutaneous screw fixation in two types of unilateral sacroiliac joint dislocations (see previous section). A third FE pelvic model is created by Bruna-Rosso et al. in 2016 [8]. The model of Bruna-Rosso tested different SI joint fixations under compression loads. This model is also adapted for further research to compare sacral and transarticular sacroiliac screw fixation in 2020 [36], and to determine the patient characteristics affecting SIJ fixation performance in 2021 [22].

The model of Ivanov et al. uses iFuse implants, the model of Zhang et al. uses screw implants and the model of Bruna-Rosso et al. uses RI-ALTO implants. In the rest of this section, the structure and model setup of the above-described FE-models will be elaborated on schematically. The models are used as examples to learn from, as assumptions must be made to simplify complex systems and only focus on the most significant aspects.

4.2.1 Model setup and simplifications

In APPENDIX A one can see an overview of the model setup with technical details for the three models described above. In all three studies the pelvic girdle is modeled with distinctions between cortical and trabecular bone, ligaments, the articular surfaces, and cartilage. All three models simulate the whole pelvis, in which only one SIJ is fixed with implants. The main difference in geometry among the three models is the inclusion of ligaments and other soft tissues, but as the incorporation of these components was beyond the scope of this study due to time constraints, further details on this aspect will not be addressed here.

An other difference in geometry is the thickness of the cortical 'shell', which varies across the different models: 1-8mm in the model of Ivanov et al., 0.45-1mm in the model of Zhang et al. and 0.05-5mm in the model of Bruna-rosso et al. Additionally, there are notable differences in element type and mesh size (note that the mesh of the ligaments will again not be discussed, but the details can be found in the appendix) across the three models. Ivanov et al. uses eight-node solid elements, while Bruna-Rosso et al. uses four node tetrahedral elements for the boney structure. Zhang et al do not specify the element type used in their model. The mesh size in Bruna-Rosso et al.'s model ranges from 0.4 to 2mm. Although the mesh size for the other two models is not explicitly stated, images included in the appendix suggest that a larger mesh size was likely used, except in areas around the implants in Lindsey et al.'s model. No mesh refinement study was reported in these three models.

4.2.2 Material properties

Table 4-1 presents the material properties utilized in the three models. It is notable that the Young's modulus for cortical bone is consistent between the models from Ivanov et al. and Zhang et al., while the Young's modulus in the model from Bruna-rosso et al. is more than 6 times lower. The Young's modulus for trabecular bone also varies across the three models, although the model of Bruna-Rosso et al. again utilizes the lowest value. Additionally, while the models from Zhang et al. and Bruna-Rosso et al. use homogeneous material properties for cancellous and trabecular bone, Ivanov et al.'s model incorporates non-homogeneous properties for sacral trabecular bone. The implants in all three models are characterized by a Young's modulus at least 6 times higher than of cortical bone, or are modelled as rigid. Furthermore, the Poison's ratios are modeled similarly across the three models.

In APPENDIX A.2 the material properties are stated for the ligaments, cartilage, and pubis in specific. Although the inclusion of ligaments and cartilage was beyond the scope of this study due to time constraints, an overview of their material properties used in the three models has been included to facilitate future research.

Table 4-1: Overview of the material properties used in the models from Ivanov et al. [22], Zhang et al. [10] and Bruna-Rosso et al. [11]. NS = not specified.
*Material properties of the sacral trabecular bone were assumed to be isotropic and varied in accordance to the apparent bone mineral density.
**Materials were considered homogenous and isotropic. A Johnson-Cook elastoplastic law was used for the bones allowing to represent their non-linear behavior and bone failure

	Cortical bone		**Trabecular bone**		**implant**	
	E [Mpa]	**v [-]**	**E [Mpa]**	**v [-]**	**E [Mpa]**	**v [-]**
Pelvis model of Ivanov et al. [29]	17000	0.3	70 varied with BMD*	0.2	115000	NS
Pelvis model of Zhang et al. [3]	17000	0.3	150	0.2	114000	0.3
Pelvis model of Bruna-Rosso et al. [8]	2625 Johnson-Cook elastoplastic law**	0.3	48.75 Johnson-Cook elastoplastic law**	0.25	Rigid body	Rigid body

4.2.3 Model validation and result validation

For the model of Ivanov et al. the validation study was based on simulation of different loadings and their directions from previous cadaveric studies which investigated the biomechanical behavior of the intact [37] [38] and injured sacroiliac joint [39], and stress distribution across cortical bone of the pelvis [40]. Numerical data was compared with the results that were reported in the previous literature. Within the follow-up study of Lindsey et al. about the effect of implant number, orientation, and superior implant length [6] the experimental results were compared to different studies per research element: for the experimental results regarding differences between triangular and linear configurations the results are compared to earlier studies about similar cadaver experiments done by their own research group [7]; the experimental results regarding the effect implant length are compared with research that made a statement about the pull out force of longer implants [41]; and for the experimental results regarding the effect of implant number is referred to three studies that state that two screws is better than one [42] [43] [44]. For the experimental result that far spaced implants are better than closely spaced implants, no reference for validation is stated.

The model of Zhang et al. was validated using in vitro data [45] and other simulation study results [46] [47]. For the validation, the model was adapted for proper comparison to the studies used for validation. Some of the experimental results were also compared to literature. The experimental results regarding overall displacement magnitudes where compared to a previous study that investigates the sacroiliac joint micromotion in pelvic disruption [48]. For the experimental results which imply that the type of fixation has minimal effect on lateral bending, is also referred to supporting literature which investigated the mechanical behavior under compressive loads [49].

The model of Bruna-Rosso et al. was calibrated using cadaver experiments conducted by themselves, after which the resulting Young's modulus for the ligaments was compared to a range of reported data in literature [50]. The experimental results were also validated, using cadaver experiments conducted by themselves. Furthermore, the experimental results regarding displacement pattern [51], the difference in displacement for one or two implants [52] [53], and the magnitude of intra-articular displacements [54] [55] are compared to literature.

4.2.4 Dependent variables/ loading and boundary conditions used

For the model of Ivanov et al., used in the research of Lindsey et al [6], the dependent variables were flexion-extension, lateral bending (left and right), and axial rotation (left and right). The percent change was calculated in comparison to the intact range of motion (ROM). Additionally, the median and range for the difference in ROM, and percent change were determined for each motion. How this range of motion was determined cannot be deducted from their paper. To measure these variables, a compressive follower load of 400N is applied at the superior surface of the L1 vertebra (for which the angle of the connector elements is defined such that the entire lumbo-pelvic segment did not go into any rotational motion following contraction of the connector elements). Depending on the measured variable, a 10Nm moment is applied at the superior surface of the L1 vertebra. Loading of the model was simulated using double-leg stance: To constrain the model, the caudal ends of the femur were fixed in all degrees of freedom and the femoral head was fixed to the acetabulum to prevent any rotation between the pelvis and the femur. See Figure 4-1. To model the implant-bone interaction, a mating part surrounding the implant was created with a longitudinal cut. The mating part's properties were that of the surrounding pelvis model and the press fit between the bone and implant was simulated by applying a closing force to the longitudinal cut [32].

In the study of Zhang et al., the dependent variables where the inferior translation (defined as displacement of the sacrum in the vertical direction), flexion (defined as forward rotation of the sacrum) and lateral bend (defined as lateral rotation of the sacrum). To measure these variables, a combination of an inferior translational force of 294N, a flexion moment of 42Nm and a lateral moment of 42Nm were applied at the S1 vertebra. See Figure 4-1. Boundary conditions were not stated. Furthermore, nothing is stated about the implant bone interface.

For the research of Bruna-Rosso et al., the dependent variables where the rotation (computed using the local axes of the ilium and the sacrum at the SIJ) and translation (computed as the average of the relative linear displacement between 14 pairs of facing points on each part of the articular surfaces) in the sagittal plane between the sacrum and the ilium at the SIJ. To measure these variables, 600, 800, and 1000 N were applied as ramped vertical loads on the center of the S1 endplate and maintained at a plateau for stabilization before releasing. The bottom part of the two iliac bones were fixed to represent the experimental conditions, as in the experiments the bottom of the iliac bones were casted in resin (in standing position with a neutral pelvic tilt, where the iliac crests and pubic symphysis were in the same vertical plane). See Figure 4-1. The implant bone interface was not modeled with a certain compression fit, but the sacrum and ilium geometries where modified by subtraction of the implant configuration. The interface between implant and bone was modeled as a contact interface with a point/surface penalty method with a Coulomb friction coefficient set to 0.2

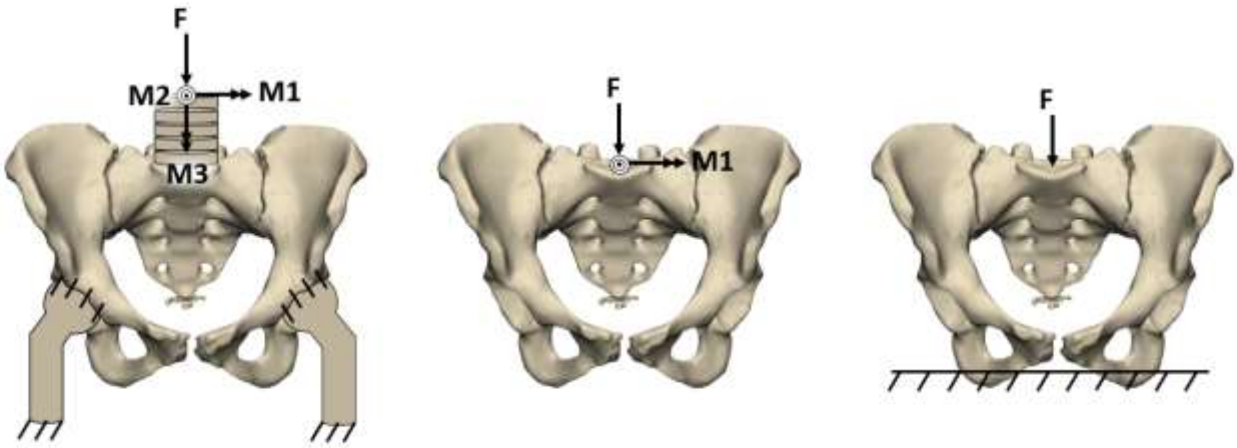

Figure 4-1: Loading and boundary conditions used in the Pelvis model of Ivanov et al. [29] in the study of Lindsey et al. [6] (left), Zhang et al. [3] (middle) and Bruna-Rosso et al. [8] (right).

4.2.5 Limitations

Ivanov et al state in their discussion that their model should be used for comparison instead of the prediction of exact values. In the follow-up study of Lindsey et al. [6] based on the model of Ivanov et al., also few limitations are stated in the discussion. They state that, as their model is based on a single patient in which no SI joint dysfunction is simulated, generalizing the results to the general patient population should be made with care. Additionally, they did not model all in vivo characteristics such as biological healing response after surgery, which thus could cause inaccuracies.

Zhang et al. stated that their limitations lie within the dependence on an anatomic reduction (this is a procedure to restore a fracture or dislocation to its normal position). Additionally, they state that the implementation in future research of making the material properties dependent on the bone mineral density could positively influence the results. Furthermore, they recommend to do further biomechanical research to validate their findings and explore the limitations noted.

Bruna-Rosso et al. primarily discuss limitations regarding the prediction of absolute values, since they used a cadaver study for the calibration and validation of the model. Therefore the small number of specimen, not representative age (the specimen where harvested from two females which were older than the for the population in which SI problems occur), and variability among the cadavers may make prediction of absolute values inaccurate. Other recommendations were made about the ligament modelling, but these will not be stated here as ligaments are outside the scope of this study. Furthermore, recommendations were made about the importance of further research in patient specific factors like bone quality, sacrum and ilia dimensions, and joint stiffness. They also advise to access the influence of bone damage at implant-bone interface. Finally, they state that different loading conditions should be tested and a larger variety of implant configurations.

The limitations of the three models, along with the similarities and differences in their assumptions, model construction, and experimental setup, as discussed in the previous paragraphs of this chapter, were used as insights for the design choices made in the remainder of this study.

5. RECREATING FOAM BLOCK MODEL OF FREEMAN ET AL.

To be able to work from a simple, validated model before diving into the complex geometry of the pelvis, an FE model was generated simulating experiments conducted on a relatively simple physical foam block model as published in literature [5]. The physical foam block model from Freeman et al. consisted of two blocks, representing the sacrum and ilium, that were connected by two or three implants. Cyclic torsion and shear tests were conducted with as objective to evaluate how different implant spacing, configuration and quantity effect the range of motion of the synthetic foam SIJ model. This chapter details the validation process of the FE foam block model, aiming to accurately replicate the first-cycle-experiments with 3 implants performed by Freeman et al. In the following chapter, the FE foamblock model will be addapted to examine the influence of different selected implant angles on the stability of the SI joint within a simple geometry.

5.1 METHOD

5.1.1 Model construction

Two blocks with dimensions 40x85.7x61.9 mm were made in Solidworks that represent the Ilium and Sacrum. The implant files from Kampkuiper et al.'s study were utilized and recreated in SolidWorks without the hole [19], see Figure 5-1: Implants from iFuse (images a and b, images adapted from and), implant configuration used by Kampkuiper et al. (image c) and implant configuration used in this research (image d).Figure 5-1.

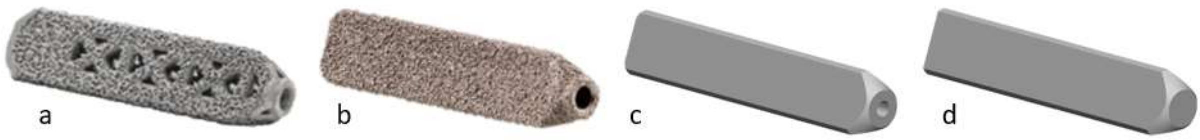

Figure 5-1: Implants from iFuse [56] (images a and b, images adapted from [57] and [58]), implant configuration used by Kampkuiper et al. [19] (image c) and implant configuration used in this research (image d).

The step files were imported in Abaqus, where the implants were subtracted from the ilium and sacrum blocks with a Boolean cut. All parts were meshed with quadratic tetrahedral elements, as these elements are suitable to mesh complex geometries, which is later needed to mesh the pelvis model, and have good performance for bending. An approximate global element size of 2.5mm, 4.3mm and 4.3mm is taken for the implants, sacrum block and ilium block. The mesh around the holes in the sacrum and ilium blocks was refined to an approximate global element size of 1.69mm. These mesh sizes were the automatically provided mesh sizes by Abaqus and remained unchanged as they are comparable to those used in some of the models found in literature that were analyzed in Section 4.2, while also limiting computational time. The total number of nodes was 199074 by average over all models (with a standard deviation of 18296) and the total number of elements was 136100 by average over all models (with a standard deviation of 13101). In Figure 5-2 one can see the meshed sacrum block, ilium block and implants for one of the tested implant configurations.

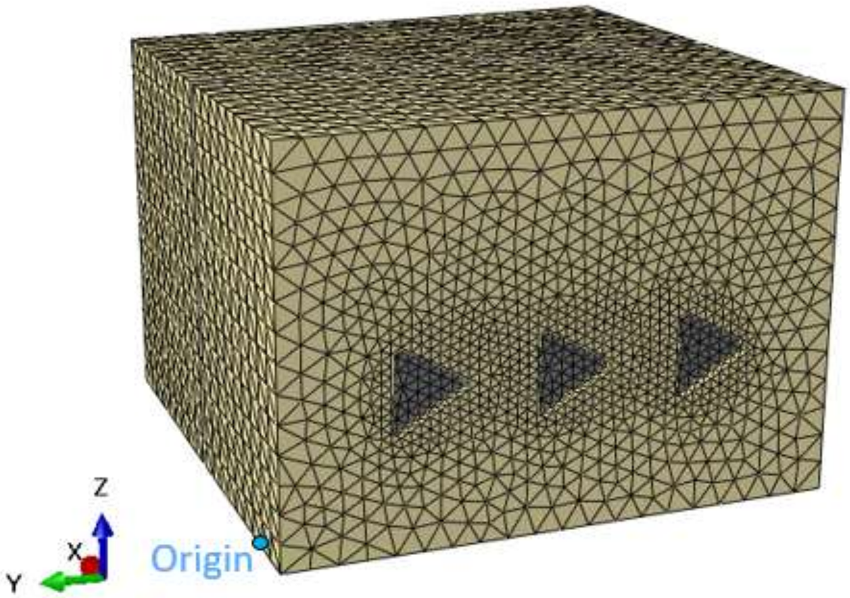

Figure 5-2: Mesh of the sacrum block, ilium bock and implants for the torsion test of implant configuration Linear 22.

Non-linear equations were used as contact is modeled and the resulting displacements are of importance. As noted in Section 4.1.2, there are two problems associated with contact that need to be solved by the software. The first is to find out where contact will happen. Furthermore, this contact area can change and these changes need to be updated. To do this, the standard interaction type 'General contact' is used, which automatically manages contact between all surfaces across the model. Although contact is primarily expected at the implant-bone interface, any other contact that occurs will also be automatically simulated this way. The second problem that is associated with contact, is to solve for the contact forces. To do this, for the General contact's normal behavior 'Hard Contact' is selected as pressure-overclosure and 'Augmented Lagrangian' as constraint enforcement method. The Augmented Lagrangian method introduces additional variables (called Lagrange multipliers) to enforce contact constrains relatively accurate, while adding a penalty factor for robustness. It employs an iterative correction scheme to refine the solution and ensure convergence. For the General contact's tangential behavior, a friction coefficient of 0.5 is used with 'Penalty' as friction formulation. Gao et al. stated in their literature review a found value of 0.45 as friction coefficient between human trabecular bone and plasma-sprayed titanium and 0.64 between human cortical bone and plasma-sprayed titanium [59]. Therefore, a friction coefficient of 0.5 should be representative as an overall friction coefficient. (Note that first the model was tried to run with friction coefficients of 0.1 and 0.3 as the friction coefficient was not known yet, but these models did not seem to converge to a solution after only part of the force was applied. No possible reason was found for this so the assumption was made that the implant began to slip at that point in contact, which was not the case with the higher friction coefficient. Furthermore, 'Penalty' as a friction formulation is chosen as this is computationally efficient, and tolerates some degree of constraint violation. (Note that, although the Lagrange friction formulation enforces the friction contains exactly, this formulation may have difficulties with convergence of the solution. Especially if many points are iterating between sticking and slipping conditions [60]. As the assumption was made that this might be a problem in the model, this method was not chosen.)

The element output is chosen to be analyzed at the integration points, as the primary interest lies in the displacements.

5.1.2 Material properties

The material properties used can be found in Table 5-1. It is assumed that the material behaves linear elastic as only small movements are expected.

Table 5-1: Material properties Foam block model [61] [62] [63].

	Young's modulus [MPa]	Poisson ratio [-]
Implants	113800	0.342
Ilium block	137	0.3
Sacrum block	23	0.3

5.1.3 Tested configurations

Both torsion and shear experiments have been conducted. In Figure 5-3 one can see the different implant configurations tested in the torsion experiments. All these configurations, except for the Angled 10 and Angled 20, are also tested for shear, although the shear constructs were angled 50° from horizontal (see Figure 5-4). In Figure 5-4 one can also see all used measurements. The measurements in red are those that were not stated in the publication by Freeman et al. and were thus estimated.

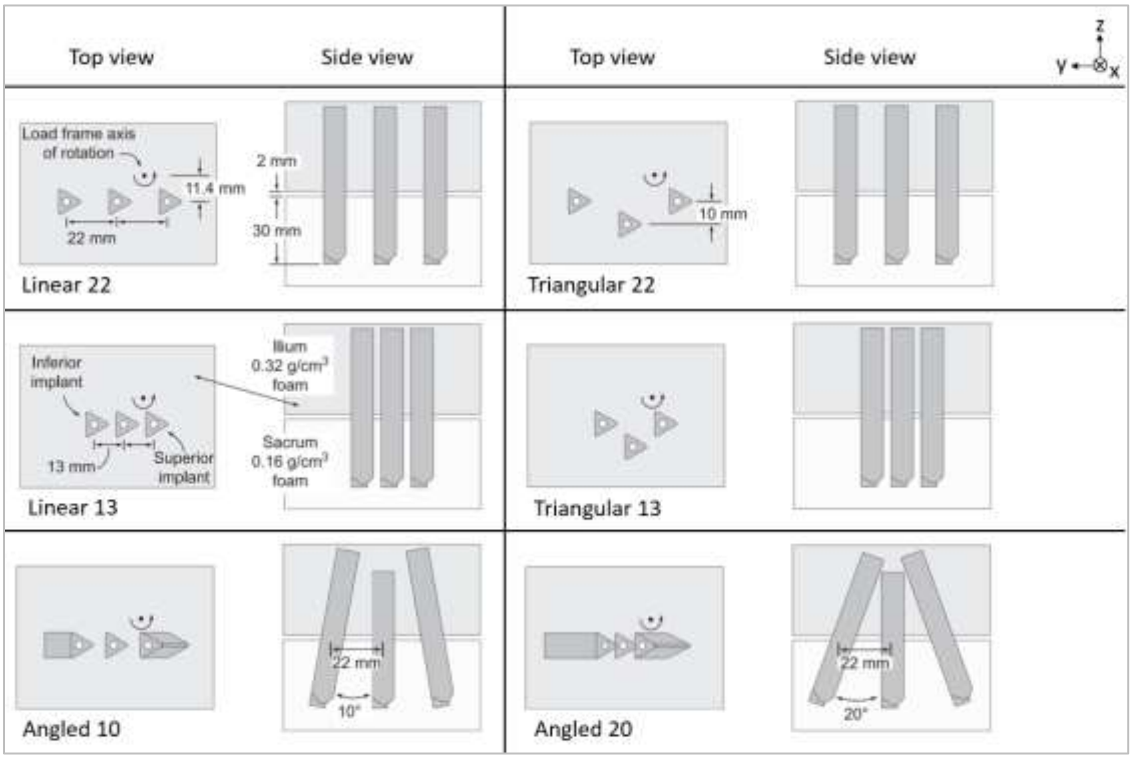

Figure 5-3: Configurations tested in the Foam block model.

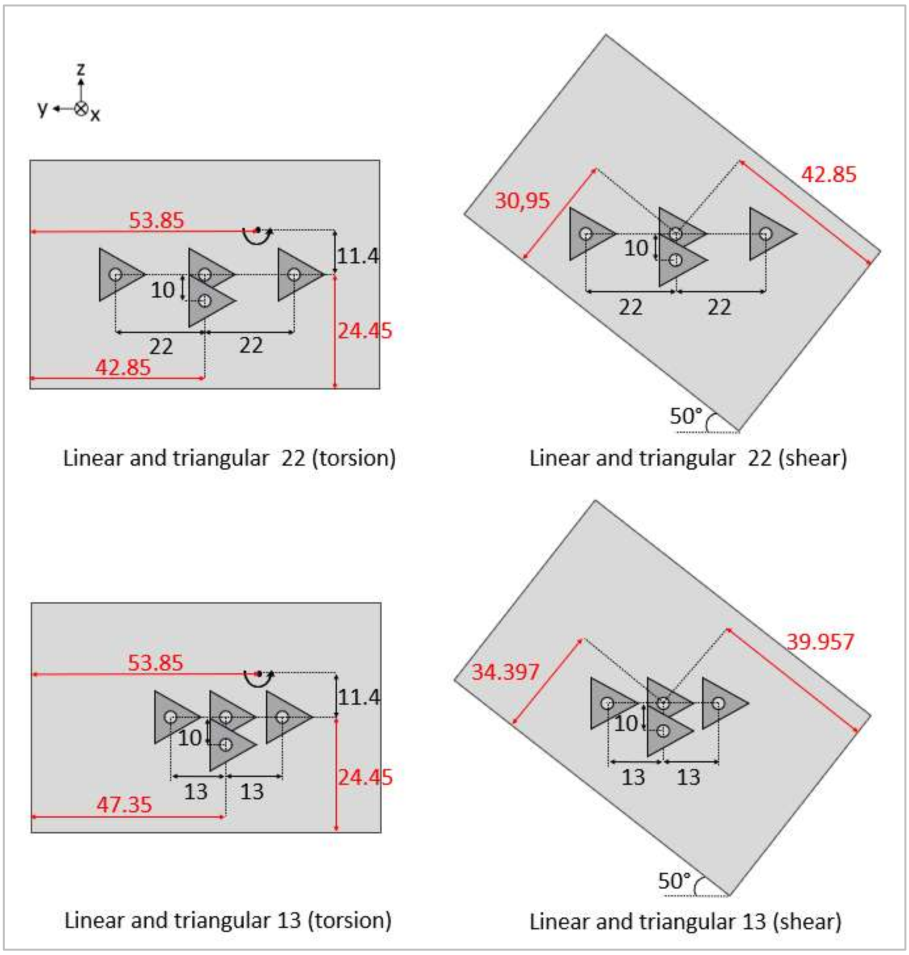

Figure 5-4: In red the measurements of the configurations of the foamblock models that were not stated in the reseach of Freeman et al. [5]

5.1.4 Loading and boundary conditions

Freeman et al. conducted cyclic testing with a sinusoidal waveform from 0 to ±7Nm for torsion and a sinusoidal waveform from -300N to -500N and -100N for shear. These loads where applied via a biaxial load frame with custom fixtures. The setups for both the torsion and shear experiments conducted by Freeman et al. are displayed in Figure 5-5 and Figure 5-6 respectively. In this research it was decided to not use this sinusoidal waveform, but do two separate simulations from zero to the extrema. For torsion this makes the convergence easier as otherwise the contact problem becomes more complex and thus the software struggles with convergence. At the direction change, the contact condition between the implant and foam block needs to be determined again. The software needs to calculate the contact forces and which nodes are in contact and which not. This process of determining the contact conditions can lead to instability and non-converging solutions as the software struggles to find a balance between the varying contact forces, varying nodes that are in contact and changing motions at an abrupt change. As the material is assumed to be linear elastic, splitting the load in two separate steps should have no influence on the combined range of motion.

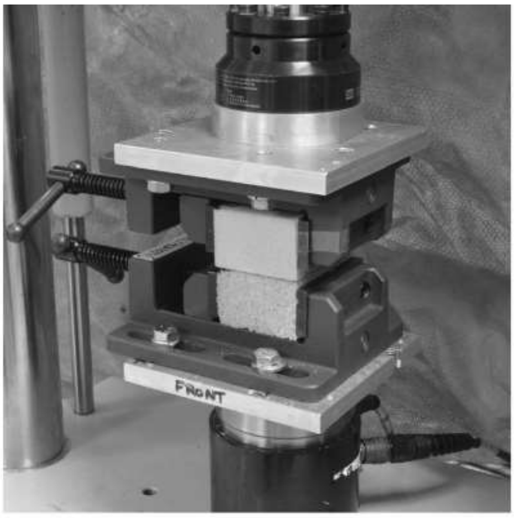

Figure 5-5: Test setup for cyclic torsion testing from Freeman et al. (Image also taken from Freeman et al.) [5]

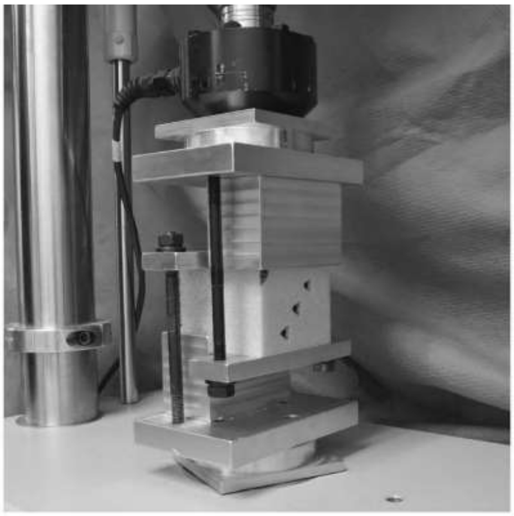

Figure 5-6: Test setup for cyclic shear testing from Freeman et al. (Image also taken from Freeman et al.) [5]

For the torsion tests, per implant configuration, one simulation is therefore done with a loading of M=7Nm applied on the center of rotation (see Figure 5-7), and one with a loading of M=-7Nm. Both are applied as a ramp. The top and bottom surfaces of the sacrum block are fixed and the node that is defined as the center of rotation is coupled to the top and bottom surfaces of the ilium block (see Figure 5-7). The range of motion is calculated as the difference between the minimum and maximum rotation of the point at which the load is applied.

For the shear tests, per implant configuration, one simulation is done with a loading of F=-100N applied on the top surface of the ilium block (see Figure 5-8), and one with a loading of F=-500N. Both are again applied as a ramp. The top and bottom surfaces of the sacrum block are again fixed. To make sure that the ilium can only move downwards, the top and bottom surfaces of the ilium are fixed in all degrees of freedom except for movement in z (see Figure 5-8). The range of motion is calculated as the difference between the minimum and maximum movement in z-direction from the ilium.

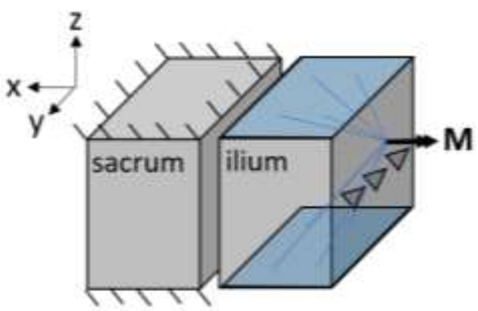

Figure 5-7: Boundary conditions for the torsion experiments.

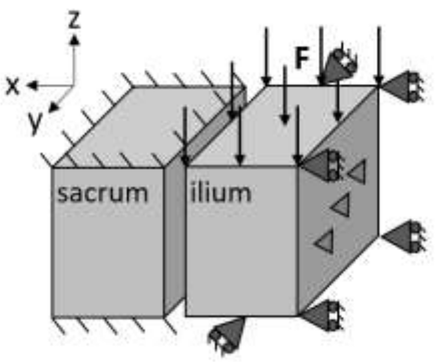

Figure 5-8: Boundary conditions for the shear experiments.

5.1.5 Validity analysis

The deformed mesh and the associated stress fields within the model are analyzed and assessed for validity using logical reasoning.

For all the simulations, the range of motion is determined and bar graphs are made to compare the results obtained by Freeman et al, and from the FE model. Note that not all precise values of the results of Freeman et al were stated in their paper and therefore they were read as precisely as possible from their bar graphs. As Freeman et al. conducted cyclic testing and this research did not, only the results from the first cycle from the experiments conducted by Freeman et al. are compared with the results in this study.

A scatterplot is created to visualize the relationship between the experiments from Freeman et al. and the results from the FE analysis. Furthermore, the Pearson correlation coefficient is calculated to quantify the strength and direction of the relationship between the two datasets, and the corresponding p-value is calculated to determine the statistical significance of the observed correlation. The p-value is calculated with a two-sided student's t-distribution, which accounts for the possibility of positive and negative correlations. This study assumes a linear relationship between the results from the FE model and the experiments from Freeman if the absolute correlation coefficient exceeds 0.8 with a probability of less than 0.05. Additionally, a line of best fit will be plotted for both the torsion and shear scatter plots.

An equivalence test is used to determine if the FEM model accurately predicts the experimental values from Freeman's study. This test assesses whether the mean differences between the FE model and the experimental results from Freeman et al. are within a pre-specified equivalence margin, indicating that the differences are insignificant. The null hypothesis states that there is a difference between the two groups (the groups are not equivalent) and the alternative hypothesis that there is no difference (the groups are equivalent). Note that an equivalence test is chosen specifically because it allows to test for equivalence rather than difference, which is uncommon in normal hypothesis testing. Again, a confidence interval of 0.95 is chosen for this analysis, using a two-sided student's t-distribution. The equivalence margins are set to the maximal standard deviation measured by Freeman et al. for the torsion and shear experiments respectively.

5.2 RESULTS

Figure 5-9 shows the deformed mesh of the model for the Linear 22 implant configuration during torsional loading. It can be seen that the ilium block rotates, and the sacrum block stays approximately stationary. Additionally, formed gaps can be observed between the blocks and the outer implants at several areas, marked by the arrows. In Figure 5-10 (top right image), one can see the rotating motion of the implants.

In Figure 5-10 illustrates the stress distribution within the implants for the Linear 22 implant configuration under torsional loading. The results indicate that the maximal stresses occur at the joint gap. For the left implant, compressive forces are located at the bottom and tensile forces at the top, indicating bending. Conversely, the right implant experiences tension at the bottom and compression at the top, indicating bending in opposite direction. Figure 5-11 displays the stresses within the sacrum block at the joint gap for the Linear 22 implant configuration under torsional loading. Mostly compression of the sacrum block is visible at the top of the left implant hole and at the bottom of the right implant hole.

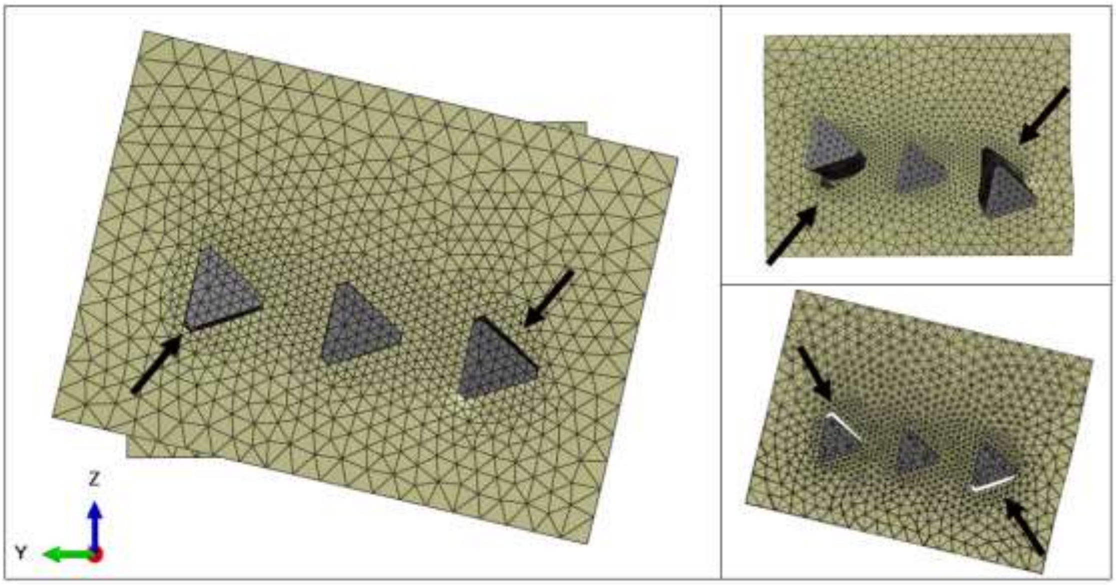

Figure 5-9: Deformed mesh of the whole model for the Linear 22 implant configuration during torsional loading (left image), the sacrum block at the SI joint gap (top right image) and a slice of the ilium block at the SI joint gap (bottom right image). Formed gaps between the blocks and the implants are marked by the arrows. (Deformation factor=20, all images are displayed within the same global coordinate orientation.)

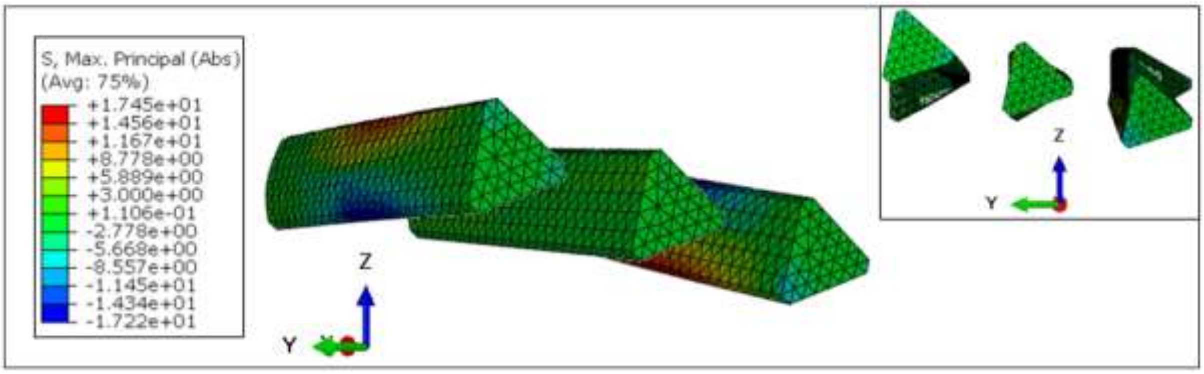

Figure 5-10: Stress distribution [MPa] within the implants for the Linear 22 implant configuration during torsional loading (center image), together with the deformed and non-deformed mesh of the implants (top right image, deformation factor=20).

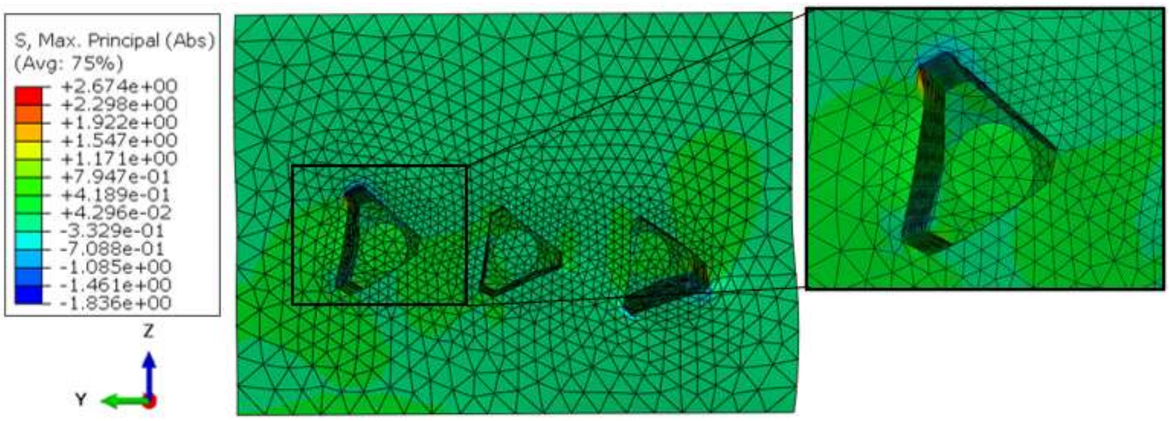

Figure 5-11: Stress distribution [MPa] within the sacrum block at the SI joint gap for the Linear 22 implant configuration during torsional loading

Figure 5-12 shows the deformed mesh of the model for the Linear 22 implant configuration during shear loading. It can be observed that the ilium block translates downward and deforms mostly at the sides and less at the center. Additionally, the ilium block translates a little to the left. The sacrum block stays at approximately the same position. Furthermore, formed gaps can be observed between the blocks and the implants at several areas, marked by the arrows.

In Figure 5-13 one can see the stresses within the implants for the Linear 22 implant configuration during shear loading. It is shown that the maximal stresses are located at the joint gap, with compression at the top of all implants and tension at the bottom, indicating bending. Figure 5-14 displays the stresses within the sacrum block at the joint gap of the neutral configuration during shear loading. Mostly compression is visible at the left/ bottom of each implant gap.

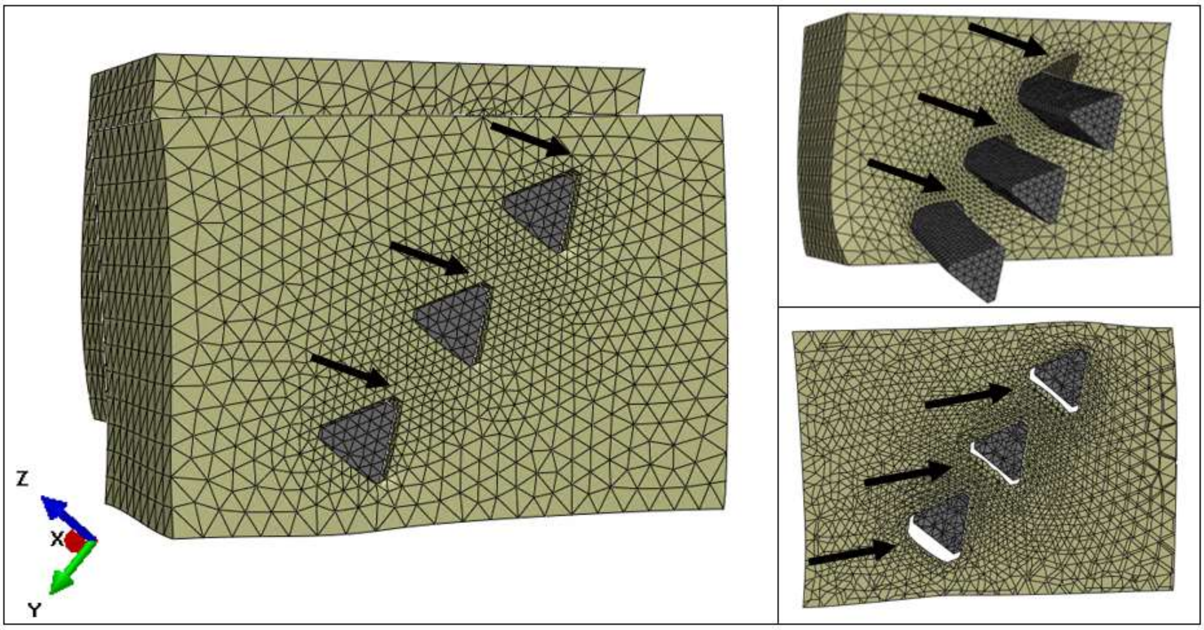

Figure 5-12: Deformed mesh of the whole model for the Linear 22 implant configuration during shear loading (left image), the sacrum block at the SI joint gap (top right image) and a slice of the ilium block at the SI joint gap (bottom right image). Formed gaps between the blocks and the implants are marked by the arrows. (Deformation factor=40, all images are displayed within the same global coordinate orientation.)

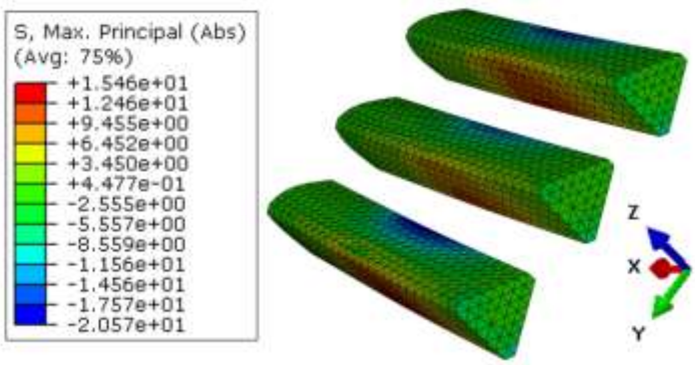

Figure 5-13: Stress distribution [MPa] within the implants for the Linear 22 implant configuration during shear loading.

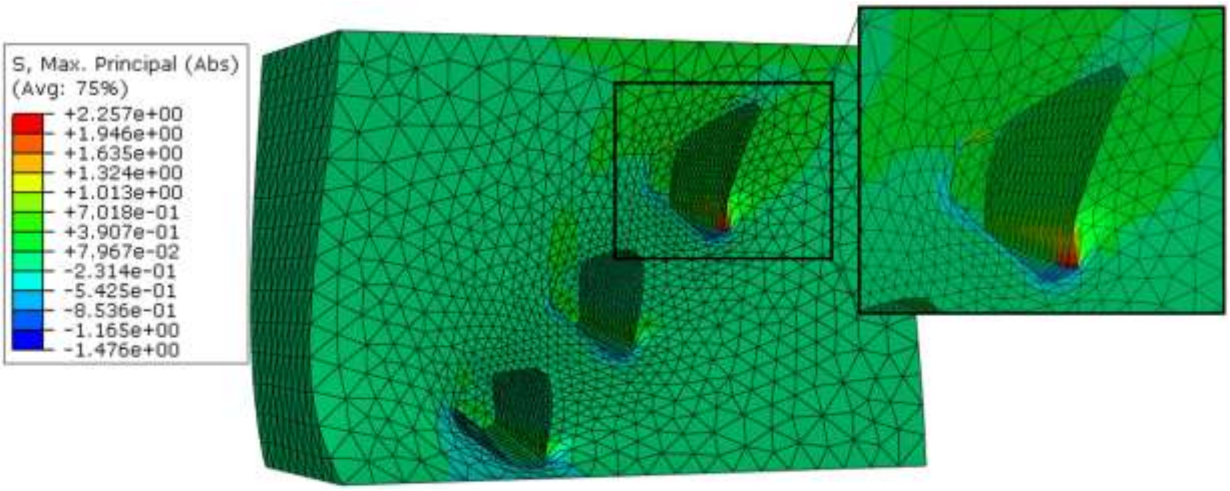

Figure 5-14: Stress distribution [MPa] within the sacrum block at the SI joint gap for the Linear 22 implant configuration during shear loading.

All other implant configurations show similar gapping and stress distributions.

In Figure 5-15 and Figure 5-16, the resulting ranges of motion per implant configuration are visualized for the experiments conducted by Freeman et al. and the results of the FE model. For the results from Freeman et al. also the standard deviations are displayed. Comparing the results for the torsion, it can be seen that the range of motion of all experiments of the FE model is consistently lower than the range of motion of the experiments from Freeman et al. For the shear experiments, the opposite is observed.

In Figure 5-17 and Figure 5-18, scatterplots are shown that plot the results of the experiments conducted by Freeman et al. against the results of the FE model. For the torsion experiments, a strong positive linear correlation is found (correlation coefficient=0.83, p-value=0.040<0.05), whereas for the shear experiments no significant correlation is found (correlation coefficient=0.86, p-value=0.14>0.05). The lines of best fit are described by $y = ax + b$ with $a = 0.82$ and $b = -0.57$ for the torsion results and $a = 1.37$ and $b = -0.06$ for the shear results.

The equivalence test gives an 95% confidence interval of [0.07;2.07] for torsion. Taking the maximal measured standard deviation, the equivalence interval is [-0.58; 0.58], which does not cover the 95% confidence interval. For the shear results the 95% confidence interval is [-0.14;0.01], while the equivalence interval is [-0.02;0.02]. Here also the equivalence interval does not cover the 95% confidence interval.

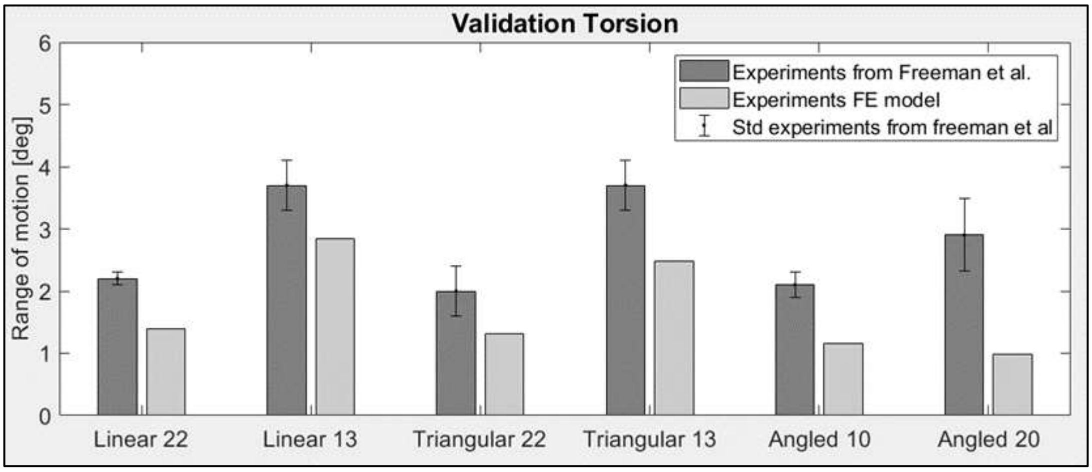

Figure 5-15: Comparison of the torsion experiments conducted by Freeman et al. and the results from the FE model. The values from Experiments of Freeman et al. are estimated from the Figures in the research of Freeman et al. [5]

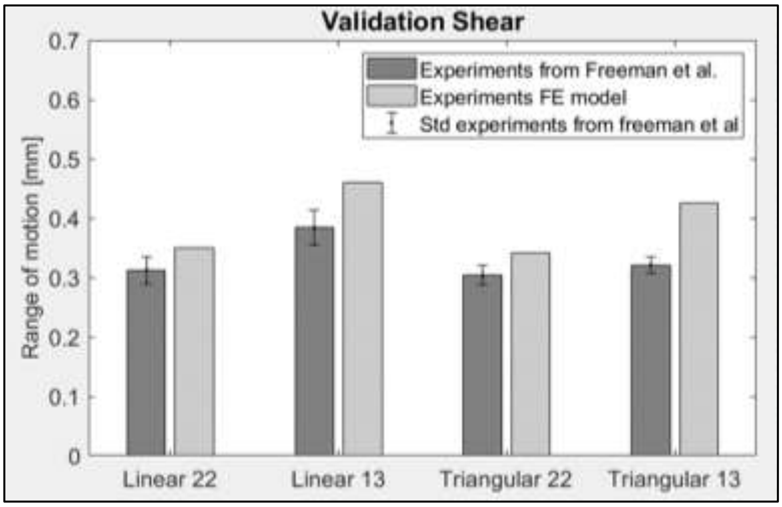

Figure 5-16: Comparison of the shear experiments conducted by Freeman et al. and the results from the FE model. The values from Experiments of Freeman et al. are estimated from the Figures in the research of Freeman et al. [5]

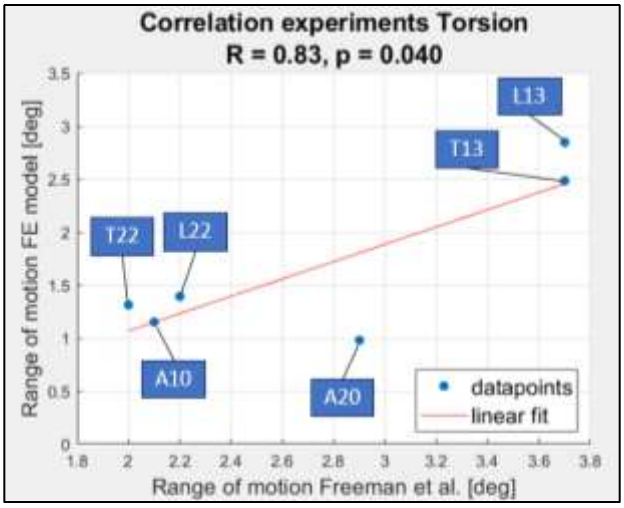

Figure 5-17: Scatter graph of results of the torsion experiments conducted by Freeman et al. plotted against the results of the torsion experiments from the FE model. (L22=Linear 22, L13=Linear 13, T22=Triangular 22, T13=Triangular 13, A10=Angled 10 and A20=Angled)

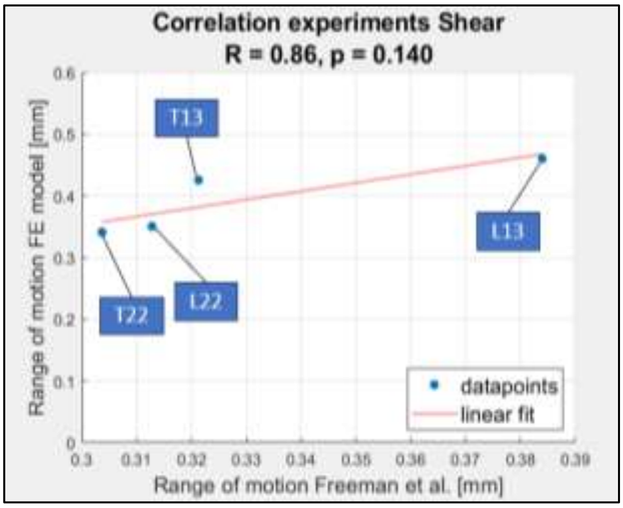

Figure 5-18: Scatter graph of results of the shear experiments conducted by Freeman et al. plotted against the results of the shear experiments from the FE model. (L22=Linear 22, L13=Linear 13, T22=Triangular 22 and T13=Triangular 13)

5.3 DISCUSSION AND RECOMMENDATIONS

A Finite Element model is created that resembles the physical model of Freeman et al. [5]. Both torsion and shear experiments are conducted for different implant configurations and compared to the results obtained by Freeman et al.

5.3.1 Interpretation of the results

The deformed meshes and stress distributions within the models were displayed and are for both torsion and shear as expected considered the applied loading. During torsional loading, the ilium block is rotated, exerting a downward force on the back of the right implant and an upward force at the back of the left implant, while the sacrum block is constrained and thus preventing these movements at the tip of the implants. This results in a tilting motion in counteracting directions for the left and right implants, causing gaps to form at the bottom of the left and the top of the right implant hole within the sacrum block at the joint gap (Figure 5-9 top right image), the other way around at the ilium block at the joint gap (Figure 5-9 bottom right image) and a similar pattern at the inlet of the implants again in the ilium block (Figure 5-9 center image). During shear loading, the ilium block is pushed downward, exerting a downward force on the back of the implants, while the sacrum block is constrained, preventing downward movement of the tip of the implants. This results in a tilting motion of the implants, causing gaps to form at the top of the sacrum block at the joint gap (see Figure 5-12, top right image), the bottom of the ilium block at the joint gap (see Figure 5-12, bottom right image) and the top of the ilium block at the inlet of the implants (Figure 5-12, center image). The stress distributions confirm this. Where the implants are considered to push into the blocks for example, compression within the blocks can be found.

From Figure 5-11 and Figure 5-14, it can be seen that the stresses within the sacrum (-1.836 to 2.674 MPa for torsion and -1.476 to 2.257 MPa for shear) are in the order of magnitude that was expected from the material data sheet [61]. This data sheet states a compression strength of 2.3 MPa for the sacrum block (and 5.4 Mpa for the ilium block). The maximal allowable tensile strength is not stated.

Comparing the results of the torsion experiments to the results obtained by Freeman et al., it could be seen that the range of motion of all experiments of the FE model is systematically lower than the range of motion of the experiments from Freeman et al. For the shear experiments, the opposite is observed. A possible explanation for this is the absence of preloading in the torsion experiments from Freeman et al. This absence of preloading can cause some play previous to loading, which is not present in the FE model (as a Boolean cut makes a perfect fit which is not possible in real life). The shear experiments are preloaded in the experiments from Freeman et al, causing less extra motion.

For the torsion experiments, the correlation coefficient between the results from Freeman et al. and the FE model is 0.83 (with p=0.040). Given that the absolute correlation coefficient exceeds 0.8 with a significance level below 0.05, a linear relationship between the FE model results and Freeman et al.'s experimental data is assumed, indicating that any observed errors are likely to be systematic. For the shear experiments the correlation coefficient is 0.86 (with p=0.14). Although the absolute correlation coefficient exceeds 0.8, the p-value is higher than 0.05, indicating that there is statistically not enough evidence to believe that there is a linear relationship between the results from the FE model and the experiments from Freeman. One should however notice that this high p-value is likely to be caused by the low number of samples, as the correlation coefficient is rather large. The p-value is influenced by both the sample size and the magnitude of the observed correlation coefficient, as can be seen in Equation 5-1 and Equation 5-2. If there is a small sample size, one should have a high correlation coefficient to maintain a low p-value. In this case, the correlation coefficient for the shear must be higher than 0.95 to obtain a p-value of less than 0.05. As Freeman conducted multiple physical experiments per implant configuration, resulting in inherent standard deviations, this is not a realistic value to strive for. Considering the small sample size paired with a relatively high correlation coefficient, it is likely that an addition of samples could strengthen the correlation coefficient, thereby lowering the p-value. Therefore, the models were assumed to have a positive linear relationship in the shear experiments due to the high correlation coefficient, despite the statistical test not definitively supporting this conclusion.

$$p = 2 \cdot (1 - \mathrm{tcdf}(|t|, n - 2))$$

Equation 5-1

$$t = \frac{r\sqrt{(n-2)}}{1 - r^2}$$

Equation 5-2

The lines of best fit for the scatterplots of the experiments conducted by Freeman et al. plotted against the results of the experiments from the FE model, are described by $y = ax + b$ with $a = 0.82$ and $b = -0.57$ for the torsion results and $a = 1.37$ and $b = -0.06$ for the shear results.

The negative b-values indicate that Freeman et al. observes greater movement in their models. A possible cause for the greater movement in the torsion models can be, as already has been discussed before, the absence of preloading and therefore the allowance for some initial play. As the shear experiments are preloaded, this initial play is expected to be less which can also be seen in the lower b-value for the shear experiments. As the experiments were only repeated 5 times (n=5), and a certain standard deviation is present, the resulting b-value for the shear experiments is likely to be caused by that. An additional possible cause for the b-value to be so much lower for torsion is because of the results for angled 20. For the torsion experiment, category Angled 20 is the only one that lays relatively far below the line of best fit. This could indicate a mistake in the FE model. However, one should also note that this category has the highest standard deviation, and Freeman only tested all configurations five times. Therefore it is assumable that the resulting mean value from Freeman is not reliable for this implant configuration.

For the torsion tests, the line of best fit has a slope of 0.82. This indicates that the range of motion observed by Freeman et al. increases more rapidly than that predicted by the FE model. In contrast, the shear experiments exhibit the opposite trend with a slope of 1.37. The a-value can be not equal to 1 for various reasons. For the torsion experiments, it is possible that the a-value is also lowered by the unexpected angled 20 result. Other possible causes for the a value not being equal to 1 are differences in contact properties between the simulations and the physical world (for example, a too low friction coefficient can underestimate the motion), differences in material properties (for example, a too high Young's modulus can underestimate the motion), the use of incorrect material models in the simulation (for example the assumption of linear elastic material behavior while also plastic deformation is present), the use of incorrect mesh size in the simulation (for example, a too big mesh can cause inaccuracy), etc. Note that, for most of the above mentioned possible causes for the differences between the models, it is contradictionary that for torsion the a-value is below 1 while for shear above. The difference can also be caused by limitations in the setup of Freeman et al. (for example friction within the setup) or other inaccuracies, that are also reflected in the high standard deviations.

Another possible reason for differences between the results of the torsion tests in specific, is a difference in boundary conditions. In the model of Freeman et al. the load is applied at the clamps, that make the ilium block rotate around the center of rotation. In the FE model, the load is applied at the coordinates that should be the center of rotation, which is constraint to the clamps, to replicate the loading of the physical model. However, the point to which the load is applied, was not constraint to only rotational movement in RX and therefore this point is not the center of rotation in the FE model.

Due to time constrains this effect is not further investigated, but it was observed that for implant configuration Linear 22, the point at which the load is applied has a displacement of 0.18 mm for an applied torsion of +7Nm. This indicates that the point at which the load is applied is not the center of rotation and therefore the boundary conditions of the model of Freeman et al. and the FE model are indeed different.

An equivalence test is used to determine if the FEM model accurately predicts the experimental values from Freeman's study. As for both the torsion and shear experiments the 95% confidence intervals are not covered by the equivalence intervals, it can be concluded that the FE model is not likely to predict the precise values of the experiments conducted by Freeman et al. This was to be expected as it could already be seen in Figure 5-15 and Figure 5-16 that the shear results of the FE model are higher and the torsion results of the FE model are lower than the results of Freeman et al.

5.3.2 Limitations of this research and recommendations for future research

Although the model is stated to be validated, some model assumptions introduce potential sources of inaccuracies. As explained in the Section 5.1.1, 'Penalty' as a friction formulation was chosen, although the Lagrange friction formulation enforces the friction constrains exactly. Additionally, it was assumed that splitting the load in two would have no influence on the combined range of motion as the material is assumed to be linear elastic. But even if the material behavior is linear, the whole model does not necessarily have to be. For example, the friction is likely to cause a certain degree of hysteresis, influencing the total range of motion.

Moreover, in the FE model it was assumed that all materials behave linear elastically. To verify this assumption, the stress plots from the experiments are evaluated. For some experiments, the maximal allowable compressive strength is exceeded [61], indicating failure of the material and thus an incorrect material assumption. Moreover, the maximal allowable tensile strength is not stated within the datasheet, but crushable foam structures usually experience a different response in compression than in tension. The Abaqus Documentation guide refers to Gibson et al. [64], Gibson and Ashby [65] and Maiti et al. [66], to state that in compression the ability of the material to deform volumetrically is enhanced by cell wall buckling processes, while in tension, on the other hand, cell walls break readily. As a result, the tensile load bearing capacity of crushable foams may be considerably smaller than its compressive load bearing capacity [67]. As the tensile load bearing capacity is probably smaller than the compressive strength, also failure due to tensile forces is expected. The occurrence of plastic deformation within the models is likely to be in line with the results from the physical experiments conducted by Freeman et al. as there is a difference between their 'zero cycle experiments' and the '10000 cycles experiments' [5]. The maximal Von Mises stresses within the implants were way below the yield strength, making the linear material assumption for the implants reliable.

Furthermore, the implant-bone interface is simulated without the addition of some type of clamping force. In the model of Freeman et al., the implants where broached into the bone (replicating SIJF surgery, as here the implants are also broached into the bone, see Section 2.3), resulting in a clamping force exerted by the foam blocks on the implants. The total stresses in the model will thus differ in reality. While this is not expected to affect the relative displacement differences between the implant configurations as long as the entire simulation remains within the elastic material region, variations may occur if plastic deformation is present.

Moreover, due to time limitations, no mesh refinement study is done. However, a mesh refinement study is a crucial step to ensure the accuracy and reliability of the simulation results. A too coarse mesh can result in inaccuracies as more interpolation is needed of the computed results, while the solution should converge to the true physical solution when the mesh is refined. Note that a too small mesh will result in a high computational time, and therefore a mesh study is also needed to help balancing accuracy and computational cost.

Furthermore, some warnings about negative eigenvalues were given for the matrix in the Angled experiments during the simulations for torsion. Additionally, verifying the mesh of all models, some element warnings could be found throughout the whole model. As quadratic elements are used, the element warnings are not expected to be a problem [68]. Furthermore, as no errors where present and the results are only analyzed globally instead of locally, both warning types were chosen to be ignored.

Lastly, it should be noted that the statistical models used for this analysis assume a normal distribution of the data. However, given the small sample size (only 4 configurations for shear and 6 for torsion), it is uncertain whether this data is indeed normally distributed. Due to this uncertainty, and the limited amount of data, one cannot draw proper statistical conclusions. Nevertheless, the high correlation coefficients suggest that the FE model captures the relationships between the displacements for different implant configurations. Since no additional configurations tested by Freeman, and due to time constraints it is not possible to do more physical experiments within this research, it is chosen to continue with these results.

5.3.3 Recommendations

Given these limitations, further research should focus on improving the accuracy of the FE model. First, the torsion experiments should be rerun with more precise boundary conditions, ensuring that the point of load application is constrained in translations. It is also recommended to test alternative friction formulations, such as the Lagrange formulation, to evaluate the impact on the results. Furthermore, it is advised to investigate the influence of non-linear effects like frictional hysteresis in physical experiments to see in what extent this would influence the deformations within the models. Moreover, future studies could explore more complex material models that account for plastic deformation, since the linear elastic model assumption is likely to be inaccurate. Additionally, a more detailed analysis on material failure should be conducted, as the evaluation of material failure is more complex than addressed in above discussion section. The failure criteria should be determined (for example the formation of cracks or yielding) and a failure theorem should be selected based on the stress components responsible for these failure mechanisms (for example von mises is a good stress theorem when looking at the yielding of materials, but maximal principal stresses when looking at the stress before breakage).

Furthermore, a mesh refinement study is recommended. As the interest of this study lies in the displacement of the ilium block, the mesh refinement study can be done by refining the mesh of the model with the least amount of elements (or for all models separately) gradually, until the displacement of the ilium block is within 5% of difference.

5.4 CONCLUSION

A Finite Element model is built to resemble the physical model of Freeman et al. [5] and both torsion and shear experiments are conducted to compare the resemblance of the results from the FE model to the experimental results from Freeman et al. From the equivalence test it was concluded that the FE model is not likely to predict the precise values of the experiments conducted by Freeman et al., but due to the high correlation coefficient that was found, it assumed that this error is likely to be systematic. Therefore, there is chosen to accept this model as validated, as the relative differences between the different experiments is of higher importance than the precise displacement values.

6. FOAM BLOCK MODEL FOR IMPLANT ANGLE MEASUREMENTS

A simplified version of the pelvis model is created within this chapter, building upon the validated foam block model from the previous chapter. This simplified model serves as a foundation before moving on to the more complex pelvis geometry and helps to determine the extent to which implant angles influence stability in a simple geometry. The model will again consist of two blocks that are connected by three implants. The model will be referred to as the Foam block model, as it is designed to resemble the physical foam blocks and set-up used in experiments from Freeman et al. [5] which were used for its validation (see Chapter 5). In the next chapter (Chapter 7), a pelvis model is build and the same experiments are conducted to see the influence of different implant angles on the SI joint stability.

6.1 METHOD

6.1.1 Model construction

The foam block model for implant angle measurements is constructed almost the same way as the validated FE foam block model replicating the foam block model of Freeman et al. [5] from the previous chapter (see Section 5.1.1 Model construction). However, the ilium block of the foam block model for implant angle measurements was adjusted to dimensions of 30x85.7x61.9 instead of 40x85.7x61.9 mm. This change allows the implants to protrude slightly in all tested implant configurations, making the setup more realistic. In SIJF procedures, implants are often placed positioned to protrude from the ilium, facilitating easier revisions if necessary. Again, although there are no element errors, warnings about a few elements per part were chosen to be ignored. The total number of nodes was 196154 by average over all models (with a standard deviation of 3451) and the total number of elements was 134460 by average over all models (with a standard deviation of 2470).

Furthermore, the model construction is automated using Python code to ensure that all models are built consistently, minimizing the risk of small errors that could introduce differences between the models. If an error occurs, it will occur in each model. In Figure 6-1 one can see a block diagram of the automated model construction.

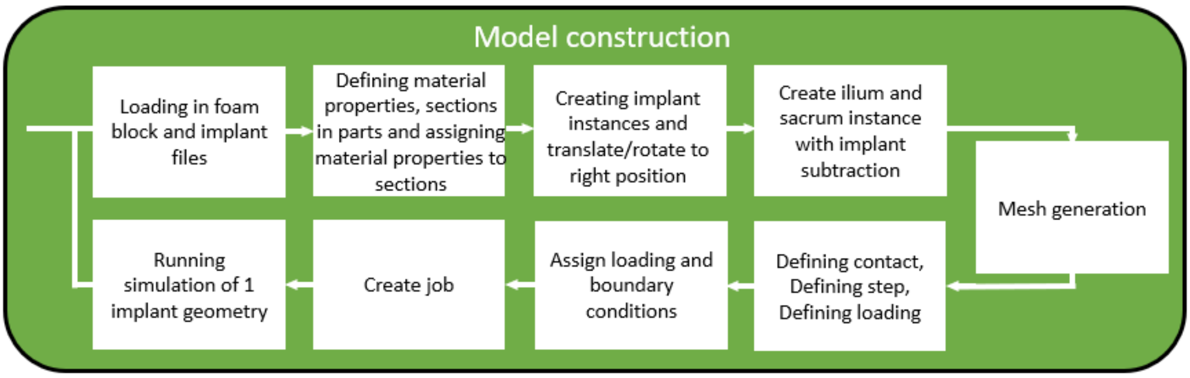

Figure 6-1: Schematic overview of the automation of the FE foam block model.

6.1.2 Material properties

The same material properties are used as for the validated FE foam block model replicating the foam block model of Freeman et al. [5] from the previous chapter (see Section 5.1.2). These properties are for clarity again stated in Table 6-1. Note that these properties are based on foam blocks that are often used for tests where bone properties are needed.

Table 6-1: Material properties foam block model [61] [62] [63].

	Young's modulus [MPa]	Poisson ratio [-]
Implants	113800	0.342
Ilium block	137	0.3
Sacrum block	23	0.3

6.1.3 Tested configurations

The stability of the implant connection will be tested for different implant angles. In Table 6-2 one can see the position in coordinates of every implant in 'neutral position' for the foam block experiments (experiment set 0, experiment 0 in Table 6-3). This neutral position together with the global coordinate system and the local implant coordinate system is visualized in Figure 6-2. In Table 6-3 all tested implant angles are stated. A visualization of the neutral position of the implants together with the maximum tested angle per implant can also be seen in Figure 6-2.

Note that the orientation of the global coordinate system is aligned with the coordinate system of the pelvis model from the next chapter, allowing the use of identical rotation angles in the experiments for effective comparison of the results. The configuration of the neutral position is adapted from the configuration used by Freeman et al. to a more anatomically feasible non patient specific configuration. The non patient specific implant configuration 'Triangular 22' of Freeman et al. is positioned in the foam block based on anatomical features such as the iliac cortical densities and the line from center implant 1 to center implant 3 that were obtained from the pelvis model in the next chapter. The angle of the iliac cortical densities is assumed to be similar among patients (see APPENDIX B), and although the line from center implant 1 to center implant 3 is for every patient different, this line will be taken as a basis to begin with.

The centre of rotation is chosen to be in the middle of the SI joint and thus in the middle of the spacing in between the ilium and sacrum blocks. This way, the spacing in between the implats remains consistant within the joint. This is important as the spacing has proven to influence the stability of the SI joint [3] [5] [6]. Furthermore, the contact surface of the implant with the ilium and sacrum blocks remains more consistent.

The axis of rotation used, is inspired from the literature study (see section 2.4). Kampkuiper et al. suggested in a letter to Freeman et al. that, taking into account all findings on superior implant length, triangular configuration, spacing and angle, the combination of the triangular pattern with a converging orientation could be the most superior implant orientation [9]. This orientation would automatically create more spacing between the implants at the height of the SI joint gap. Furthermore, in this configuration, a larger implant depth could be obtained without damaging the nerves in the foramina of the sacrum. Freeman et al. agreed with the thoughts from Kampkuiper et al. in their letter back [10], but this configuration is not yet tested in literature. Since the converging configuration proposed in Kampkuiper et al.'s letter is relatively patient specific, an alternative, less patient specific, variation was tested here. The axis of rotation have the direction of vector $\nu_\beta = [0, 0.9118, 0.4106]$, which is perpendicular to the iliac cortical densities (see Figure 6-2). This orientation of rotation axis still anatomically allows an increased implant spacing and depth in SIJF. rotation axis still gives the possibility to anatomically be able to obtain increased implant spacing and depth in SIJF. The range of tested implant angles is constraint to anatomically feasible angles within the pelvis model discussed in the next chapter.

Table 6-2: Coordinates of the implants in neutral position in the Foam block model. Rotations are in Euler angles with RzRyRx as order of rotation.

	X [m]	Y [m]	Z [m]	Rx [°]	Ry [°]	Rz [°]
Implant 1	0.027	-0.026	0.047	-24.252	0.000	0.000
Implant 2	0.027	-0.034	0.024	-35.746	0.000	0.000
Implant 3	0.027	-0.056	0.015	24.253	0.000	0.000

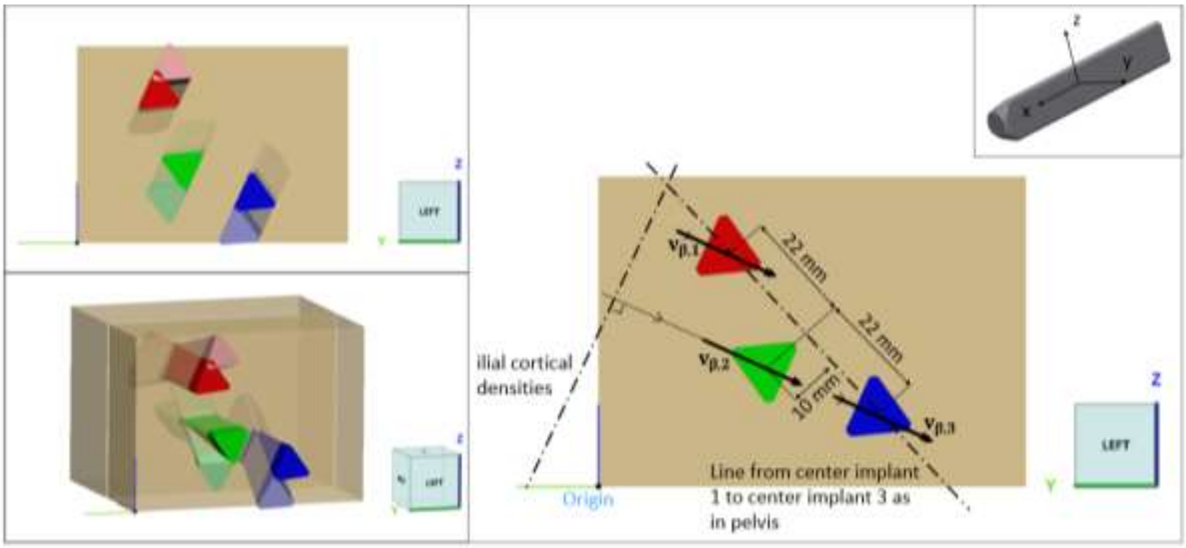

Figure 6-2: Neutral position of the implants in the foam blocks in global coordinate system (center image) with the local coordinate system for the implants (top right image) and the neutral position of the implants together with the maximum tested angle per implant (left images).

Table 6-3: Configurations tested.

		Implant 1	Implant 2	Implant 3
experiment set	**Experiment configuration**	**β,2 [°]**	**β,2 [°]**	**β,3 [°]**
1	1a	0	12	0
	1b	0	20	0
2	2a	-12	12	12
	2b	-16	20	20

6.1.4 Loading and boundary conditions

Similar loading conditions were selected as will be done for the pelvis model in the next chapter. A vertical loading of F=800N is applied at the top surface of the sacrum foam block, modeled as a pressure with total force equal to F. The bottom surface of the ilium block is fully constrained and the side surface of the sacrum is constrained in translation in x and rotation in y and z. See Figure 6-3.

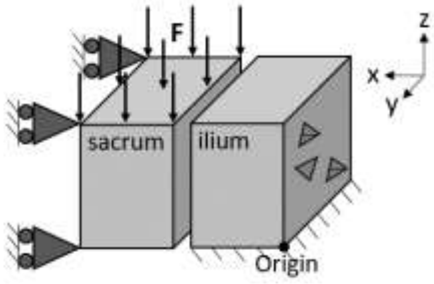

Figure 6-3: Loading and boundary conditions of the foam block model.

6.1.5 Result analysis

The deformed mesh and the associated stress field within the model are again analyzed and assessed for validity using logical reasoning.

To evaluate the impact of varying implant configurations on displacement, the difference in displacement between opposite nodes on the sacrum and ilium block at the SI joint was analyzed. Vector plots were generated for the nodal displacements in the YZ plane of the sacrum block minus the nodal displacements in the YZ plane of the ilium block for seven pairs of opposite nodes within the SI joint space. These nodes were selected to be closest to 7 sets of coordinates within the SI joint gap. The resulting vector plots, provided a comparative assessment of both the direction and magnitude of motion within the YZ plane.

Furthermore, bar graphs were created to display the minimum, median and maximal displacements for the analyzed nodes. This is done for the displacements in the YZ plane (corresponding to the vector plots) absolute X direction and for the total 3D displacements. The median displacement instead of the mean displacement is chosen as the mean is not a good estimate for the average displacement in the model, as the data is not normally distributed and therefore peeks within data have a lot of influence. The median should be a better indication.

The focus on the relative motion between opposite nodes within the SI joint is based on the assumption that minimizing the motion between sacrum and ilium during loading reduces micromovements, which are believed to causing implant loosening.

6.2 RESULTS

Figure 6-4 shows the deformed mesh of the model for the neutral implant configuration during shear loading. It can be seen that the sacrum translated downward and deforms the most at the sides and less at the center. The sacrum block stays at approximately the same position. Additionally, formed gaps can be observed between the blocks and the implants at several areas, marked by the arrows.

In Figure 6-5 one can see the stresses within the implants of the neutral configuration during shear loading. It is shown that the maximal stresses are located at the joint gap, with compression at the bottom of all implants and tension at the top, indicating bending. Figure 6-6 display the stresses within the sacrum block at the joint gap of the neutral configuration during shear loading. Mostly compression is visible at the right/ top of each implant gap.

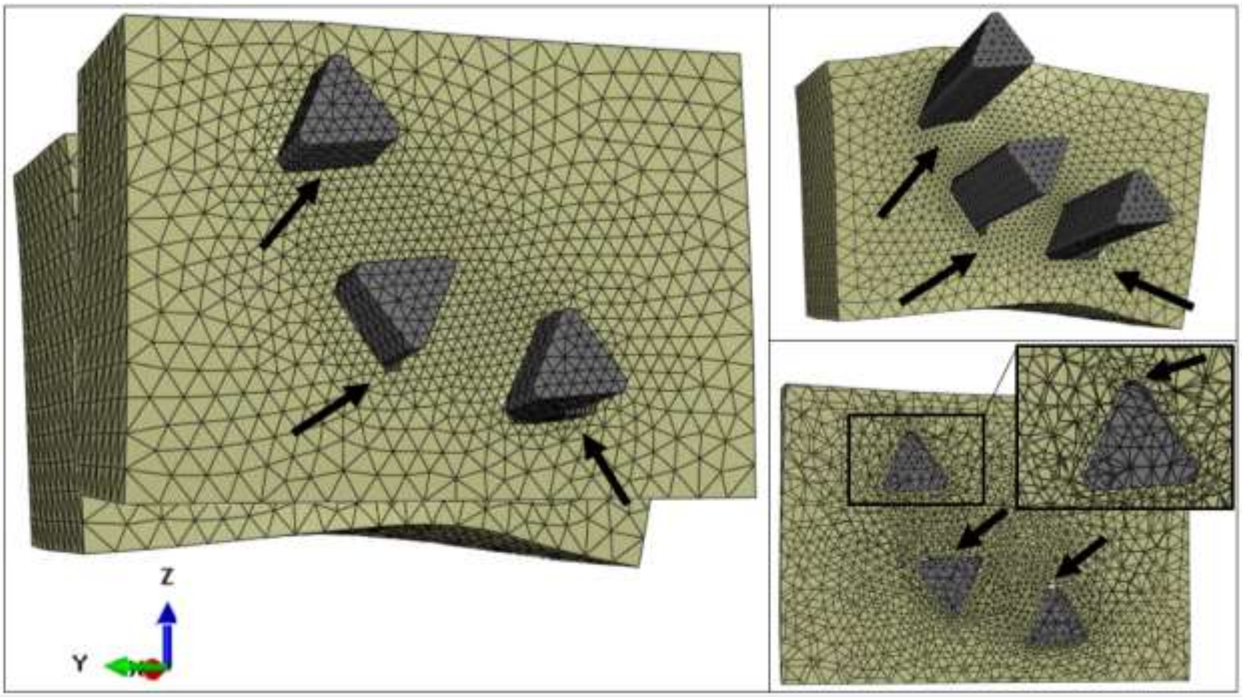

Figure 6-4: Deformed mesh of the whole model for the neutral implant configuration during shear loading (center image), the sacrum block with the implants (top right image) and a slice of the ilium block with the implants near the joint gap (bottom right image) for the neutral implant configuration, in which one can see the gaps forming in the foam blocks during shear loading. (Deformation scale factor = 10, all images are in the same coordinate configuration.)

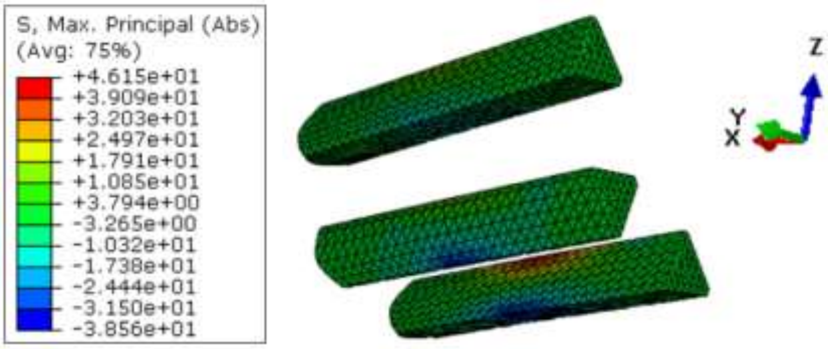

Figure 6-5: Stress distribution [MPa] within the implants for the neutral implant configuration during shear loading

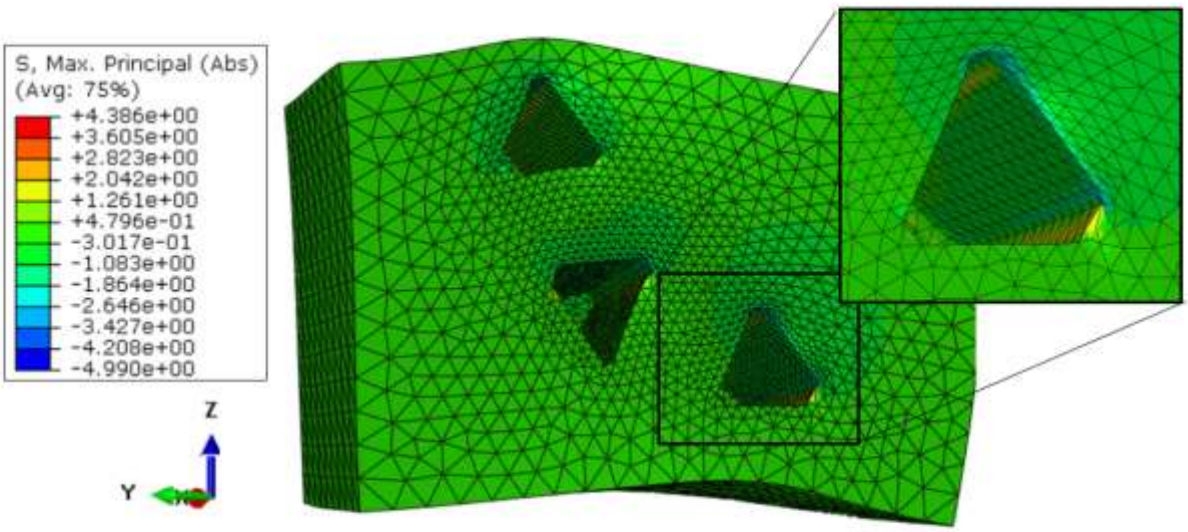

Figure 6-6: Stress distribution [MPa] within the sacrum block at the SI joint gap for the neutral implant configuration during shear loading.

All other implant configurations show similar gapping and stress distributions. Note that the results are comparable to the results from the shear experiments from the FE model replicating the models of Freeman et al in Section 5.2, taking the 'reversed' but similar loading and boundary conditions into account.

In Figure 6-7 one can see a vector plot of the nodal displacements in the YZ plane of the sacrum block minus the nodal displacements in the YZ plane of the ilium block for seven opposite nodes within the SI joint space. In this plot, the results for different implant configurations are visualized. In this figure, it can be seen that there is relatively small difference in displacement direction, as well as minimal difference in vector length. The minimal difference in vector length indicates that there is minimal difference in displacement magnitude.

In Figure 6-8 one can see the minimum, median and maximal displacement in the 3D direction of the 7 analyzed positions from Figure 6-7. The displacements are again defined as the nodal displacements of the sacrum minus the nodal displacements of the ilium for opposite nodes. From this figure no trend can be recognized: Between de a and b configurations for both experiments sets, the minimal displacements seem to decrease but the median and maximal displacements seem to increase. Furthermore, the neutral position (experiment 00) has the highest minimal displacements, but the lowest median and maximal displacements. Between experiment sets 1 and 2, not that much differences can be seen although experiment set 2 seems to have a higher median than experiment set 1.

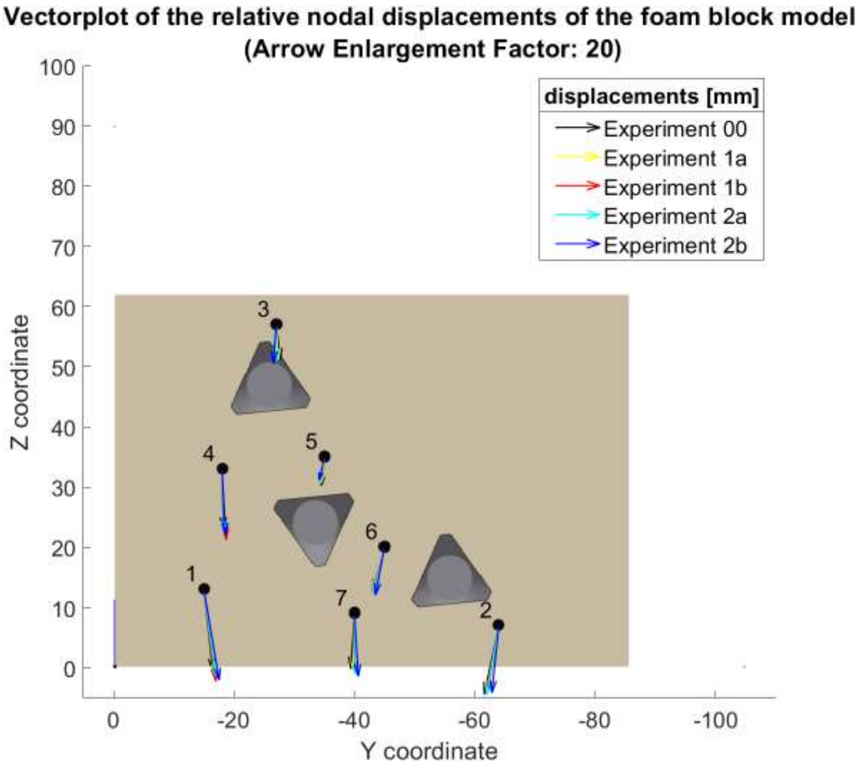

Figure 6-7: Vector plot of the relative nodal displacements of the sacrum block minus the nodal displacements of the ilium block for seven opposite nodes in the YZ plane of the foam block model.

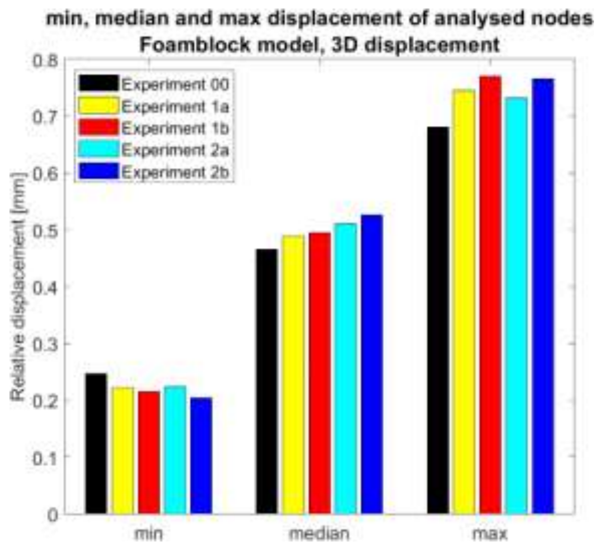

Figure 6-8: Minimum, median and maximal relative displacement in 3D of the analyzed nodes of the foamblock model. (The displacements are again defined as the nodal displacements of the sacrum minus the nodal displacements of the ilium for opposite nodes.)

6.3 DISCUSSION AND RECOMMENDATIONS

A simplistic version of the pelvis model is made, building upon the validated foam block model from the previous chapter. Shear experiments are conducted for different implant configurations and the range of motion within the joint space is compared.

6.3.1 Interpretation of the results

The deformed meshes and stress distributions within the models were displayed and as expected considering the applied loading. During shear loading, the sacrum block is pushed downward, exerting a downward force on the tip of the implant, while the ilium block is constrained, preventing downward movement of the back of the implant. This results in a tilting motion of the implants, causing gaps form at the bottom of the sacrum block at the joint gap (see Figure 6-4 top, right image), the top of the ilium block at the joint gap (see Figure 6-4, bottom right image) and the bottom of the ilium block at the inlet of the implants (see Figure 6-4, center image). The stress distributions confirm this. Where the implants are considered to push into the blocks for example, compression within the blocks can be found.

Furthermore, the range of motion is in the same order of magnitude as was the case for the shear experiments of Section 5 ‘Recreating foam block model of Freeman et al.’ This was expected as similar boundary conditions are applied and, although a higher shear force is applied, the relative displacements are analyzed instead of the total displacement wherefore less deformation within the blocks is taken into account.

Vector plots of the nodal displacements of the sacrum block minus the nodal displacements of the ilium block for seven opposite nodes within the SI joint space are made. From this plots it could be seen that there is minimal difference in displacement direction, as well as minimal difference in vector length, and thus displacement magnitude. Furthermore, bar graphs were made in which one could see the minimum, median and maximal displacement on the analyzed nodes. From these figures no logic trend could be seen. Therefore, it seems that the different implant configurations do not have a clear influence on the displacements within the SI joint for shear.

It is challenging to determine what outcome would be logically expected. Simplifying the model, while still representing it accurately using a Free Body Diagram (FBD) and equilibrium equations, is not feasible due to the complexity of the model and the numerous unknows involved. Predicting the force distribution within the foam block model is difficult, making comparisons between different models unreliable. Additionally, comparison with existing literature is not possible, as the influence of similarly angled implant configurations is not investigated in literature yet.

6.3.2 Limitations of this research

As this model is built upon the model validated with the results from Freeman et al from Section 5, unrealistic assumptions that have a large impact are not expected (although one must be cautious regarding the limitations discussed in Section 5.3.2, which will not be repeated here). Moreover, the automated construction of the model eliminates the potential for more errors that might arise from manual reconstruction of the models for different implant configurations: If an error occurs, it occurs in all models consistently. However, one mistake that is identified, is that the center of rotation of the implants, was not in the middle of the SI joint by a mistake made in the coding: it was positioned 4mm from the middle of the Si joint and thus 3mm within the ilium. This resulted in a less triangular implant configuration and reduced implant spacing as the implant angle increased. Since both reduced implant spacing and a more linear implant configuration are both known to negatively influence implant stability (see Section 2.4), this error might have a noticeable influence on the results. Additionally, as the implant angle increases, the implant-sacrum contact surface reduces in comparison to the implant-ilium contact surface, which is also expected to reduce the SI joint stability due to higher forces per unit area at the sacrum resulting in more deformation per unit area. Although the shift in the center of rotation is relatively small, the already minor differences between implant configurations and the cumulative negative effects suggest this could still influence the results.

6.3.3 Recommendations

Besides the recommendations that were already discussed in Section 5.3.3, that might have an influence on this section as well, it is advised to rerun the analysis with the correct center of rotation.

Furthermore, since the interest of this study lies in the relative displacements within the SI joint, the mesh refinement study that was recommended in Section 5.3.3 can be done by refining the mesh of the model with the least amount of elements (or for all models separately) gradually, until the displacements at the 7 analyzed nodes is within 5% of difference, instead of the overall displacement.

Although the different implant configurations do not have a clear influence on the displacements within the SI joint for shear, it was still recommended to proceed with the pelvis model due to time constrains, as the primary objective of this research is to investigate the influence of implant angle on displacements within the SI joint of the pelvis. While the foam block model discussed in this chapter shares fundamental similarities with the pelvis model, such as the two-part structure connected by three implants, comparable boundary conditions and similar loading scenarios, the foam block model remains a highly simplified version. The difference in geometry is expected to result in greater torsion of sacrum in the pelvis model, given that the force is applied anterior to the implant configuration. Moreover, the pelvis model is fixed at the acetabulum, introducing additional momentum. See Figure 6-9. This additional moment was not present in the foam block model, where fixation occurs directly beneath the implants. Furthermore, the difference in material properties (homogeneous in the foam block model versus non homogeneous in the pelvis model) could lead the different implants to have other contributions to the stability of the SI joint. All these variations make the model thus more complex, which may influence the results. To draw more reliable conclusions about the influence of implant angle on the SI joint stability, the study will proceed with the pelvis model.

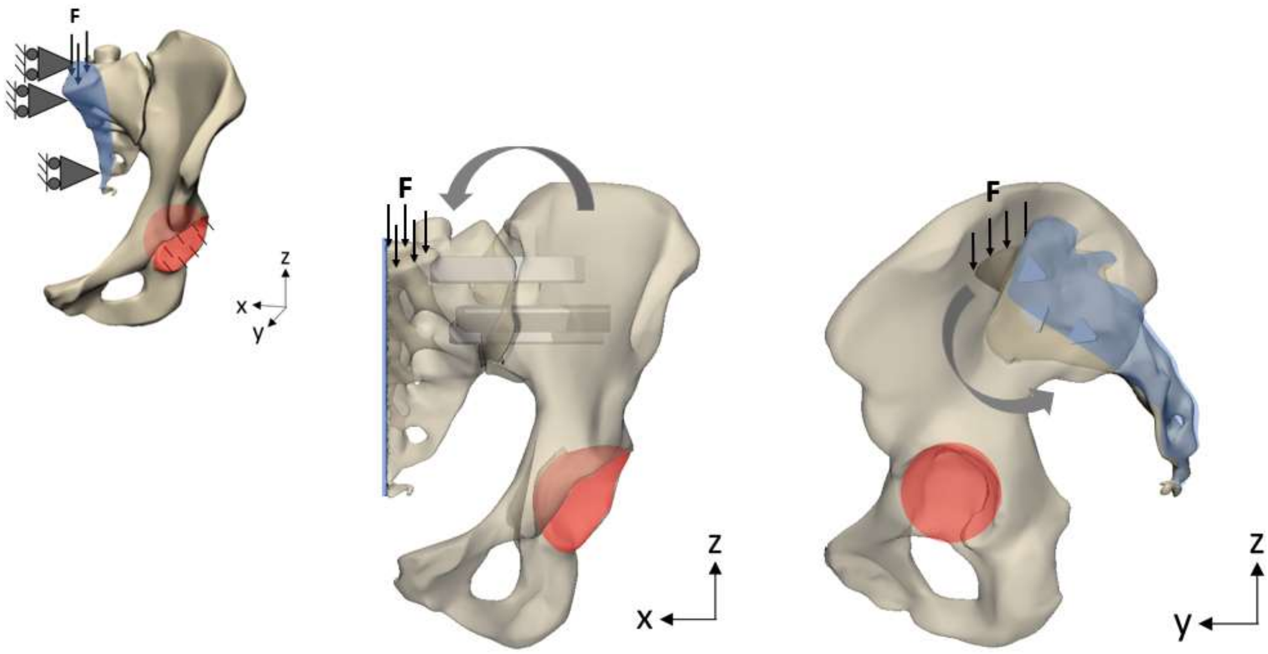

Figure 6-9: Schematic overview of the positioning of the implants in the sacrum model. The difference in geometry is expected to result in greater torsion of sacrum in the pelvis model, given that the force is applied anterior to the implant configuration (see grey arrow right image). Moreover, the pelvis model is fixed at the acetabulum, introducing an additional moment (see grey arrow middle image).

6.4 CONCLUSION

A simplistic version of the pelvis model is made, building upon the validated foam block model from the previous chapter. Shear experiments are conducted for different implant configurations and the range of motion within the joint space is compared. From the results no logic trend could be seen. Therefore, it seems that the different implant configurations do not have a clear influence on the displacements within the SI joint for shear. It is decided to continue with the pelvic model to conduct similar experiments due to time constrains. It is of interest to continue with the pelvis model as the different geometry, material properties and position of forces and boundary conditions could influence the outcome.

7. PELVIC MODEL FOR IMPLANT ANGLE MEASUREMENTS

A pelvis FE model is created, built upon the FE foam block model from the previous chapters. The model consists of the boney structure of the left half of the sacrum and left ilium. Experiments are conducted to determine the influence of implant angle on the stability of the SI joint.

7.1 METHOD

7.1.1 Model construction

A block diagram of the model construction is displayed in Figure 7-1. De 'automized model buildup' is likewise the one from previous chapter.

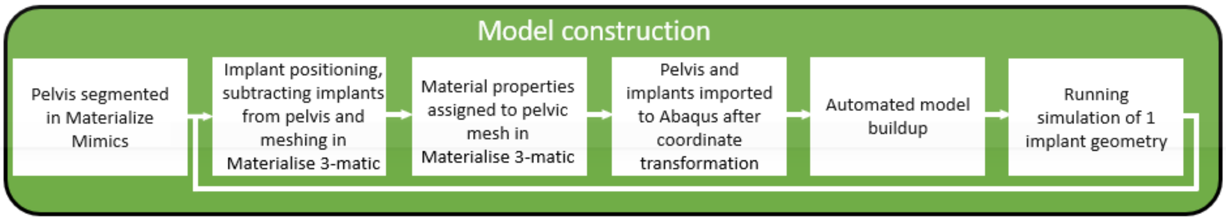

Figure 7-1: Schematic overview of the model construction of the pelvis model.

The pelvis geometry is constructed from computed tomography (CT) (slice thickness 1mm, kVp 120, pixel spacing 0.82mm) of a female with a regular pelvis (length 1,78m, weight 69,5kg, age 34y, no abnormalities except for SIJ dysfunction at left side) using the Somatom Force scanner (Siemens Healthcare, Forcheim, Germany). The cortical bone of the pelvis was automatically segmented in Materialise Mimics with a minimal and maximal thresholding of 226 and 1853 HU. The built-in function Region growing was used to exclude noise and the pixels representing the table the patient laid on, after which Hole fill is used with 2 voxels to add the missing trabecular bone. Large holes were manually filled. The SI joint is segmented as well with a thresholding of minimally -1000 and maximally 226 HU. Again, Region growing is used to exclude noise pixels. The Si joint is subtracted from the pelvic geometry with a Boolean operation and L4 and L5 are subtracted from the geometry with the use of Multiple slice edit. Smooth mask is used to exclude the remainder noise pixels at the edges. Split mask is used to obtain the separate iliac bones and sacral bone. See Figure 7-2 for the CT images, and the resulting segmented sacrum and iliac bones.

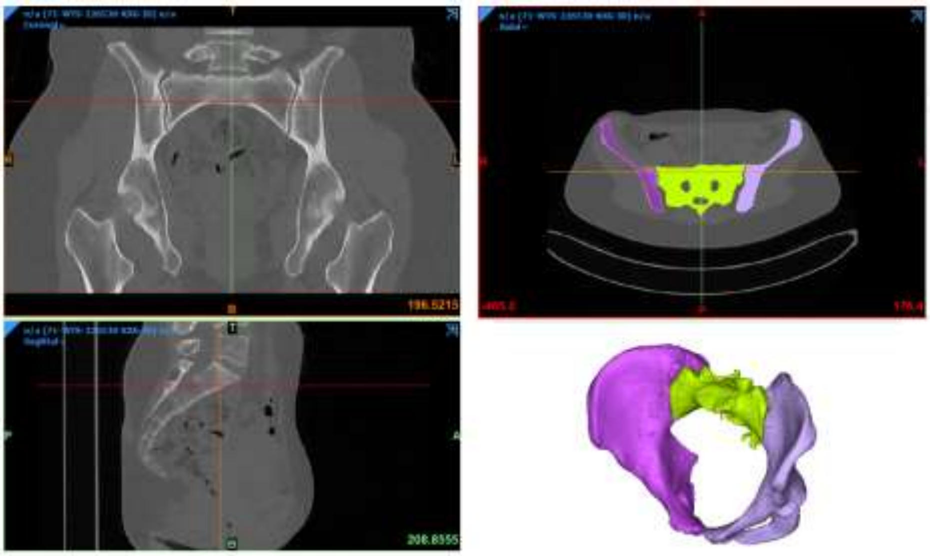

Figure 7-2: CT images and the resulting segmented sacrum and iliac bones.

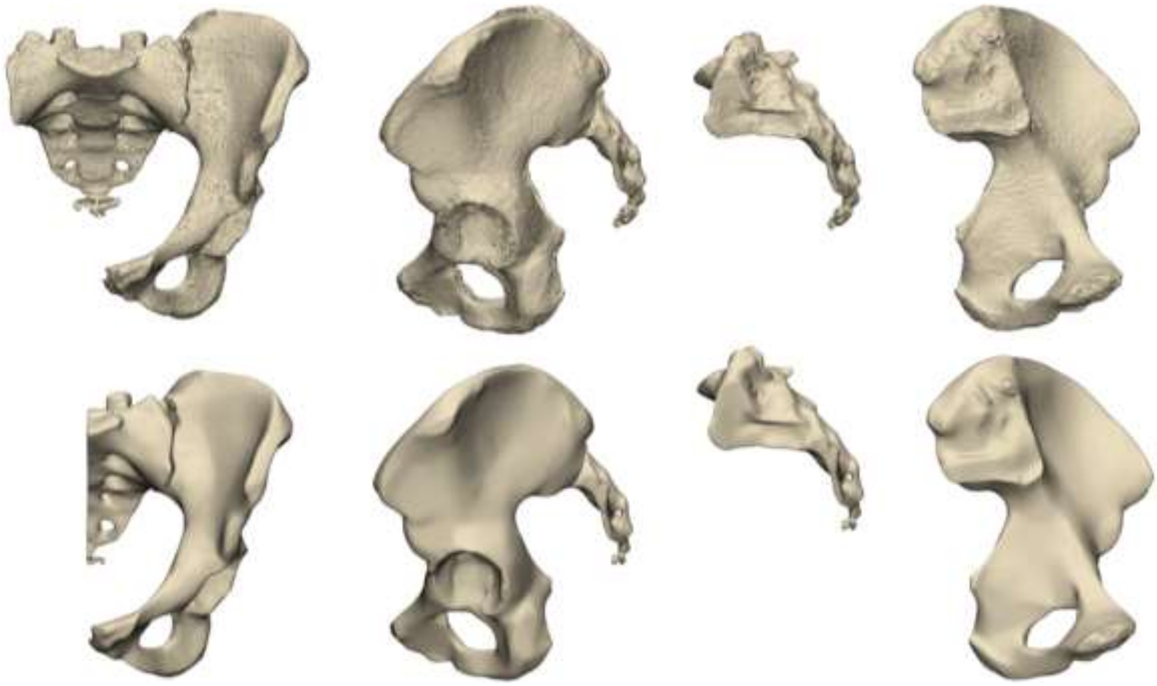

Figure 7-3: Top row: Sacrum and left ilium imported from Materialize Mimics to Materialize 3-matic. Bottom row: Sacrum and left ilium before meshing.

The sacrum and left ilium are imported to Materialize 3-matic and the ilium is subtracted from the sacrum with a clearance of 0.3mm. Both are reduced and smoothed several times to remove surface imperfections caused by the voxel size from the CT scan, whilst keeping the overall geometry. The sacrum is cut in two (over the YZ-plane in the global coordinate frame from Fischer et al. [69]) and the build-in function Remove Spikes is used to remove large irregularities in the ilium and to remove the sharp edges at the spinous tubercles resulting from the cut. In Figure *7-3*: Top row: Sacrum and left ilium imported from Materialize Mimics to Materialize 3-matic. Bottom row: Sacrum and left ilium before meshing.Figure 7-3 it can be seen that the main geometry has been preserved, while the irregularities originated from inaccuracies from the bone segmentation, which complicate meshing, have been removed. The implant STL files used in the research from Kampkuiper et al. [19] are imported and recreated in Solidworks without the hole. The implant configuration is also imported in 3-matic and the mesh is made. This is done by making a union from the sacrum and ilium and creating a nonmanifold with the union and implants. An adaptive surface mesh is made with minimal triangle edge length of 2 and max of 6mm. The interfaces of the union with the implants are selected for the local mesh parameters, for which the max edge length is set to 2mm. Afterwards, the mesh quality is improved with the build in function for which the shape quality is set on high and the max edge length on 6mm. For both the adaptive mesh and the mesh quality improvement, the max geometrical error is set on 0.04mm. After the nonmanifold and afterwards the union is split again, a volume mesh is made with tet4 elements and a max edge length of 6. For the models that do not run with this mesh, the surface mesh is adapted by hand in the areas with sharp edged triangles before generating the volume mesh again. In some models, still some disproportionately small elements were present, see Figure 7-5, but were not removed as they did not seem to cause problems. The total number of nodes was 24219 by average over all models (with a standard deviation of 254) and the total number of elements was 102732 by average over all models (with a standard deviation of 928).

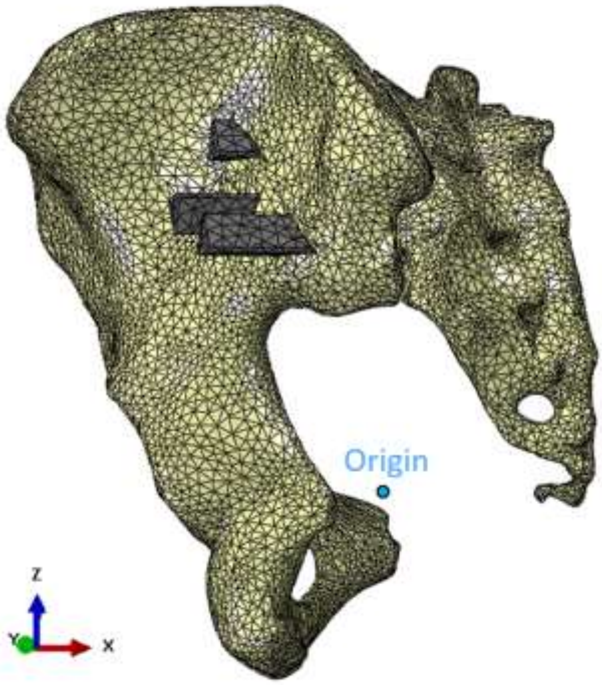

Figure 7-4: Mesh of the sacrum, ilium and implants of implant configuration 00.

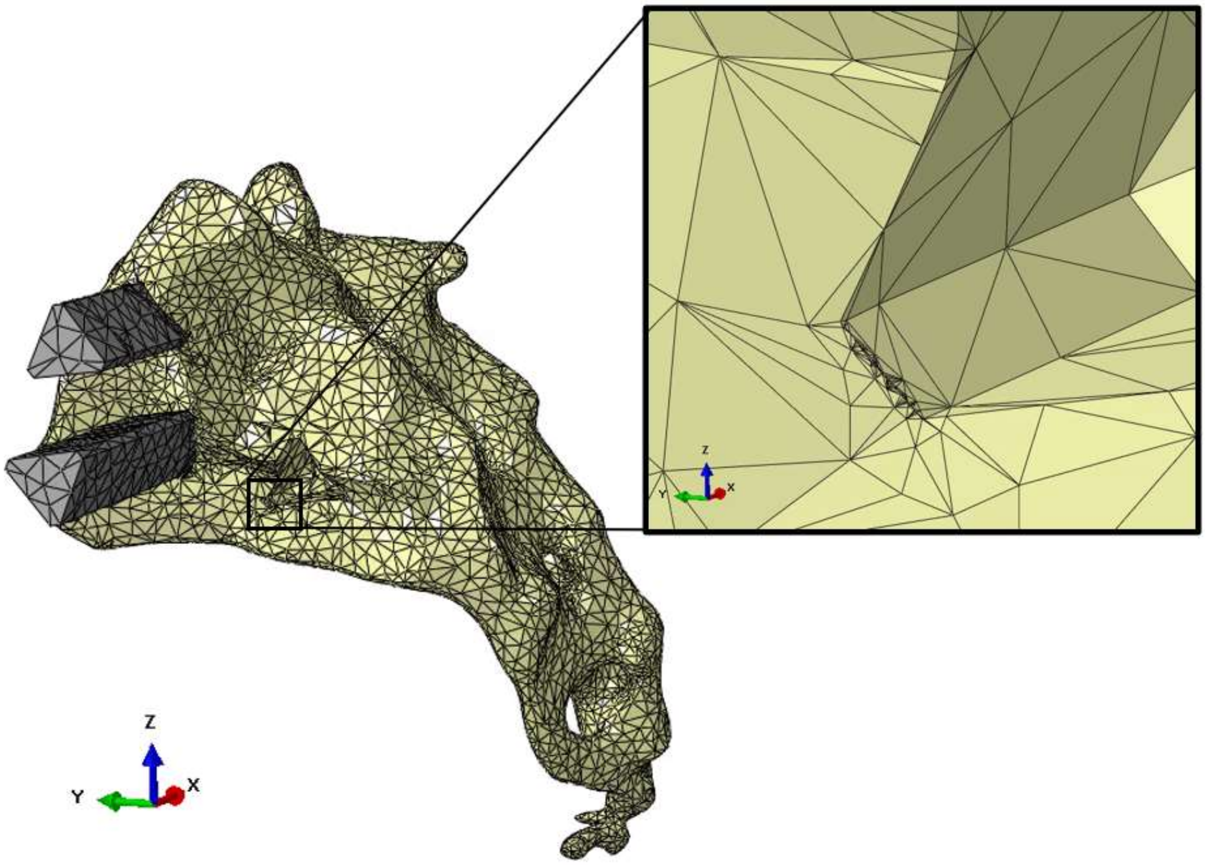

Figure 7-5: Some small elements that were still present but did not cause errors.

The materials are assigned to the mesh in mimics, according to the bone mineral density (see Section 7.1.2). Afterwards, the mesh with material assignment is transformed to a general coordinate system with a Matlab code and exported to Abaqus. The transformation matrix is obtained following the method explained in the paper of Fischer et al. [69]

Furthermore, the model construction is automated again using Python code because of the same reasons explained in the previous chapter (see Section 6.1.1). For the current model construction it is even more important as no planes can be selected anymore for boundary conditions, loadings etc. For example, with automation it is now made sure that nodes for the boundary conditions are automatically selected on being surface nodes laying within a predefined ellipse or box (see Figure 7-6 for the selected nodes of the acetabulum).

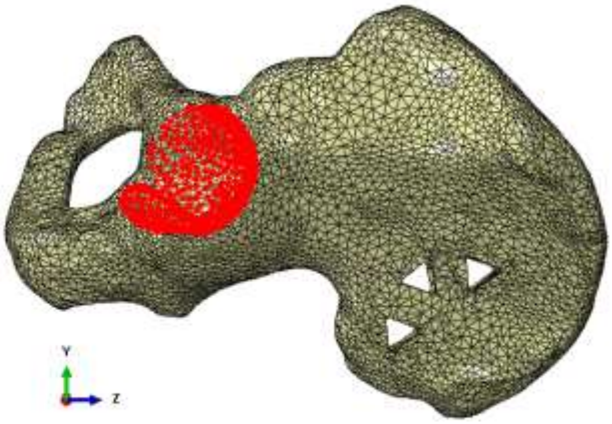

Figure 7-6: Filtered nodes, selected with the use of Python coding, of the ilium to apply a boundary condition on.

As can be seen in the block diagram, a lot of steps need to be repeated manually before using the automated model buildup. The model construction of Figure 7-7 was tried beforehand, but was not possible because the material assignment of the ilium and sacrum cannot be done within Abaqus and needs to be done in Materialize Mimics (see section 7.1.2. Material properties). As the boolean cut feature does not work on a meshed part within Abaqus, the implant subtraction of the sacrum and ilium needs to be done before the mesh is made, and thus a lot of steps need to be repeated for all models, resulting in the block diagram of Figure 7-1.

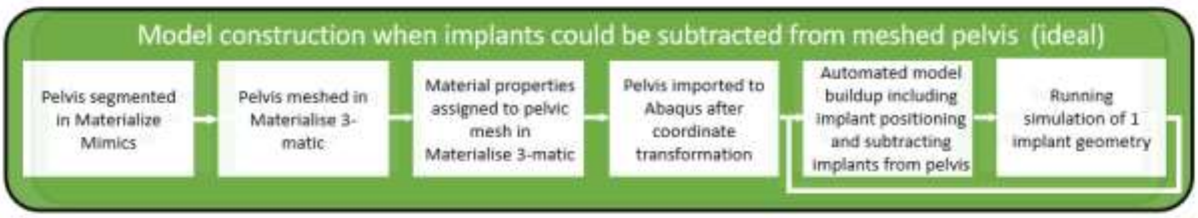

Figure 7-7: Schematic overview of the more ideal model construction of the pelvis model.

Since the implant subtraction of the sacrum and ilium needs to be performed prior to mesh generation, implant positioning and subtraction were conducted using Materialize 3-matic, as shown in Figure 7-1. Initially, there was tried to use the boolean cut feature and to generate the mesh of the implants, sacrum and ilium separately. However, this resulted in penetrating nodes at the implant-bone interface. Although Abaqus resolves intersecting nodes when the 'general contact' feature is used, the level of penetration was too large, leading to simulation failure due to too small or zero-volume elements. While using larger elements resolved this specific issue, the simulation still aborted due to the presence of other low-quality elements. Manually adjusting all problematic elements for each model was not feasible due to time constraints. The use of really small elements, did create high quality elements, but significantly slowed down the model to the point where running the simulation was impractical. Therefore, linear tetrahedral elements were chosen over quadratic tetrahedral, as linear tetrahedral elements offer greater geometric stability. A more detailed discussion of the implications of these decisions is provided in section 7.3. Due to time constraints there was chosen to continue.

7.1.2 Material properties

The CT images are used to calculate a calibration function relating the gray value (HU) to the Bone Mineral Density (BMD) of the bones following the method described by of Eggermont et al. [70]. The calibration was based on the histogram of gray values, which was divided into ten sections, resulting in ten distinct material properties being assigned. The calibration function is stated in Equation 7-1.

$$BDM = \frac{HU - 4.3835}{1.2071}$$ Equation 7-1

The bone density (ρ) and Elasticity modulus (E) used in the model are calculated using the method of Keyak et al. [71] and those equations are stated in Equation 7-2 and Equation 7-3.

$$\rho = 0.0633 + 0.001 \cdot BDM \cdot 0.887$$ Equation 7-2

$$E = 14900 \cdot \rho^{1.86}$$ Equation 7-3

A minimal Young's modulus of 10 was used in order to prevent difficulties with convergence. In Table 7-1 one can see an overview of the average (with standard deviation) minimal, median and maximal Young's modulus values of the sacrum and ilium of all models.

Table 7-1: Average and standard deviation of the minimal, peak of the grey value histogram, median and maximal Young's modulus [Mpa] values of the sacrum and ilium of all models.

	Sacrum Young's modulus [Mpa]				Ilium Young's modulus [Mpa]			
	min	peak histogram	median	max	min	peak histogram	median	max
Mean of all configurations	10	1714	3656	13061	71	1308	4795	15723
Std of all configurations	0	15	31	154	50	164	193	71

For the implants, an Young's modulus of 113800 Mpa is used and a poisons ratio of 0.342 [62] [63], these are the same values used as in the foam block model.

7.1.3 Tested configurations

The stability of the implant connection will be tested for the same implant angles as in previous chapter and therefore again Table 6-3 displays the position of each implant per experiment. The implants are rotated around the same axis as the implants in the previous chapter were rotated around, and the point of rotation is taken to be in the middle of the SI joint. The reasoning behind this is already explained in previous chapter (see section 6.1.3 Tested configurations). Table 7-2 shows the position of each implant in 'neutral position' for the pelvis experiments (experiment set 0, experiment 0 in Table 6-3), which is different from the 'neutral position' of the implants in the foam block model (see Figure

7-8). The neutral position of the pelvis model is determined by an orthopedic surgeon by means of a virtual surgical planning [19], ensuring all tested implant angles are positioned realistically. A visualization of the neutral position of the implants together with the maximum tested angle per implant can be seen in Figure 6-2.

Table 7-2: Coordinates of the implants in neutral position in the Pelvis model.

	X1 [m]	Y1 [m]	Z1 [m]	Rx1 [°]	Ry1 [°]	Rz1 [°]
Implant 1	-0.053	-0.095	0.126	22.258	0.232	-0.468
Implant 2	-0.059	-0.097	0.059	-41.254	0.237	-0.465
Implant 3	-0.054	-0.118	0.098	22.260	0.237	-0.464

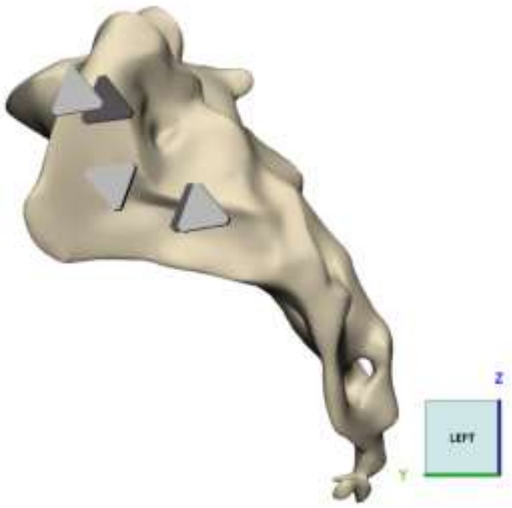

Figure 7-8: 'Neutral position' of the implants in the pelvis model (dark grey implants) in comparison to the ‘neutral position’ of the implants in the foam block model (light grey implants). Middle implants for the foam block model and pelvis model are aligned.

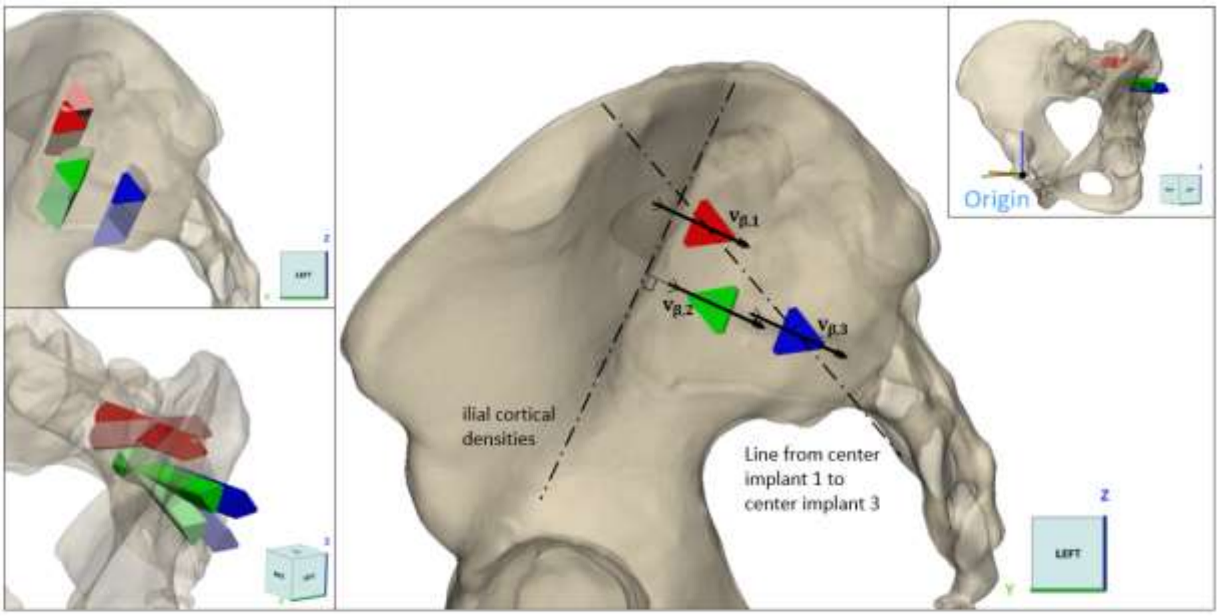

Figure 7-9: Neutral position of the implants in the pelvis in global coordinate system (center image) with the local coordinate frame of the pelvis (top right image) and the neutral position of the implants together with the maximum tested angle per implant (left images). Note that the same local coordinate system for the implants is used as in previous chapter (see Figure 6-2).

7.1.4 Loading ang boundary conditions

A vertical loading of F=800N is applied at the top surface of the sacrum, modeled as a pressure with total force equal to F. The surface of the acetabulum is fully constrained to replicate two leg stance and the side surface of the sacrum is constrained translation in X and rotation in Y and Z. See Figure 7-10. Although this representation of two leg stance is not perfect, it will be used as a start. The loading of 800N is chosen, as this is used by one of the models from literature, analyzed in Section 4.2, with similar boundary conditions.

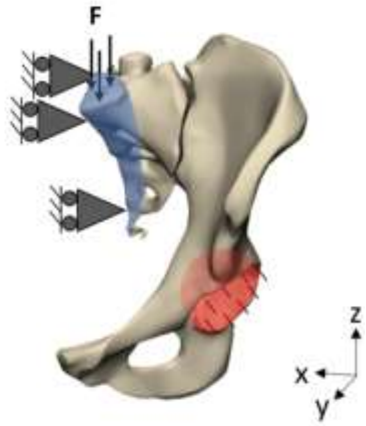

Figure 7-10: Loading and boundary conditions of the pelvis model.

It was considered to change the loading direction to be perpendicular on the sacral promontory as displayed in Figure 7-11, as it was uncertain what replicated reality most. It is decided to use the vertical loading as this is also used in two of the three models found in literature analyzed in Section 4.2.

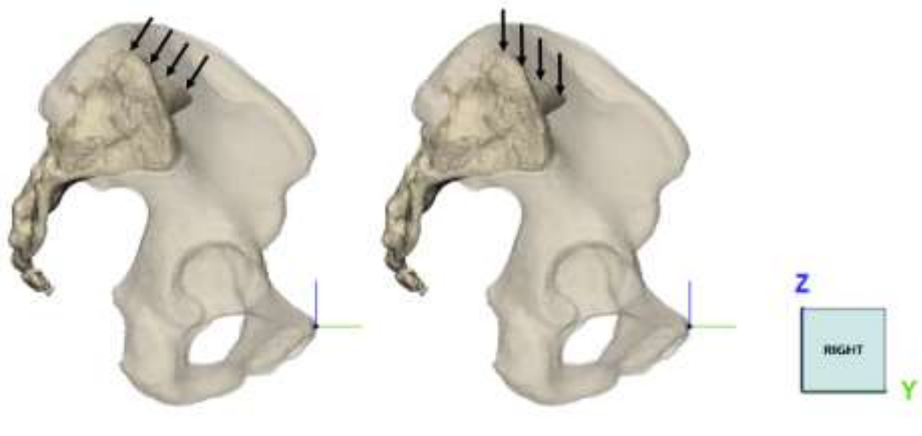

Figure 7-11: Left: loading direction perpendicular on the sacral promontory, right: vertical (negative Z) loading direction currently used.

7.1.5 Result analysis

The results are analyzed in the same way as previous chapter. See section 6.1.5.

Note that the 7 points selected for the relative displacement analysis are different for the pelvis and foam block model, as the positioning of the implants is also different (see Figure 7-8). The 7 points for the pelvis and foam block model are selected to be in similar position with respect to the implants and the articular surface. See Figure 7-12.

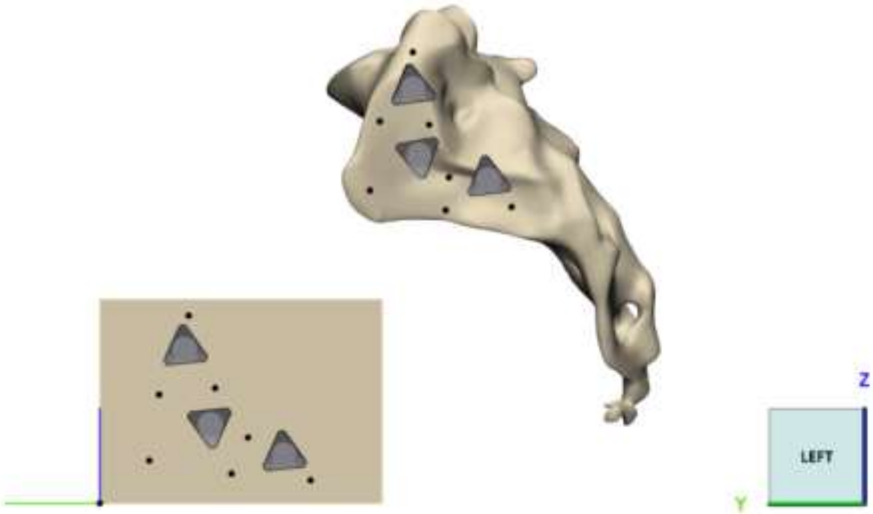

Figure 7-12: Positioning of the 7 displacement analyzation points in the foam block model and the pelvis model.

7.2 RESULTS

Figure 7-13 shows the original and deformed mesh of the model for the neutral implant configuration during shear loading. It can be seen that the sacrum flexes forward and there is lateral bending of the ilium. The overall stress distribution within the ilium and sacrum is visible in Figure 7-14. Stress concentrations are visible at iliac fossa near the pelvic ring, and at the top of cutting plane of half the sacrum. Additionally in Figure 7-15, formed gaps can be observed between the bone and the implants at several areas, marked by the arrows.

Figure 7-16 shows the stress distribution within the sacrum at the SI joint gap for the neutral implant configuration under shear loading. In Figure *7-17* the stress distribution within the implants for the neutral implant configuration is shown. The results indicate that the maximal stresses occur at the joint gap, with tension at the top of the implants and compression at the bottom, indicating bending.

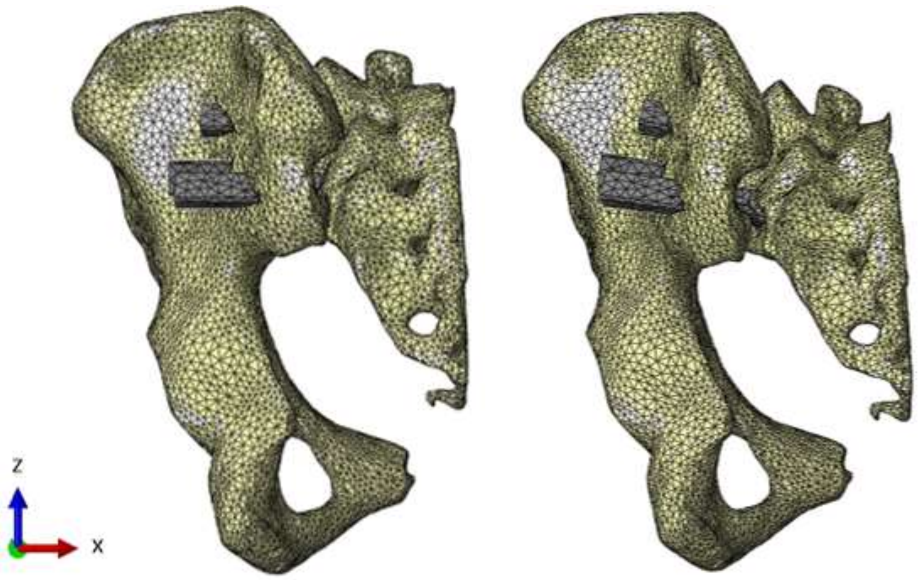

Figure 7-13: Undeformed (left image) and deformed (right image) mesh of the model for the neutral implant configuration under shear loading. (Deformation scale factor = 100)

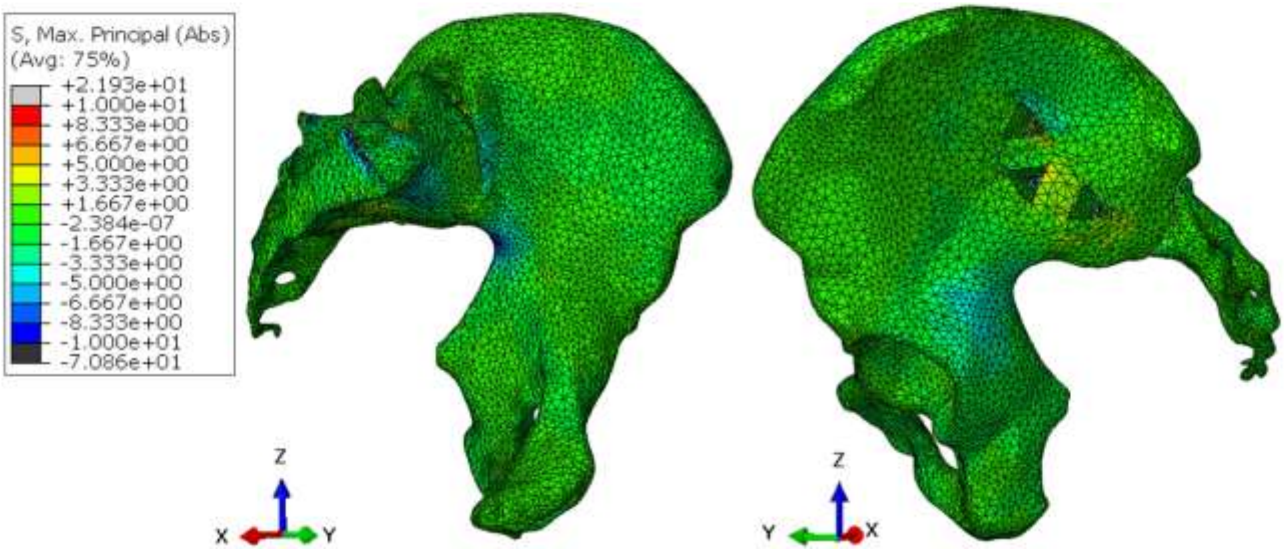

Figure 7-14: Stress distribution [MPa] within the sacrum and ilium for the neutral implant configuration.

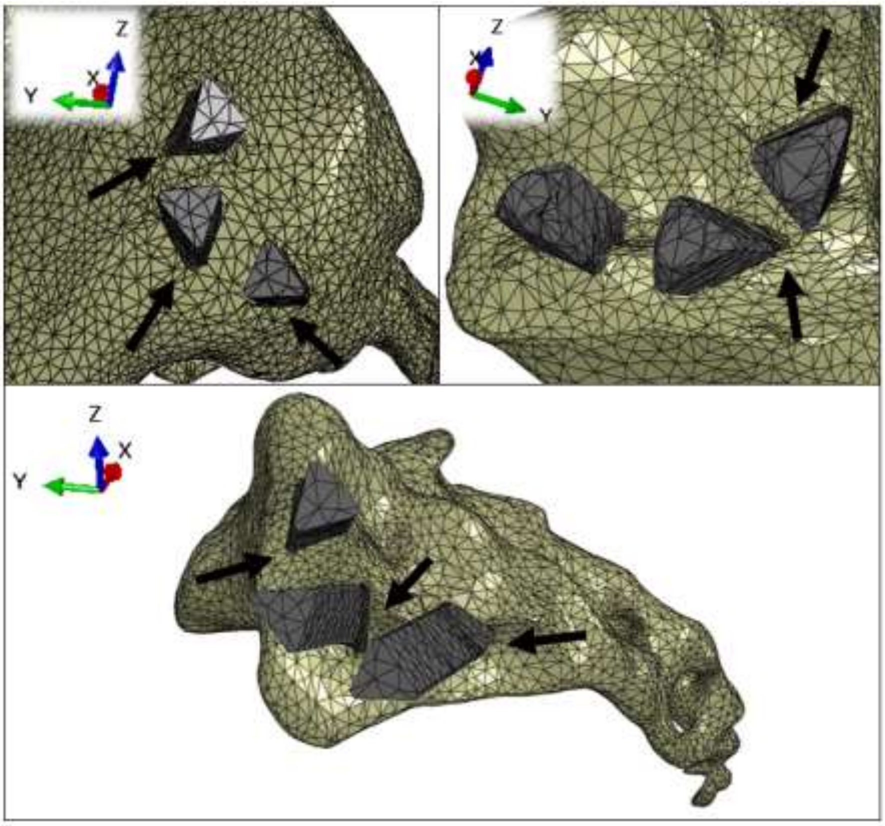

Figure 7-15: Deformed mesh of the sacrum at the SI joint gap (bottom image), ilium at the implant inlet (top left image) and ilium at the SI joint gap (top right image) for the neutral implant configuration during shear loading. Formed gaps between the bone and implants are marked by arrows. (Deformation scale factor = 250.)

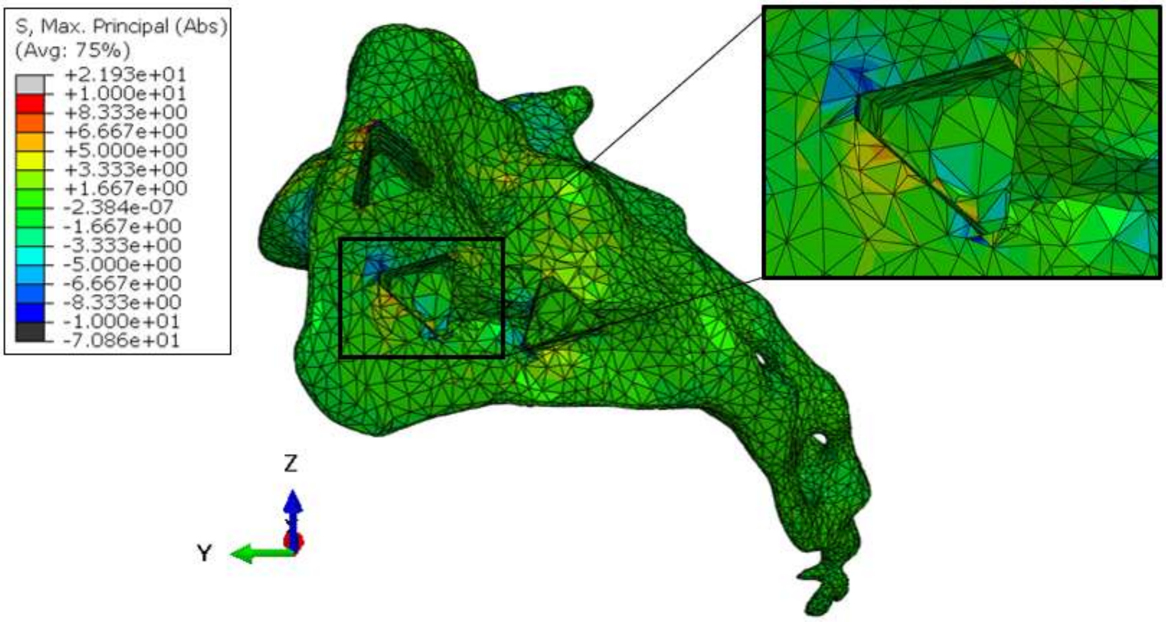

Figure 7-16: Stress distribution [MPa] within the sacrum at the SI joint gap for the neutral implant position during shear loading.

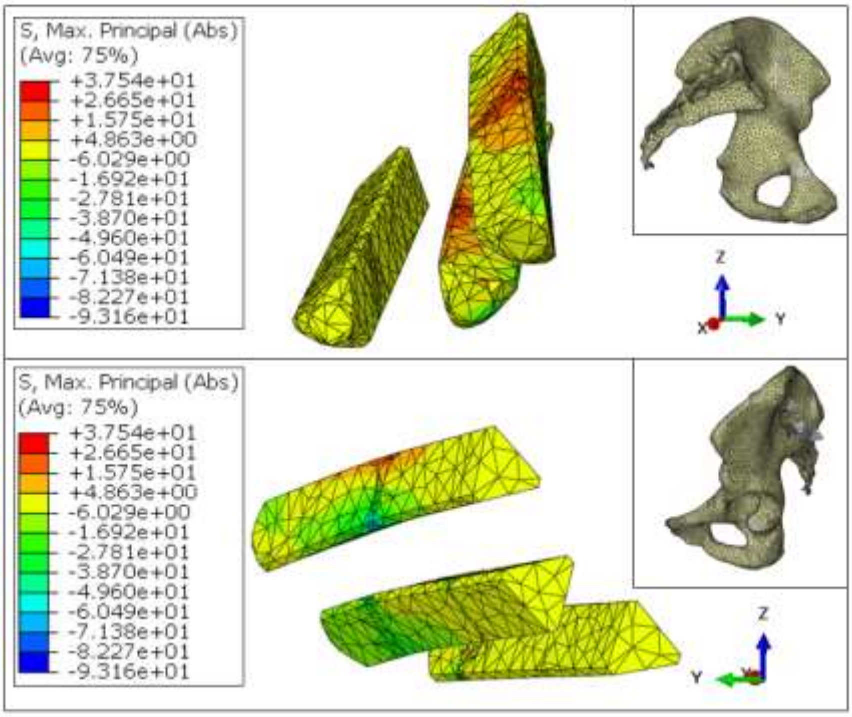

Figure 7-17: Stress distribution [MPa] within the implants for the neutral implant configuration during shear loading for two different global coordinate orientations (in the top right images, the orientation within the pelvis model is displayed).

All other implant configurations show similar gapping and stress distributions.

In Figure 7-18 a vector plot of the displacements of the sacrum minus the displacements of the ilium in YZ-plane at several positions on the sacrum can be seen, for the different experiments. In the figure minimal difference in displacement direction is visible between the different implant configurations, and also minimal difference in vector length, indicating minimal difference in displacement magnitude.

In Figure 7-19 the minimal, median and maximal displacement in 3D direction of the seven nodes displayed in Figure 7-18 are plotted in a bar graph for the different implant configurations. One can see that the range of motion is relatively small, and the differences in range of motion are also relatively small as was already expected from Figure 7-18. When one does look at the differences, it can be seen that for both experiment sets, experiment b (the more angled configuration) has a bigger displacement. Furthermore, implant configuration 00 has the lowest displacements.

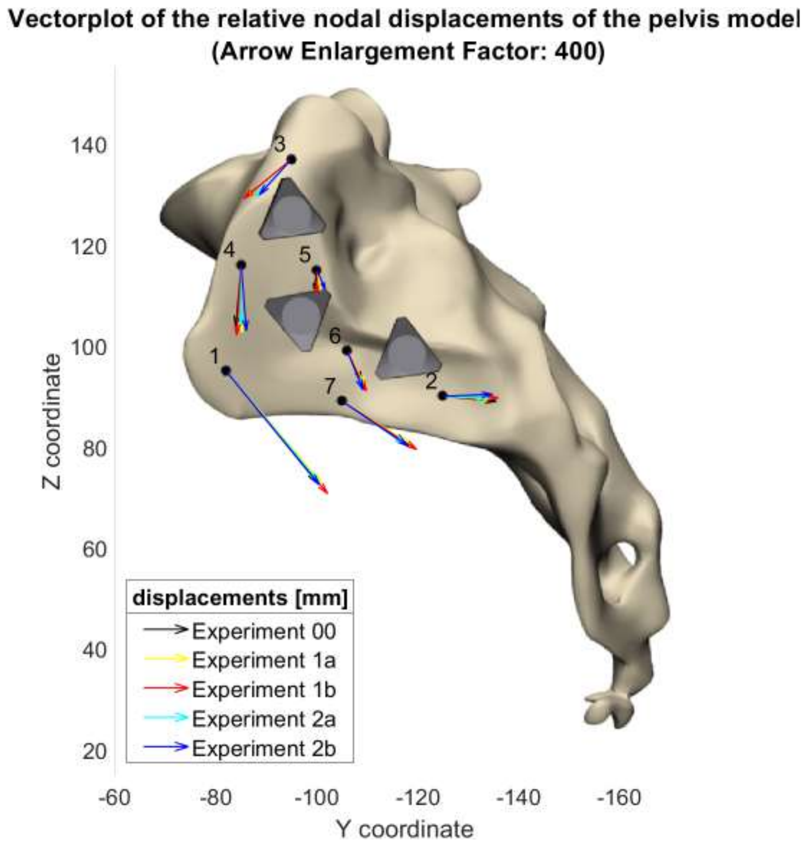

Figure 7-18: Vector plot of the relative nodal displacements of the sacrum block minus the nodal displacements of the ilium block for seven opposite nodes in the YZ plane of the pelvis model.

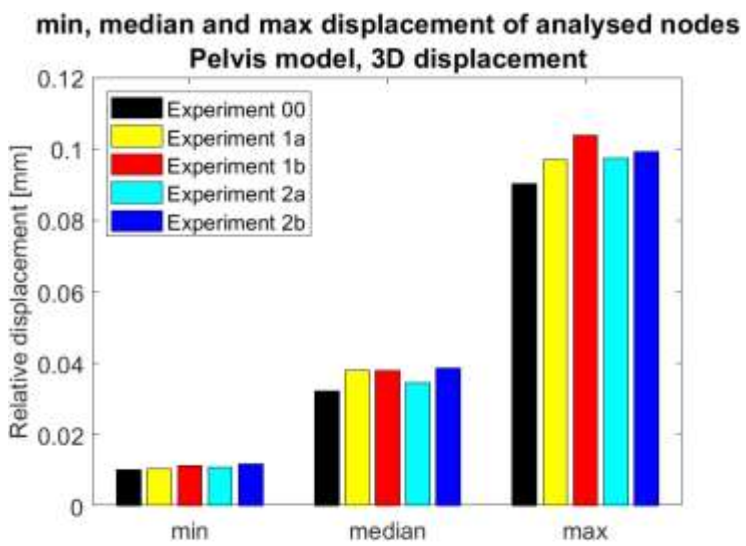

Figure 7-19: Minimum, median and maximal relative displacement in 3D of the analyzed nodes of the pelvis model. (The displacements are again defined as the nodal displacements of the sacrum minus the nodal displacements of the ilium for opposite nodes.)

7.3 DISCUSSION AND RECOMMENDATIONS

A pelvis model is made consisting of the boney structure of half the pelvis. Shear experiments are conducted for different implant configurations and the range of motions within the joint space are compared.

7.3.1 Interpretation of the results

The deformed meshes and stress distributions within the models were displayed. It can be seen that the sacrum flexes forward and there is lateral bending of the ilium. Both were expected as was explained in Section 6.3. The gap forming is also as expected due to the rotating movement of the sacrum, while the implants are fixated by the ilium: similar gap forming is found as was the case for the foam block torsion experiments (see Section 5.2). The stress distributions confirm this. Where the implants are considered to push into the bone for example, compression within the blocks can be found. Furthermore, the bending within the implants is expected from the flexing motion of the sacrum and therefore the lateral bending of the implants.

Vector plots of the nodal displacements of the sacrum block minus the nodal displacements of the ilium block for seven opposite nodes within the SI joint space are made. From these plots it could be seen that there is minimal difference in displacement direction, as well as minimal difference in vector length, and thus displacement magnitude. Furthermore, bar graphs were made in which one could see the minimum, mean and maximal displacement on the analyzed nodes. From this figures it could be seen that the displacements are relatively small, but for both experiment sets, experiment b (the more angled configuration) has a bigger displacement in 3D. Furthermore, experiment set 00 has a low displacement. This may indicate that angled implant configurations behave unfavorable over non angled implant configurations.

Comparing the results from the pelvis model to the results of the foam block model, it can be seen that the displacement direction of the pelvis model is different than that of the foam block model. This was already expected due to the difference in geometry (see section 6.3 again). Furthermore, the magnitude of displacement is lower than that is observed in the foam block model. This can be explained due to the higher Young's modulus that is used in the pelvis model. Additionally, there is relatively more deformation of the ilium expected in the pelvis model due to the larger distance to the fixture, leading to reduced relative displacements within the SI joint. The comparison of the influence of the different implant configurations on the overall 3D stability similar for both models: for both experiment sets, implant configuration a has less, median and maximal displacement than implant configurations b and implant configuration 00 had the least, median and maximal displacement. The only exception to this pattern is seen in the foam block model for minimal displacements.

Again, comparison to results from literature is not possible, as the influence of alike angled implant configurations is not tested in literature yet. Furthermore, the pelvis models described in section 4.2 all contain ligaments, resulting in more difficulties for proper comparison in range of motion.

7.3.2 Limitations of this research

As this model is built upon the simplified model of Section 6, that was built upon the model validated with the results from Freeman et al from Section 5, unrealistic assumptions that have a large impact are not expected (although one must be cautious again regarding the limitations discussed in Section 5.3.2 and Section 6.3.2, which will not be repeated here). Moreover, the automated construction of the model eliminates the potential for more errors again that might arise from manual reconstruction of the models for different implant configurations. However, there are a few adaptations made from the validated model which are not validated.

The first is the adaption form the boolean cut feature to the nonmanifold feature for the implant subtraction from the sacrum and ilium. However, the non-manifold feature generates the mesh for both the implant and the sacrum and ilium simultaneously, with a smaller element size at the point of interface, resulting in a more accurate fit compared to using the Boolean cut feature previous to meshing. This hypothesis is supported by the exclusion of the error as explained in Section 7.1.1 'Model construction'.

The second adaption is the transition from quadratic tetrahedral elements to linear tetrahedral elements. This could result in inaccuracies, for example in bending deformation, because linear elements can only represent a constant strain field [68]. Furthermore, one must notice that warnings about distorted elements are more likely to cause inaccuracies using linear elements [72]. With the loading and boundary conditions used earlier in this section, it was tested to see whether the change from quadratic to linear elements indeed resulted in less motion and it was observed that the model with linear elements resulted indeed in less motion than the model with quadratic elements. Unfortunately, the implant-bone interface was made with the Boolean cut feature for the quadratic element model, while the implant bone interface for the linear element model was made with the non-manifold feature. It is therefore not certain whether these results were representative.

The third change is the transition from homogeneous to nonhomogeneous material properties. Ten different material properties were assigned to various regions within the ilium and sacrum, based on the BMD from the CT scan used to create the model. This makes the model more realistic compared to the foam block models. However, real bone consists of more than just 10 different material properties, so some inaccuracies compared to reality still exist. For instance, at the edges of the bone, incorrect material properties can be assigned when part of an element is, due to mesh inaccuracies, positioned outside of the boney region. As the density is averaged over the element, a lower density is computed and thus other material properties are assigned. Note that a smaller mesh size, will thus also increase the accuracy for this problem.

7.3.3 Recommendations

Besides the recommendations that were already discussed in Section 5.3.3 and Section 6.3.3, that might have an influence on this section as well, some additional recommendations can be made.

Firstly, it is advised to spend more time on analyzing the influence of the transition from quadratic tetrahedral elements to linear tetrahedral elements. It was shown that there is reason to believe that the model using linear elements is stiffer than the model using quadratic elements. However, the analyzation done in the section above has some limitations wherefore it is unsure to what degree it is representative. If this transition indeed has a lot of influence on the results, it is recommended to put effort in making the model run with quadratic tetrahedral elements, to get rid of this effect. Another solution to minimize this effect, is to refine the mesh. This was not tested here, due to time constrains.

Furthermore, it is recommended to investigate the influence of a larger variety of material properties on the results. Note that this possibly must be done in combination with a mesh refinement as explained above.

Finally, one must note that the recommended, more detailed, analysis on material failure given in section 5.3.3, will be even more complicated than already stated due to additional difficulties caused by the transition from homogeneous to nonhomogeneous material properties.

7.4 CONCLUSION

A FE Pelvis model is made, building upon the validated foam block model from the previous chapters. Shear experiments are conducted for different implant configurations and the range of motion within the joint space is compared. It could be seen that the displacements are relatively small, even as the differences in displacements between the varying implant configurations. For both experiment sets, experiment b (the more angled configuration) had a slightly bigger displacement in 3D. Furthermore, experiment set 00 had the lowest displacement. This may indicate that angled implant configurations behave slightly more unfavorable over non angled implant configurations.

8. DISCUSSION AND RECOMMENDATIOND

The research question of this study was 'To what extend do implant angles influence the stability of the SI joint for lateral transiliac SI joint fusion while taking into account patient anatomy and operative accessibility?' To answer this research question, the goal of this study was 'To develop, validate with literature and use a Finite Element Model from the pelvis to determine the optimal configuration of the implants for SIJF, while taking into account patient anatomy and surgical accessibility.'

To be able to work forward from a simple, validated model before diving into the complex geometry of the pelvis, it is decided to begin with modelling the experiments conducted on a physical foamblock model found in literature [5]. The physical foam block model from Freeman et al. consisted of two blocks, representing the sacrum and ilium, that were connected by three implants. This model is addapted to examine the influence of different implant angles on the stability of the SI joint within a simple geometry. Lastly, a pelvis FE model is created, built upon the FE foam block model. The pelvis model consists of the boney structure, with nonhomogeneous material properties, of the left half of the sacrum and left ilium. Experiments were conducted to determine the influence of implant angle on the stability of the SI joint. This is done by conducting shear experiments on different implant configurations to determine the influence of implant angle on the stability of the SI joint. 5 different implant configurations were tested: one parallel configuration, two in which only the middle implant is rotated (experiment set 1) and two in which all implants are rotated (experiment set 2).

8.1.1 Interpretation of the results

Minimal differences in displacement direction and magnitude were observed for varying implant configuration. However, for both experiment sets it could be seen that, overall, the more angles implant configuration had less stability than the less angled implant configuration. Furthermore, the neutral implant configuration had the most stability. This may indicate that angled implant configurations behave unfavorable over non angled implant configurations .

8.1.2 Limitations of this research

With the development of the pelvis FE model, which incorporated the boney structures with nonhomogeneous material properties, a significant step toward creating a realistic pelvis model is made. This model was created, building the validated foam block model, replicating the experiments from Freeman et al. [5]. However, validation of the foam block model is partly done as was already explained in Section 5.3: The validation using Freeman's model turned out to be quite difficult because Freeman had not done many experiments. Statistically speaking, no proper conclusions could be drawn. To get a better indication about the validity of the foam block model, additional experiments are conducted that can be found in APPENDIX C . In this appendix section, the influence of implant depth in the models used is investigated, as it is proven that deeper placed implants have better stability [6]. In the appendix section it could be seen that the minimal and median displacement is less for the deeper placed implant configuration (which is as expected), but the maximal displacement is more for the deeper placed implant configuration (which is unexpected, note however that these differences are very small). Looking at the overall displacements within the model, it was observed that the maximal displacement of the sacrum was less for deeper placed implants than for the original implant configuration (which is as expected). This indicates that the decision of data analysis is of real importance.

Besides the validation of the model, no soft tissue such as ligaments and cartilage is incorporated in the model which could also have significant influence on the results. For example, Bruna-Rosso et al. suggest that their unexpected results indicating that the addition of a second implant does not increase stability, can be explained by the modification to the simulated ligament damage to enable implant insertion, considering the ligaments crucial role on the SIJ biomechanics [8]. They refer to a book from Rahl, which recommends favoring trajectories that preserve the integrity of the IOL [73]. Furthermore, the boundary condition of two leg stance is really simplified from reality. For example, the acetabulum is currently fixed in all translations and rotations, while in reality it can rotate (even though not freely) to a certain degree around the femur head. This allowance for rotation could reduce the stresses within the model. Additionally, the current model represents only half of the pelvis. While this was sufficient for the boundary conditions and loadings applied in this study, as symmetry could be assumed, antisymmetric behavior, such as implementation of unilateral implants, may differ. Additionally, the pelvis model is based on the anatomical data of only a single patient. Although this patient is selected by a surgeon to be 'average', this patient may not be representable for other patients given the significant variability in patient anatomy (see section 2.1, [14] [15] [16]). This variety could influence the results as it is already proven that the differing anatomy of male and female pelvis influences the stability of SIJF [35].

Furthermore, only shear is tested in this research. It is possible that other load cases give other results regarding implant stability. As a first step towards the investigation of other load cases, the influence the different implant configurations on the displacement is tested for torsion (flexion) in APPENDIX D Although, from these results no clear trends can be observed, it is expected that implants in multiple directions are overall better for a variety of load cases in different directions. Additionally, from the results of Freeman, it was shown that cyclic loading has an influence on the implant stability, which was also outside the scope of this research. Furthermore, in this study a start was made to access the influence of anatomically feasible implant angles, but also other implant angles are possible to use for SIJF within the anatomy of the SI joint, which could give other results.

Finally, one must note that it is still uncertain what is the precise cause of implant loosening. In this study, the assumption was made that a more stable implant configuration would result in less implant loosening, which is in line with the results of Kohli et al. [2]. However, more factors may influence the implant loosening, which are not taken into account in this study. For example Kohli et al. also state that many factors were found to combine to affect the implant loosening, including loading time, the type of implant and the material being used [2].

8.1.3 Recommendations

Given these limitations, further research should focus on improving the resemblance of the FE model with reality. Firstly, it is recommended to add soft tissue such as ligaments and cartilage. In APPENDIX A the material properties found in the three models from literature discussed in Section 4.2 are stated, but due to time constrains this was not further investigated. Furthermore, it is recommended to make the two leg stance boundary condition more realistic. This could for example be done by fixing all translations of the acetabulum, while a progressively increasing resistance should be applied on the rotations. This way, the rotations are not free, but also not completely fixed, like is the case in reality. Additionally, given the significant variability in patient anatomy, it is advisable to model several representative anatomies to better understand the influences of these differences.

Furthermore, only shear is tested in this research, although it is possible that other load cases give other results regarding implant stability. Therefore, it is recommended that more load cases like flexion-extension, lateral bending, and axial rotation are tested, as well as cyclic loading. Additionally, bigger variety of implant angles, also rotating around other axis, within anatomical possibilities for SIJF should be tested. Furthermore, further validation of the pelvis model with other FE studies or cadaver studies is advised as the FE pelvis model was not validated in this study. Note that the addition from the other half of the pelvis is might needed when further elaborating the model. This is for example needed when asymmetry is tested, other loading conditions are tested (for example for lateral bending and axial rotation) and validation with cadaver experiments/other FE models from literature is done.

Finally, it is recommended to search in literature to what extent implant spacing and implant depth is of importance in SI joint stability. If the angled implants have zero to minimal negative effect, and deeper placed implants and further spaced implants have a lot of positive effect on the SI joint stability, it is recommended to use the angled implant configuration if the implants can be deeper placed and with more spacing.

9. CONCLUSION

The research question of this study was 'To what extend do implant angles influence the stability of the SI joint for lateral transiliac SI joint fusion while taking into account patient anatomy and operative accessibility?' To answer this research question, the goal of this study was 'To develop, validate with literature and use a Finite Element Model from the pelvis to determine the optimal configuration of the implants for SIJF, while taking into account patient anatomy and surgical accessibility.' As a first step, FE simulations were conducted to replicate experimental SI stability measurements (shear and torsion) for varying implant configurations as reported in the literature. The physical model from literature consisted of two blocks, representing the sacrum and ilium, connected by three implants. The FE model showed a trend that was similar to what was reported in literature. This FE model is addapted to examine the influence of different implant angles on the stability of the SI joint within a simple geometry. Five clinically relevant implant configurations were selected with three implants: one parallel configuration, two in which only the middle implant is rotated and two in which all implants are rotated. Each configuration was arranged in a triangular pattern with consistent spacing between the implants at the SI joint gap. The configurations were chosen based on patient anatomy and surgical accessibility, and the motions at the SI joint were calculated under shear loading conditions. These analyses served as the foundation to create a more anatomically realistic FE model of a patient. The patient model consists of the boney structure, with nonhomogeneous material properties based on the bone mineral density, of the left half of the sacrum and left ilium. In this patient model, similar implant configurations are tested and the motions at the SI joint were again calculated under shear loading conditions. The results showed minimal differences in both displacement direction and magnitude across the different configurations for both the foam block and the pelvis model.

REFERENCES

During the writing of this thesis, ChatGPT was used in order to provide the basis for some of the coding used during this research. Furthermore, ChatGPT was used to provide inspiration and improve the formulation of the content written by the author. This was done with the goal of enhancing the overall quality of writing.

After the tool was used, the author analysed, reviewed, and edited the responses. The author takes full responsibility for the content of the work.

[1] SI-Bone, "iFuse Implant System," SI-Bone, [Online]. Available: https://si-bone.co.uk/patients/si-joint-pain-treatment/ifuse-implant-system. [Accessed 07 08 2024].

[2] N. Kohli, J. C. Stoddart and R. J. van Arkel, "The limit of tolerable micromotion for implant osseointegration: a systematic review," *Scientific reports,* vol. 11, no. 1, pp. 1-11, 2021.

[3] L. Zhang, Y. Peng, C. Du and P. Tang, "Biomechanical study of four kinds of percutaneous screw fixation in two types of unilateral sacroiliac joint dislocation: A finite element analysis," *Injury,* pp. 2055-2059, 2014.

[4] Y. Shih, B. Beaubien, Q. Chen and J. N. Sembrano, "Biomechanical evaluation of sacroiliac joint fixation with decortication," *The Spine Journal,* pp. 1241-1249, 2018.

[5] A. L. Freeman, J. E. Bechtold and D. W. Polly, "Biomechanical Stability of the Sacroiliac Joint with Differing Implant Configurations in a Synthetic Model," *International Journal of Spine Surgery,* vol. 15, no. 5, pp. 853-861, 2021.

[6] D. P. Lindsey, A. Kiapour, S. A. Yerby and V. K. Goel, "Sacroiliac joint stability: Finite element analysis of implant number, orientation, and superior implant length," *World Journal of Orthopedics,* vol. 9, no. 3, pp. 14-23, 2018.

[7] H. Soriano-Baron, D. P. Lindsey, N. Rodriguez-Martinez, P. M. Reyes, A. Newcomb, S. A. Yerby and N. R. Crawford, "The Effect of Implant Placement on Sacroiliac Joint Range of Motion, Posterior Versus Transarticular," *Spine Biomechanics,* vol. 40, no. 9, pp. 525-530, 2015.

[8] C. Bruna-Rosso, P.-J. Arnoux, R.-J. Bianco, Y. Godio-Raboutet, L. Fradet and C.-É. Aubin, "Finite Element Analysis of Sacroiliac Joint Fixation under Compression Loads," *International Journal of Spine Surgery,* vol. 10, 2016.

[9] N. F. Kampkuiper, F. F. Schröder, E. E. Hekman, M. A. Koenrades and J. M. Nellensteijn, "Letter to the Editor: “Biomechanical Stability of the Sacroiliac Joint With Differing Impact Configurations in a Synthetic Model"," *International Journal of Spine Surgery,* vol. 17, no. 1, pp. 162-163, 2022.

[10] A. L. Freeman, J. E. Bechtold and D. W. Polly, "Response Letter," *International Journal of Spine Surgery,* vol. 17, no. 1, pp. 164-165, 2023.

[11] K. L. Moore, A. F. Dalley and A. M. Agur, "Pelvis and Perineum," in *Clinically Orinented Anatomy*, Philadelphia, Wolters Kluwer, 2018, pp. 553-665.

[12] A. Kiapour, A. Joukar, H. Elgafy, D. U. Erbulut, A. K. Agarwal and V. K. Goel, "Biomechanics of the Sacroiliac Joint: Anatomy, Function, Biomechanics, Sexual Dimorphism, and Causes of Pain," *International Journal of Spine Surgery,* vol. 14, pp. S3-S13, 2020.

[13] R. L. Drake, A. Wayne Vogl, A. W. Mitchel, R. M. Tibbitts and P. E. Richardson, "Pelvis and Perineum," in *Grey's Atlas of Anatomy*, Philadelphia, Elsevier, 2015, pp. 211-284.

[14] N. K. Mahato, "Implications of structural variations in the human sacrum: why is an anatomical classification crucial?," *Surg. Radiol. Anat.,* vol. 38, p. 947–954, 2016.

[15] J. S. Cheng and J. K. Song, "Anatomy of the sacrum," *Neurosurg. Focus,* vol. 15, no. 2, pp. 1-4, 2003.

[16] M. K. Jesse, C. Kleck, A. Williams, B. Petersen, D. Glueck, K. Lind and V. Patel, "3D Morphometric Analysis of Normal Sacroiliac Joints: A New Classification of Surface ShapeVariation and the Potential Implications in Pain Syndromes," *Pain Physician,* vol. 20, pp. E701-E709, 2017.

[17] M. P. Lorio, D. W. Polly Jr, I. Ninkovic, C. G. Ledonio, K. Hallas and G. Andersson, "Utilization of Minimally Invasive Surgical Approach for Sacroiliac Joint Fusion in Surgeon Population of ISASS and SMISS Membership," *The Open Orthopaedics Journal,* vol. 8, pp. 1-6, 2014.

[18] A. Joukar, A. Kiapour, H. Elgafy, D. U. Erbulut, A. K. Agarwal and K. V. Goel, "Biomechanics of the Sacroiliac Joint: Part II––Surgical Treatments," *International Journal of Spine Surgery,* vol. 00, no. 00, 2020.

[19] N. Kampkuiker, J. Nellensteijn, E. Hekman, G. Tuijthof, S. Lankheet, M. Koenraders and F. Schröder, "Patient-Specific 3D Virtual Surgical Planning Using Simulated Fluoroscopic Images to Improve Sacroiliac Joint Fusion," *Biomechanics,* vol. 3, pp. 511-522, 2023.

[20] C. T. Martin, L. Haase, P. A. Lender and D. W. Polly JR, "Minimally Invasive Sacroiliac Joint Fusion: The Current Evidence," *International Journal of Spine Surgery,* vol. 14, pp. 20-29, 2020.

[21] P. G. Whang, V. Patel, B. Duhon, B. Sturesson, D. Cher, W. C. Reckling, R. Capobianco and D. Polly, "Minimally Invasive SI Joint Fusion Procedures for Chronic SI Joint Pain: Systematic Review and Meta- Analysis of Safety and Efficacy," *International,* vol. 00, no. 0, pp. 1-15, Jorunal of Spine Surgery.

[22] R. Dubé-Cyr, I. Villemure, P.-J. Arnoux, J. Rawlinson and C.-É. Aubin, "Instrumentation of the sacroiliac joint with cylindrical threaded implants: A detailed finite element study of patient characteristics affecting fixation performance," *Journal of Orthopaedic Reearch,* vol. 39, p. 2693–2702, 2021.

[23] R. Dubé-Cyr, C.-È. Aubin, I. Villemure and P.-J. Arnoux, "Biomechanical analysis of the number of implants for the immediate sacroiliac joint fixation," *Spine Deformity,* vol. 9, p. 1267–1273, 2021.

[24] R. D. Cook, D. S. Malkus and M. E. Plesha, Concepts and applications of finite element analysis, John Wiley & Sons, 1989.

[25] T. Meinders and A. van den Boogaard, "An Introduction to the Finite Element Method (reader)," University of Twente, Enschede, 2014.

[26] M. C. Wang, A. Kiapour, E. Massaad, J. H. Shin and N. Yoganandan, "A guide to finite element analysis models of the spine for clinicians," *JNS Spine,* vol. 40, pp. 38-44, 2024.

[27] S. E. Perdahcioglu, "Nonlinear Finite Element Method, Lecture notes," University of Twente, Enschede, 2024.

[28] S. E. Perdahcioglu, "Geometrical Nonlinearity and Contact, Lecture notes," University of Twente, Enschede, 2024.

[29] A. A. Ivanov, N. A. Ebraheim, V. K. Goel, A. Biyani and M. S. Bisesi, "Development, validation and clinical application of finite element human pelvis model," University of Toledo, 2008.

[30] A. A. Ivanov, A. Kiapour, N. A. Ebraheim and V. Goel, "Lumbar Fusion Leads to Increases in Angular Motion and Stress Across Sacroiliac Joint," *SPINE,* vol. 34, no. 5, pp. E162-E169, 2009.

[31] A. Kiapour, A. A. Abdelgawad, V. K. Goel, A. Souccar, T. Terai and N. A. Ebraheim, "Relationship between Limb Length Discrepancy and Load Distribution across the Sacroiliac Joint—A Finite Element Study," *Journal of Orthopedic Research,* vol. 10, pp. 1577-1580, 2012.

[32] D. P. Lindsey, A. Kiapour, S. A. Yerby and V. K. Goel, "Sacroiliac Joint Fusion Minimally Affects Adjacent Lumbar Segment Motion: A Finite Element Study," *International Journal of Spine Surgery,* vol. 9, no. 64, 2015.

[33] A. Joukar, V. K. Goel, A. K. Agarwal and R. L. Fournier, "Gender Specific Sacroiliac Joint Biomechanics: A Finite Element Study (Master Thesis)," University of Toledo, 2017.

[34] A. Joukar, R. D. Chande, D. P. Lindsey, D. U. Erbulut, R. Dana Carpenter, S. A. Yerby, B. Duhon and V. K. Goel, "Effects on hip stress following sacroiliac joint fixation:," *Spine,* pp. 1-13, 2019.

[35] A. Joukar, A. Kiapour, A. Shah, A. Seyed Vosoughi and V. K. Goel, "Sacroiliac joint stabilization using implants provide better fixation in females compared to males: a finite element analysis," *European Spine Journal,* vol. 30, p. 2351–2359, 2021.

[36] L. Fradet, R.-J. Bianco, R. Tatsumi, J. Coleman and C.-É. Aubin, "Biomechanical comparison of sacral and transarticular sacroiliac screw fixation," *Spine Deformity,* vol. 8, p. 853–862, 2020.

[37] J. A. Miller, A. B. Schultz and G. B. Andersson, "Load-Displacement Behavior of Sacroiliac Joints," *Journal of Orthopaedic Research,* vol. 5, no. 1, pp. 92-101, 1987.

[38] H. J. Rothkötter HJ, and W. Berner, "Failure Load and Displacement of the Human Sacroiliac Joint Under In Vitro Loading," *Arch Orthop Trauma Surg,* vol. 107, no. 5, pp. 283-287, 1988.

[39] P. T. Simonian, M. L. Chip Routt, Jr, R. M. Harrington, K. A. Mayo and A. F. Tencer, "Biomechanical simulation of the anteroposterior compression injury of the pelvis: An

understanding of instability and fixation," *CLinical Orthopaedics and related research,* vol. 309, pp. 245-56, 1994.

[40] M. Dalstra, M. Huiskes and L. Erning, van, "Development and validation of a three-dimensional finite element model of the pelvic bone," *Journal of Biomechanical Engineering,* vol. 117, no. 3, pp. 272-278, 1995.

[41] W. Kraemer, T. Hearn, M. Tile and J. Powell, "The effect of thread length and location on extraction strengths of iliosacral lag screws," *Injury,* vol. 25, no. 1, pp. 5-9, 1994.

[42] K. Yinger, J. Scalise, S. A. Olson, B. K. Bay and C. G. Finkemeier, "Biomechanical Comparison of Posterior Pelvic Ring Fixation," *Journal of Orthopaedic Trauma,* vol. 17, no. 7, pp. 481-487, 2003.

[43] C. van Zwienen, E. van den Bosch, C. Snijders, G. Kleinrensink and A. van Vugt, "Biomechanical comparison of sacroiliac screw techniques for unstable pelvic ring fractures," *Journal of Orthopaedic Trauma,* vol. 18, no. 9, pp. 589-595, 2004.

[44] C. van Zwienen, E. W. van den Bosch, G. Hoek van Dijke, C. Snijders and A. B. van Vugt, "Cyclic loading of sacroiliac screws in Tile C pelvic fractures," *The Journal of Trauma,* vol. 58, no. 5, pp. 1029-1034, 2005.

[45] J. Miller, A. Schultz and G. Andersson, "Load-Displacement Behaviour of Sacroiliac Joints," *Journal of Orthopaedic Research,* vol. 5, no. 1, pp. 92-101, 1987.

[46] P. H. Eichenseer, D. R. Sybert and J. R. Cotton, "A Finite Element Analysis of Sacroiliac Joint Ligaments in Response to Different Loading Conditions," *Spine ,* vol. 36, no. 22, pp. E1446-E1452, 2011.

[47] K.-T. Kim, S.-H. Lee, K.-S. Suk, J.-H. Lee and B.-O. Jeong, "Biomechanical Changes of the Lumbar Segment after Total Disc Replacement: Charite, Prodisc and Maverick Using Finite Elemement Model Study," *The Korean Neurosurgical Society ,* vol. 47, pp. 446-453, 2010.

[48] F. H. Dujardin, X. Roussignol, M. Hossenbaccus and J. M. Thomine, "Experimental study of the sacroiliac joint micromotion in pelvic disruption," *Journal of Orthopaedic Trauma,* vol. 16, no. 2, pp. 99-103, 2002.

[49] M. Wang and G. Dumas, "Mechanical behavior of the female sacroiliac joint and influence of the anterior and posterior sacroiliac ligaments under sagittal loads," *Clinical Biomecahnics,* vol. 13, pp. 293-299, 1998.

[50] A. Goode, E. Hegedus, J. P. Sizer, J.-M. Brismee, A. Linberg and C. Cook, "Three-dimensional movements of the sacroiliac joint: a systematic review of the literature and assessment of clinical utility," *Journal of Manual & Manipulative Therapy,* vol. 16, no. 1, pp. 25-38, 2008.

[51] A. Kapandji AI., "La ceinture pelvienne," in *Physiologie articulaire*, Maloine, 2007.

[52] B. E. Dahl, S. V. Eden and M. D. Rahl, "Surgery for the Painful, Dysfunctional Sacroiliac Joint," in *Anatomy and Biomechanics*, Springer International Publisher, 2015, pp. 15-35.

[53] C. van Zwienen, E. van den Bosch, C. Snijders, G. Kleinrensink and A. van Vugt, "Biomechanical Comparison of Sacroiliac Screw Techniques for Unstable Pelvic Ring Fractures," *Journal of Orthopaedic Trauma,* vol. 18, no. 9, pp. 589-595, 2004.

[54] A. Goode, E. J. Hegedus, P. Sizer, J.-M. Brismee, A. Linberg and C. E. Cook, "Three-Dimensional Movements of the Sacroiliac Joint: A Systematic Review of the Literature and Assessment of Clinical Utility," *Journal of Manual & Manipulative Therapy,* vol. 16, no. 1, pp. 25-38, 2008.

[55] J. Miller, A. Schultz and G. Andersson, "Load-displacement behavior of sacroiliac joints," *Journal of Orthopaedic Research,* vol. 5, no. 1, pp. 92-101, 1987.

[56] "The iFuse Implant System," SI-BONE, [Online]. Available: https://si-bone.co.uk/providers/solutions/ifuse/ifuse-implant-system. [Accessed 29 08 2024].

[57] D. Cher, K. Wroe, W. C. Reckling and Y. Scott, "Postmarket surveillance of 3D-printed implants for sacroiliac joint fusion," *Medical Devices: Evidence and Research,* pp. 337-343, 2018.

[58] M. Haller, "Aetna Covers SI-Bone's iFuse Implant System," Market Scope, 06 05 2020. [Online]. Available: https://www.market-scope.com/pages/news/4540/aetna-covers-si-bone-s-ifuse-implant-system. [Accessed 29 08 2024].

[59] X. Gao, M. Fraulob and G. Haïat, "Biomechanical behaviours of the bone-implant interface: a review," *The Royal Society ,* 2019.

[60] Abaqus, "3Abaqus Version 6.6 Documentation - 0.1.5 Frictional behavior," Abaqus, [Online]. Available: https://classes.engineering.wustl.edu/2009/spring/mase5513/abaqus/docs/v6.6/books/usb/default.htm?startat=pt09ch30s01aus142.html. [Accessed 13 08 2024].

[61] "Sawbones," [Online]. Available: https://www.sawbones.com/media/assets/product/documents/Cellular_Rigid_Polyurethane_Foam_Properties_V03.pdf. [Accessed 2024].

[62] "SI-BONE," [Online]. Available: https://assets.si-bone.com/doc/500131-en-Rev-N-English-iFuse-OUS-IFU_AU-NZ-CI.pdf?mtime=20210216093819&focal=none. [Accessed 2024].

[63] "MatWeb," [Online]. Available: https://www.matweb.com/search/datasheet_print.aspx?matguid=c4297fb8f1094da189732c224e3be1ed. [Accessed 2024].

[64] L. Gibson, M. Ashby, G. Schajer and C. Robertson, in *The Mechanics of Two-Dimensional Cellular Materials*, London, Proceedings of the Royal Society, 1982, p. 25–42.

[65] J. Gibson and M. Ashby, in *The Mechanics of Three-Dimensional Cellular Materials*, London, Proceedings of the Royal Society, 1982, p. 43–59.

[66] S. Maiti, L. Gibson and M. Ashby, "Deformation and Energy Absorption Diagrams for Cellular Solids," *Acta Metallurgica,* vol. 32, no. 11, p. 1963–1975, 1984.

[67] Abaqus, "Abaqus Version 6.6 Documentation," [Online]. Available: https://classes.engineering.wustl.edu/2009/spring/mase5513/abaqus/docs/v6.6/books/stm/default.htm?startat=ch04s04ath118.html. [Accessed 2024 09 07].

[68] T. Meinders and A. van den Boogaard, "Chapter 9.3 Element Type," in *Reader: An Introduction to the Finite Element Method*, Enschede, University of Twente, 2014, pp. 171-173.

[69] M. C. Fischer, F. Krooß, J. Habor and K. Rademacher, "A robust method for automatic," *Natureresearch, Scientific reports,* pp. 1-10, 2019.

[70] F. Eggermont, N. Verdonschot, Y. van der Linden and E. Tanck, "Calibration with or without phantom for fracture risk prediction in cancer patients with femoral bone metastases using CT-based finite element models," *PLOS ONE,* vol. 14, no. 7, pp. 1-13, 2019.

[71] J. H. Keyak, T. S. Kaneko, J. Tehranzadeh and H. B. Skinner, "Predicting Proximal Femoral Strength Using Structural Engineering Models," *Clinical Orthopaedics and Related Research,* vol. 437, pp. 219-228, 2005.

[72] T. Meinders and A. van den Boogaard, "Chapter 9.2 Element shape," in *Reader: An introduction to Finite Element Method*, Enschede, University of Twente, 2014, pp. 165-170.

[73] B. E. Dall, S. V. Eden and M. D. Rahl, "Anatomy and Biomechanics," in *Surgery for the Painful, Dysfunctional Sacroiliac Joint*, Springer International Publishing, 2015, pp. 15-35.

[74] O. Bakland and J. H. Hansen, "The "axial sacroiliac joint"," *Anatomia Clinica,* vol. 6, pp. 29-36, 1984.

APPENDIX A MODEL PROPERTIES FINITE ELEMENT MODELS FOUND IN LITERATURE

In this chapter, the properties are given of the FE models found in literature that model the pelvis with SIJF implants. Note that the changes made on the model of Bruna-Rosso et al. [8] in the follow-up study from Dubé Cyr et al. [22] are not taken into account due to time constrains and the limited important differences for this research (see the captions of the tables and figures for differences that might be of interest in follow-up research).

A.1 TABEL OF THE MODEL SETUP AND SIMPLICIFATIONS

Table A- 1: Overview of the mesh from the models of Ivanov et al. [22], Zhang et al. [10] and Bruna-Rosso et al. [11]. Note that the properties for the modelling of implants for the model of Ivanov et al are extracted from the follow up papers from Lindsey et al. [32] [6]. It is recommended to look into the study of Dubé Cyr et al. for an updated version on the material properties of the model of Bruna-Rosso et al. [22]

	Imaging	**Configuration/ mesh generation**	**Simulation program**
Pelvis model of Ivanov et al. [29]	CT scan (slice thickness 2mm, normal male)	• Configuration generated using image J • Mesh generated using Abaqus 6.7 (symmetrical across the mid-sagittal plan)	Abaqus 6.7
Pelvis model of Zhang et al. [3]	CT scan (slice thickness 1mm, normal female)	• Configuration generated using mimics • Mesh generated using Hypermesh 11.0	Not stated
Pelvis model of Bruna-Rosso et al. [8]	CT scan (slice thickness 0.6mm, slice spacing 1.2mm, pixel size 0.8mm, normal male)	• Configuration generated using a Marching cube type algorithm. • Mesh generation program not stated (sacrum and ilium geometries modified by subtraction implant configuration)	RADIOSS v11

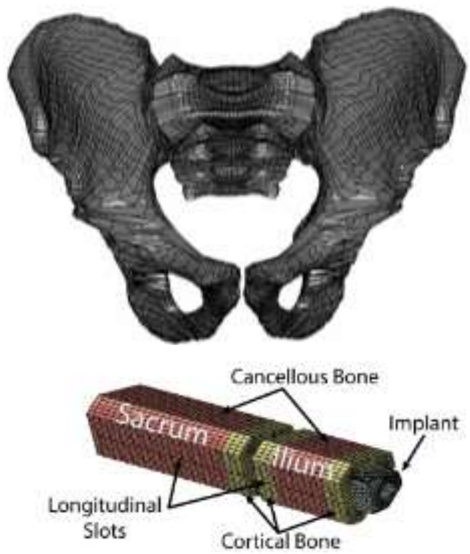

Figure A- 1 (associated with Table A- *2*): Mesh of the pelvis without ligamental bundles in the research of Ivanov et al. [8] (top image). Mesh of the bone implant surface in the research of Lindsey et al. [32] (bottom image).

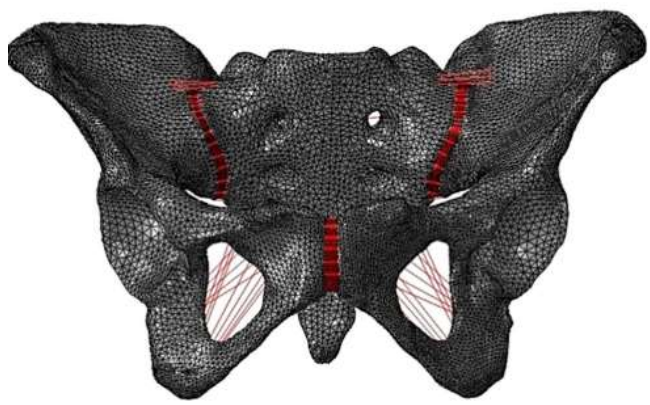

Figure A- 2 (associated with Table A- *2*): Mesh of the pelvis in the research of Zhang et al. [3]

Table A- 2: Overview of the mesh from the models of Ivanov et al. [22], Zhang et al. [10] and Bruna-Rosso et al. [11]. Note that the properties for the modelling of implants for the model of Ivanov et al are extracted from the follow up papers from Lindsey et al. [32] [6]. It is recommended to look into the study of Dubé Cyr et al. for an updated version on the mesh properties of the model of Bruna-Rosso et al. [22], this could be of importance as they state information about results of a mesh refinement study.

	Amount of nodes	**Amount of elements**	**Type of elements**	**Mesh size**
Pelvis model of Ivanov et al. [29]	44595	32586 Ligament bundles: ASL 38, PSL (inner) 23, PSL (outer) 28, IOL 110, STL 15, SSL 15	• Trabecular/ cortical bone: Eight-node solid elements. • Articular surface: Brick elements • Ligaments: Truss elements • Implants: Not stated	Not stated but see Figure A- 1 (Cortical bone modeled as a shell with regional thickness of 1-8mm.)
Pelvis model of Zhang et al. [3]	58948	285170 Ligament bundles: ASL 30, ISL 28, LPSL 8, SPSL 26, SSL 10, STL 16, SP 12, AP 12	• Trabecular/ cortical bone: Not stated • Articular surface: Not stated • Ligaments: 3D tension truss elements • Implants: Not stated	Not stated but see Figure A- 1 (Cortical bone modeled as shell with regional thickness of 0.45 for the sacrum and 1.0 mm for the ilium. Cartilage sacrum 1.8mm and cartilage ilium 0.8mm thick.)

Pelvis model of Bruna-Rosso et al. [8]	+-90000	+-420000, including ligaments	• Trabecular/ cortical bone: four node tetrahedral elements
			• Articular surface: meshed using the elements of the sacrum and iliac bones. (left and right SI joint considered to be symmetric)
			• Ligaments
			    • Sacroiliac posterior and anterior ligaments: 2D 3 node triangular shell elements
			    • Other ligaments and the pubic symphysis: 3D 4 node tetrahedrons
			• Implants: 4 node tetrahedrons
				• Trabecular/ cortical bone: average characteristic length of 3mm for the ilium and 2mm for the sacrum. Average characteristic length of 0.4mm around the SIJ, implants and significant topology changes.
				• Articular surface: meshed using the elements of the sacrum and iliac bones.
				• Ligaments: characteristic length of 2 mm
				• Implants: 0.4 mm characteristic length.
				
				(Cortical bone modeled as shell with regional thickness of 1 for the sacrum and ranging from 0.05 to 5 mm for the ilium.)

A.2 TABLES OF LIGAMENTOUS, CARTILAGE AND PUBIC MATERIAL PROPERTIES

Table A- 3: Overview of the ligaments and their material properties used in the models from Ivanov et al. [22], Zhang et al. [10] and Bruna-Rosso et al. [11]. It is recommended to look into the study of Dubé Cyr et al. for an updated version on the material properties of the model of Bruna-Rosso et al. [22]. Young's modulus E in MPa, Spring coefficient K in N/mm.
*Depending on elongation
**The ligaments and pubic symphysis followed a viscoelastic generalized Kelvin-Voigt material model.

	IOL Interaosseous ligament	**ASL Anterior sacroiliac**	**SSL Sacro-spinous**	**STL Sacro-tuberous**	**PSL (inner/short) Posterior sacroiliac**	**PSL (outer/long) Posterior sacroiliac**	**Interspinous ligament**	**Superior pubic**	**Arcuate pubic**
Pelvis model of Ivanov et al. [29]	E=range from 40 to 102*, v=0.3	E=range from 125 to 316*, v=0.3	E=range from 304 to 771*, v=0.3	E=range from 326 to 826*, v=0.3	E=range from 43 to 110*, v=0.3	E=range from 150 to 381*, v=0.3	Not modeled	Not modeled	Not modeled
Pelvis model of Zhang et al. [3]	Not modeled	K=1500	K=8000	K=9000	K=7500	K=10000	K=3000	K=250	K=250
Pelvis model of Bruna-Rosso et al. [8]	E=40, v=0.3 Viscoelastic Kelvin-Voigt model**	E=40, v=0.3 Viscoelastic Kelvin-Voigt model**	E=40, v=0.3 Viscoelastic Kelvin-Voigt model**	E=40, v=0.3 Viscoelastic Kelvin-Voigt model**	E=40, v=0.3 Viscoelastic Kelvin-Voigt model**	E=40, v=0.3 Viscoelastic Kelvin-Voigt model**	Not modeled	Not modeled	Not modeled

Table A- 4: Overview of the cartilage and pubic material properties used in the models from Ivanov et al. [22], Zhang et al. [10] and Bruna-Rosso et al. [11]. It is recommended to look into the study of Dubé Cyr et al. for an updated version on the material properties of the model of Bruna-Rosso et al. [22]. Young's modulus E in MPa.
*'Softened contact parameter' adjusts the force transfer across the joint depending on the size of the gap exponentially. At full closure, the joint assumes the same stiffness as the surrounding bone.
**The ligaments and pubic symphysis followed a viscoelastic generalized Kelvin-Voigt material model.

	SIJ articular cartilage	**Pubic symphysis/ Interpubic disc**
Pelvis model of Ivanov et al. [29]	Modeled with 'softned contact' parameter from abaqus*	Not modeled
Pelvis model of Zhang et al. [3]	Not stated	E=5, v=0.45
Pelvis model of Bruna-Rosso et al. [8]	E=150, v=0.2	E=397 v=0.3 Viscoelastic Kelvin-Voigt model**

APPENDIX B IILIAC CORTICAL DENSITIES

The assumption was made that the iliac cortical densities is comparable for different patients. In Figure B- 1, one can see the lateral view of different pelvises placed on top of each other, with for each the plane going through the cortical densities visualized in blue. In Table B- 1, one can see the measured angle between the iliac cortical densities plane and the anterior posterior plane.

Although there are some differences, it can be seen that the iliac cortical densities are somewhat comparable for different patients. For now, it is chosen that this comparability is enough to keep this assumption for this research, as we are interested in a general implant configuration for an average pelvis.

Table B- 1: Measured angles between iliac cortical densities plane and anterior posterior plane

Patient	Angle
1	31.02
2	19.19
3	28.96
4	19.75
5	24.28
6	23.9
7	27.1
8	18.7
9	15.03
10	24.07
Mean	23.2
STD	4.76

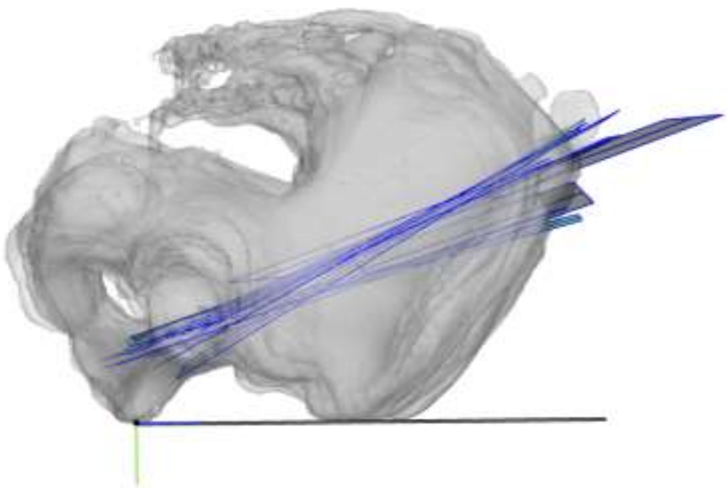

Figure B- 1: Lateral view of different pelvises placed on top of each other, with for each pelvis the cortical densities visualized in blue

APPENDIX C FOAMBLOCK MODEL FOR IMPLANT ANGLE MEASUREMENTS: DEEPER PLACED IMPLANTS

In this appendix section the influence of implant depth is investigated in the foam block. The same model buildup, loading conditions, and boundary conditions of Section 6 are used. Due to time constrains, only implant configuration 2b was tested, along with the same configuration but with implants placed 2.5 mm deeper. A deeper implant configuration was not possible to test due to time constrains, as the 2b implant configuration could only be adapted this much while ensuring that implants still protruded from the ilium block. The implant spacing within the SI joint was kept constant, so the implants were positioned deeper along their longitudinal axis within the configuration. It is expected that deeper placed implants provide better stability [6] (although Lindsey et al. only place one implant deeper).

In Figure C- 1 a vector plot of the displacements of the sacrum block minus the displacements of the ilium block at several positions on the sacrum block can be seen for the different implant configurations. In the figure, minimal difference in displacement direction and magnitude can be observed. In Figure C- 2, the minimal, median and maximal displacement in 3D of the seven nodes displayed in Figure C- 1 are plotted in a bar graph for the different implant configurations. Looking at the precise values of the minimal, median and maximal displacements, the minimal and mean displacements are lower for the deeper placed implant configuration (which is as expected) while the maximal displacement is larger for the deeper placed implant configuration than the original implant configuration (which is not as expected). This could thus indicate a mistake in the model.

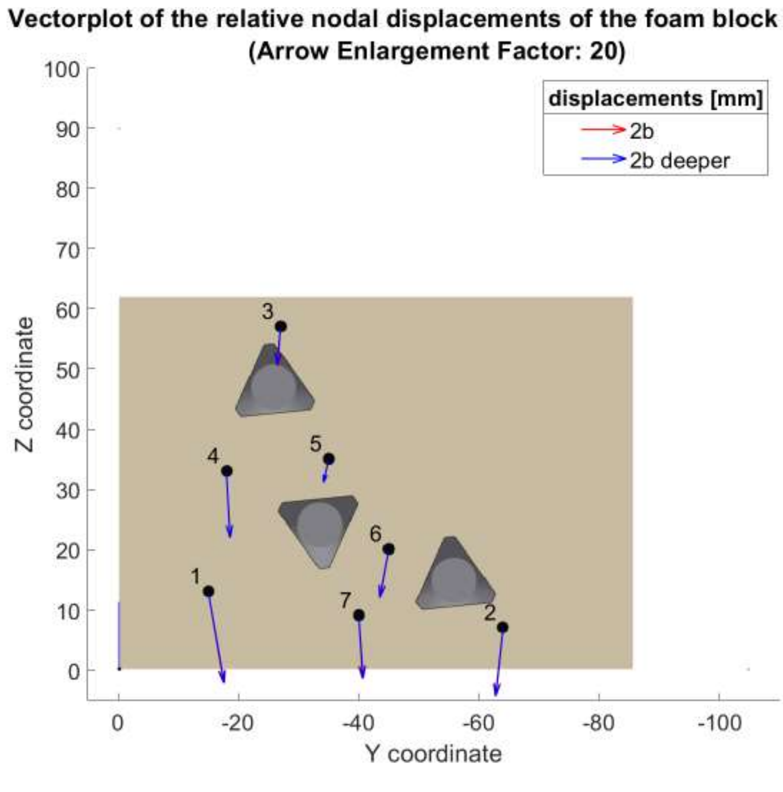

Figure C- 1: Vector plot of the relative nodal displacements of the sacrum block minus the nodal displacements of the ilium block for seven opposite nodes in the YZ plane of the foam block model.

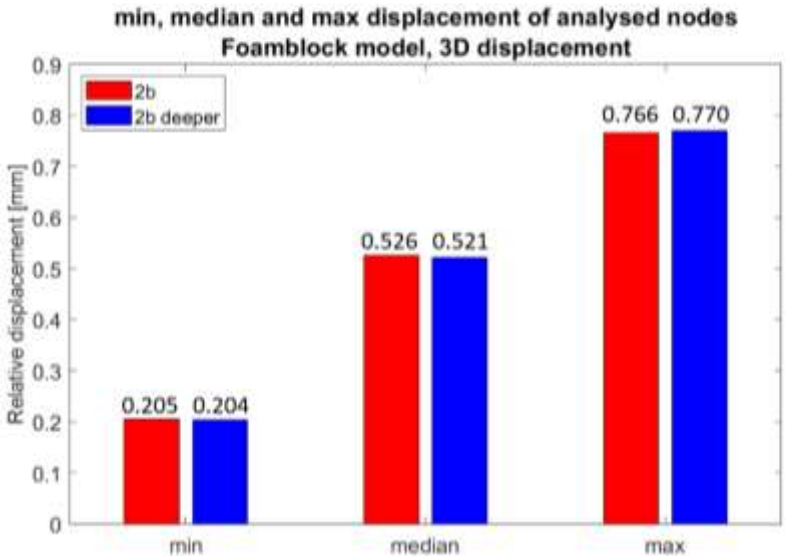

Figure C- 2: Minimum, median and maximal relative displacement in 3D of the analyzed nodes of the foam block model. (The displacements are again defined as the nodal displacements of the sacrum minus the nodal displacements of the ilium for opposite nodes.)

To understand this unexpected behavior, the displacement plots of the model were examined, see Tabel C- 1. From the legends of these displacement plots, it is observed that the deeper placed implants have less minimal and maximal motion, as was expected based on literature [6]. Additionally, the differences are bigger than is observed in Figure C- 2. Furthermore, in Figure C- 3 and Figure C- 4, displacement plots of the whole model are visualized for the 2b and 2b deeper implant configurations. When looking at the overall displacement of the sacrum (which of course could also be accessed only looking at Tabel C- 1) it is again observed that the sacrum with deeper placed implants has less maximal motion.

From the above it can be concluded that the decision of data analysis is of real importance, since the conclusions drawn from Figure C- 2 (deeper placed implants do not necessarily improve implant stability) would be different than the conclusions drawn from Figure C- 3 and Figure C- 4 (deeper placed implants do improve implant stability).

	Sacrum	Ilium
Original implant configuration (2b)	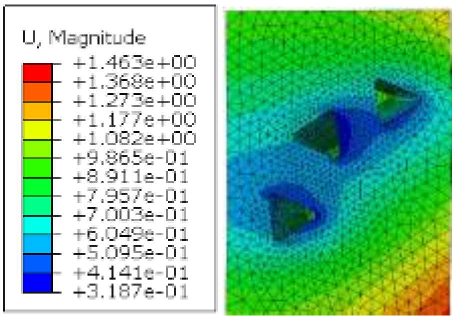	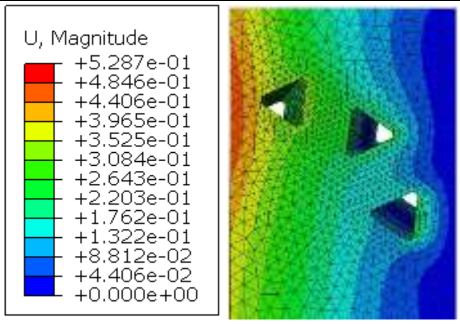
Deeper implant configuration (2b deeper)	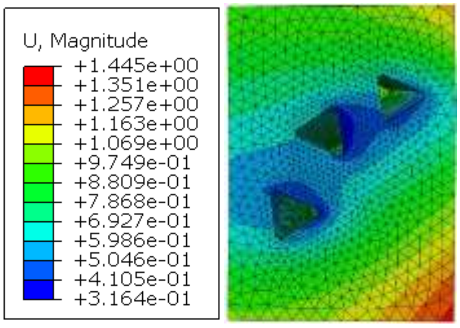	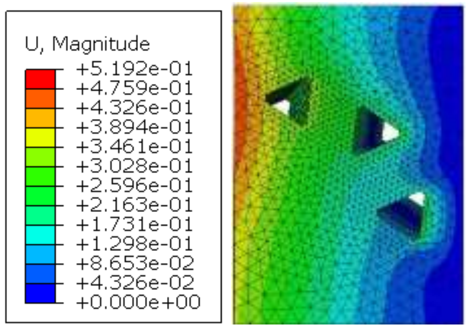

Tabel C- 1: Displacement plots [mm] within the sacrum and ilium block at the SI joint space for the original implant configuration (2b) and the deeper placed implant configuration (2b deeper).

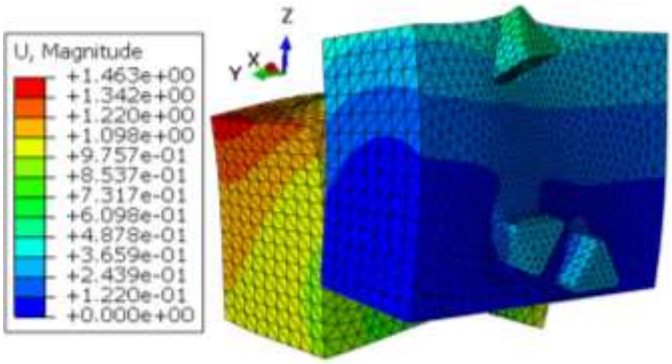

Figure C- 3: Displacement plot [mm] of the whole model for the original implant configuration (2b).

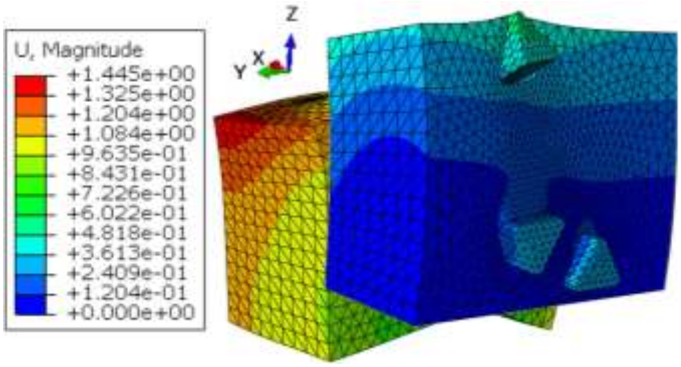

Figure C- 4: Displacement plot [mm] of the whole model for the deeper placed implant configuration (2b deeper).

APPENDIX D PELVIS MODEL FOR IMPLANT ANGLE MEASUREMENTS: TORSION EXPERIMENTS

In this appendix section the influence of the different implant angles on the stability of the SI joint is tested for torsion. The same model buildup and tested implant configurations of Section 6 are used. In Figure D- 1 the loading and boundary conditions for the torsion experiments are shown. Again, a two leg stance boundary condition is used, with a flexion moment of M=20Nm. This flexion moment magnitude is chosen as it falls between the values used in the models from the literature that was analyzed in Section 4.2

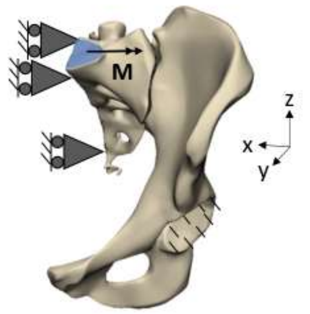

Figure D- 1: Loading and boundary conditions of the pelvis model for torsion testing.

In Figure D- 1 a vector plot of the displacements of the sacrum minus the displacements of the ilium at several positions on the sacrum can be seen for the different implant configurations. As expected, a rotational relative movement is visible. In the figure, minimal difference in displacement direction can be observed, only at the nodes positioned more to the center of the SI joint (nodes 5 and 6) some difference is visible. This indicates that the different implant configurations have a little difference in center of rotation. In Figure D- 3, the minimal, median and maximal displacement in 3D of the seven nodes displayed in Figure 7-18 are plotted in a bar graph for the different implant configurations. No clear trend is observed.

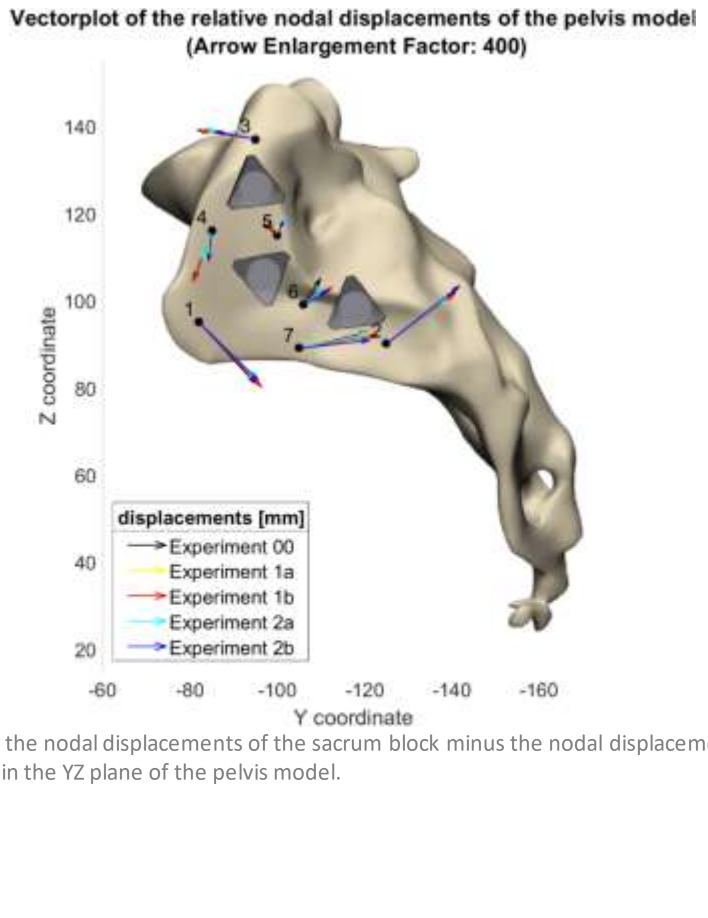

Figure D- 2: Vector plot of the nodal displacements of the sacrum block minus the nodal displacements of the ilium block for seven opposite nodes in the YZ plane of the pelvis model.

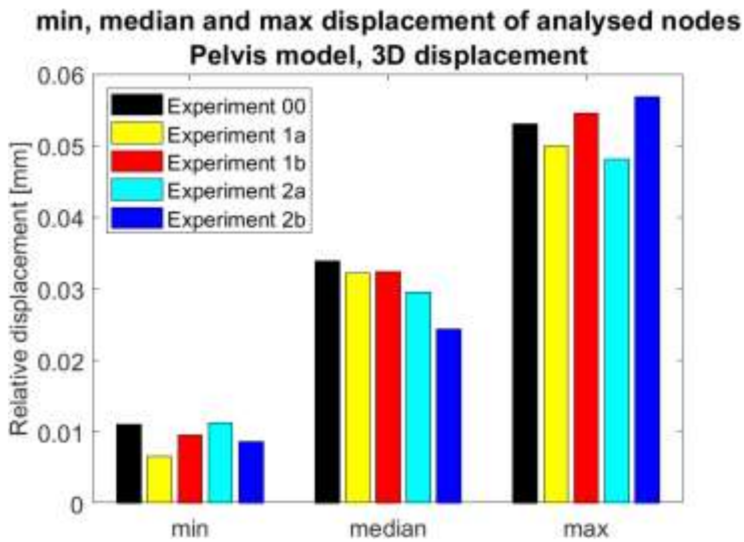

Figure D- 3: Minimum, median and maximal displacement in 3D of the analyzed nodes of the pelvis model. (The displacements are again defined as the nodal displacements of the sacrum minus the nodal displacements of the ilium for opposite nodes.)